Polydispersity in Granular Flows : Exploring Effects in Dry and Submerged Environments

Oscar Polania

THÈSE POUR OBTENIR LE GRADE DE DOCTEUR DE L'UNIVERSITÉ DE MONTPELLIER

En mécanique et génie civil

École doctorale Information Structures Systèmes (I2S)

Unité de recherche Laboratoire de Mécanique et Génie Civil (LMGC)

En partenariat international avec Universidad de los Andes, Colombie

Polydispersity in Granular Flows: Exploring Effects in Dry and Immersed Environments

Présentée par Oscar POLANIA

Le 05 Décembre 2023

Sous la direction de Emilien AZÉMA, Nicolas ESTRADA, Mathieu RENOUF et Miguel CABRERA

Devant le jury composé de

Philippe GONDRET,	Professeur,	Université Paris-Saclay	Président
Laurent LACAZE,	Chargé de Recherche CNRS,	Institut de Mécanique des Fluides de Toulouse	Rapporteur
Marina PIRULLI,	Professeur,	Politecnico di Torino	Rapportrice
Bernardo CAICEDO,	Professeur,	Universidad de los Andes	Examinateur
Emilien AZÉMA,	Professeur,	Université de Montpellier - IUF	Co-direction de thèse
Nicolas ESTRADA,	Professeur Associé,	Universidad de los Andes	Co-direction de thèse
Mathieu RENOUF,	Chargé de Recherche CNRS,	Université de Montpellier	Co-encadrant de thèse
Miguel CABRERA,	Professeur Assistant,	Technische Universität Delft	Co-encadrant de thèse

UNIVERSITÉ DE MONTPELLIER

Universidad de los Andes

Contents

Acknowledgements

I would like to thank Bernardo CAICEDO, Philippe GONDRET, Laurent LACAZE, and Marina PIRULLI for agreeing to be a part of my thesis jury.

I am grateful for the assistance provided by Frédéric DUBOIS and Remy MOZUL at LGMC, as well as the developer team of MigFlow at Université Catholique de Louvain for their support in the simulations conducted for this thesis.

I would like to thank the support and help of Julieth MONRROY, Jose NARANJO, Mauricio TOBAR, and all the technical team at the hydraulic and geotechnical lab at Universidad de los Andes for their valuable support and assistance.

Last, but definitively not least, I would like to my advisory team for their support throughout this PhD journey. I am thankful to Emilien AZÉMA for his inspiring wise and calm facing scientific and life challenges. I thank Mathieu RENOUF for always having time in his schedule for discussing about research and daily activities. I am grateful to Nicolás ESTRADA for *adopting* me halfway through the thesis and for his pragmatic advises to organise my work. Finally, I thank Miguel CABRERA for all that he has taught me over the past five years.

Abstract

Granular flows are complex and evolving systems where grains interact with each other and, if immersed, interact with an ambient fluid. These flows occur at different velocities and state variables, and could behave like solids, liquids or even gases. Granular flows are involved in many circumstances and scales, from geophysical mass flows such as landslides, debris flows, pyroclastic flows, and snow avalanches, to industrial processes like pharmaceuticals, food production, and construction. For simplicity, granular flows are commonly studied with a monodisperse distribution of grains (e.i., grains with nearly the same size); however, among these flows, the grains involved in these processes have different sizes, a property termed as polydispersity.

This thesis focuses on the study of granular flows and, specifically, on the influence that polydispersity has on granular flows. We explore the effect that polydispersity has on steady flows with low inertia, where granular materials can be considered as solids, and high inertia, where granular materials can be considered as fluids. Additionally, we study dry and immersed granular flows in the granular column collapse configuration, that is a benchmark geometry for studying granular flows with phases of acceleration and deceleration.

We study granular flows by means of experimental and numerical methods. The numerical simulations of granular flows are done with discrete element methods (DEM) and, for immersed cases, we use a coupled finite element method (FEM) with DEM. We also conduct a controlled experimental campaign in the triaxial test apparatus where we systematically vary the polydispersity level, aiming to study the strength of polydisperse granular materials in quasi-static conditions. Furthermore, we do the physical modelling of immersed and dry gravity-driven flows in the granular column collapse configuration. Our goal is to explore the influence of polydispersity on granular flows and to identify the influence of the basal fluid pressure on the mobility of granular flows. For the experiments, we use spherical beads, exclusively focusing on the effect that size polydispersity has on granular flows.

Our results allow us to conclude that the shear strength of granular materials is independent of the size polydispersity from a quasistatic condition to a condition of high inertia. For very large inertial conditions, the shear strength of polydisperse materials is smaller compared to that of monodisperse materials. We found that this difference arises from distinct variations in geometric and force parameters belonging to the contact and force network. Additionally, we provide evidence that immersed granular flows are strongly influenced by an increase in polydispersity levels. We show that the difference between monodisperse and polydisperse materials essentially arises from different evolutions of the basal fluid pressure. The initiation of polydisperse flows is delayed compared to monodisperse flows, due to a sustained negative fluid pressure change with large amplitude. Then, as the flow deposits, polydisperse systems reach

longer runout distances due to the generation of exceeding pore pressure that lasts longer than the exceeding pore pressure provoked by monodisperse systems. Finally, we propose a model that links flow kinetic energy with the mobility of granular flows, which applies to different polydispersity levels, and has been successfully validated through simulations and experiments. The results of this thesis provide new insights into the role of polydispersity in both dry and immersed granular flows.

Résumé en français

Polydispersité dans les écoulements granulaires : exploration des effets dans des environnements secs et submergés

Les matériaux granulaires sont des matériaux divisés composés de grains. On parle de matériaux granulaires lorsque les grains sont suffisamment gros, d'un diamètre supérieur à 0.1 mm, pour supposer qu'ils interagissent principalement par frottement et collision. L'écoulement des matériaux granulaires est un processus qui présente un intérêt dans plusieurs domaines. Les écoulements granulaires sont des systèmes complexes et évolutifs dans lesquels les grains interagissent entre eux et, s'ils sont immergés, avec un fluide ambiant. Ces écoulements se produisent à différentes vitesses et contraintes, et peuvent se comporter comme des solides, des liquides ou même des gaz.
Les écoulements granulaires sont impliqués dans de nombreux phénomènes et à de nombreuses échelles, depuis les écoulements de masse géophysiques tels que les glissements de terrain, les coulées de débris, les écoulements pyroclastiques et les avalanches de neige, jusqu'aux processus industriels tels que les produits pharmaceutiques, la production alimentaire et la construction. Par souci de simplicité, les écoulements granulaires sont généralement étudiés avec une distribution monodisperse de grains (c'est-à-dire des grains ayant pratiquement la même taille). Cependant, parmi ces écoulements, les grains impliqués dans ces processus ont des caractéristiques physiques différentes, telles que la forme, la rugosité, la densité ou la taille. Cette dernière, la propriété d'avoir des tailles variées, est appelée polydispersité de taille.
L'étude des écoulements granulaires polydisperses reste une tâche ardue en raison de la difficulté de gérer à la fois des grains de tailles différentes et de prendre en compte des interactions entre les solides et fluides dans de tels systèmes. Notre objectif est de surmonter ces difficultés et de répondre aux questions qui restent en suspens concernant l'influence de la polydispersité sur les écoulements granulaires. Voici quelques-unes de ces questions

- La polydispersité affecte-t-elle la résistance au cisaillement des matériaux granulaires lors de grandes déformations ?

- Comment les microstructures sont modifiées par la polydispersité dans le cas d'écoulements rapides (c'est-à-dire, à grand nombre inertiels)?

- Comment des grains de différentes tailles interagissent-ils dans les écoulements granulaires inertiels ?

- Comment la polydispersité affecte-t-elle les comportements transitoires des écoulements secs et immergés? Et s'il y a un effet, en quoi diffère-t-il de l'influence de la polydispersité sur les écoulements granulaires secs ?
- La polydispersité joue-t-elle un rôle entre la pression du fluide interstitiel et la mobilité de l'écoulement ?
- Le comportement des matériaux granulaires polydisperses est-il mieux décrit par un diamètre caractéristique des grains ou par une fraction de solide ?

Dans cette thèse, nous abordons ces questions ouvertes en réalisant des simulations d'écoulements granulaires polydisperses sec à l'aide d'une méthode par éléments discrets (DEM) et des simulations d' écoulements granulaires immergés grâce à un couplage entre la méthode des éléments finis (FEM) et la méthode DEM utilisée dans le cas sec. Les simulations DEM permettent de modéliser les systèmes à l'échelle du grain, fournissant des informations sur les forces, les positions et les vitesses de chaque grain. Le cadre FEM-DEM que nous utilisons permet de traiter des concentrations élevées de grains en raison de l'augmentation du niveau de polydispersité. En parallèle, nous menons également une campagne expérimentale contrôlée au cours de laquelle nous faisons varier systématiquement la distribution de la taille des grains (GSD), afin d'étudier la résistance des matériaux granulaires polydisperses. En outre, nous procédons à la modélisation physique des écoulements gravitaires immergés et secs dans la configuration d'effondrement d'une colonne granulaire. Nous nous concentrerons sur l'étude de l'influence de la polydispersité sur les écoulements granulaires. Une nouveauté de notre dispositif expérimental est la capacité d'enregistrer la pression basale du fluide le long de la direction principale de l'écoulement, dans le but d'identifier l'influence couplée du mouvement de l'écoulement et de la pression du fluide sur les écoulements granulaires polydisperses.

Chapitre 3

Lorsque les matériaux granulaires sont cisaillés, ils présentent un petit domaine élastique prédominant. Ensuite, le matériau cède, avec ou sans pic de résistance au cisaillement en fonction de la densité initiale. Enfin, le matériau atteint un état stationnaire, dans lequel il se déforme à une contrainte de cisaillement constante, qui peut être liée à l'angle de frottement résiduel. Cependant, le rôle de la polydispersité sur la résistance au cisaillement des matériaux granulaires fait encore l'objet de débats. En particulier, une série d'études a prouvé, à l'aide de simulations numériques, que la résistance au cisaillement est indépendante de la polydispersité. Cette observation contre-intuitive reste insaisissable pour les expérimentateurs, et en particulier pour certaines communautés (géotechnique et génie civil notamment) qui l'utilisent comme paramètre de conception.

L'objectif de ce travail est de mener une série d'expériences systématiques et contrôlées afin de confirmer si la résistance au cisaillement est indépendante de la polydispersité, décrite en termes de taille de grains, et de le rapport entre le plus grand et plus petit grain, et distribution de la taille des grains. Pour ce faire, nous avons construit des échantillons de billes en céramique et les avons cisaillés dans un dispositif triaxial. Nous avons fait varier la polydispersité, en

construisant des échantillons granulaires monodisperses, bidisperse et polydisperse, ce qui nous a permis d'étudier les effets de la taille des grains, de leur distribution sur l'angle de frottement résiduel.
Nos résultats confirment que la résistance résiduelle au cisaillement des matériaux granulaires est effectivement indépendante du niveau de polydispersité. Les résultats expérimentaux présentés dans ce travail sont importants car ils comblent le fossé entre les expériences et les simulations des systèmes polydisperses quasi-statiques, en confirmant que la résistance au cisaillement des matériaux granulaires est indépendante de la distribution de la taille des grains. Ils servent également de lien, en connectant les résultats provenant des communautés de la physique des milieux granulaires et de la mécanique des sols, et en orientant la discussion sur la résistance résiduelle vers une conclusion commune. Les résultats de ce travail contribuent à la connaissance du comportement des matériaux granulaires polydisperses qui est une question d'intérêt dans les processus naturels et industriels.

Chapitre 4
L'écoulement des matériaux granulaires subit divers comportements qui dépendent du taux de déformation et de l'état de contrainte du système. Les matériaux granulaires sont généralement étudiés dans le régime quasi statique, où les grains interagissent par des contacts durables. Cependant, les écoulements granulaires peuvent également se produire dans des conditions de forte agitation, où les grains interagissent par collisions et contacts de courte durée. L'objectif principal de cette étude est de mieux comprendre les processus micromécaniques qui régissent les écoulements granulaires polydisperses caractérisés par une forte inertie.
Pour cela, nous utilisons la méthode par éléments discrets NSCD (pour Non Smooth Contact Dynamics) pour simuler la configuration d'une cellule de cisaillement à pression de confinement constante, permettant des changements de volume. Ce choix a été fait parce que les variations volumétriques font partie intégrante de la plupart des processus d'écoulement. Notre objectif est de décrire de manière exhaustive la rhéologie et les microstructures des écoulements granulaires polydisperses en fonction de leurs niveaux d'inertie. De plus, nous cherchons à comprendre les différences micro-mécaniques entre des systèmes ayant une polydispersité différente et ce pour différents niveaux d'inertie, caractérisé par le nombre inertiel I.
Les résultats obtenus nous ont permis d'étudier le comportement macroscopique des matériaux granulaires polydisperses et l'interaction des grains à l'échelle du contact. Nous avons montré que l'indépendance de la résistance au cisaillement par rapport à la polydispersité reste vraie pour les écoulements granulaires dans le régime dense avec un nombre inertiel $I \lesssim 0.1$. Au contraire, pour des valeurs de $I \gtrsim 0.1$, la résistance au cisaillement décroît avec la polydispersité. Aux faibles nombre inertiels, l'indépendance de la résistance trouve ses origines dans une compensation presque parfaite entre la perte de l'anisotropie géométrique et le gain de l'anisotropie induite par les forces normales. Au contraire, grandes valeurs de l'anisotropie géométrique décroît plus vite que l'augmentation de l'anisotropie des forces normales, expliquant de fait la décroissance du frottement macroscopique.

Chapitre 5 & 6

Nous utilisons la configuration de l'effondrement d'une colonne granulaire pour étudier l'influence de la polydispersité sur les écoulements granulaires immergés et secs sous gravité. Nous visons à étendre les observations sur les effondrements de colonnes monodisperses aux colonnes polydisperses en explorant différentes GSD, allant de systèmes initialement lâches à des systèmes initialement denses. Nous nous attachons à clarifier le rôle de la polydispersité sur la dynamique d'effondrement de la colonne, la vitesse et l'étalement final. Pour atteindre cet objectif, nous entreprenons des études numériques et expérimentales sur l'effondrement de colonnes granulaires monodisperses et polydisperses dans différents régimes d'écoulement, allant du régime visqueux-inertiel transitoire, où il existe de fortes interactions fluide-grain, au régime de chute libre, où les interactions fluide-grain sont négligeables.

Nous simulons l'effondrement de colonnes granulaires dans des conditions immergé et sèche. Cette étude est réalisée en couplant l'approche NSCD à une méthode FEM de fluide non résolu (la taille de maille du fluide est plus grande que le plus gros grain). La simulation de systèmes polydisperses est très coûteuse en raison du grand nombre de grains requis pour avoir des échantillons granulaires polydisperses représentatifs, du pas de temps de calcul qui doit être petit pour éviter les interpénétrations entre particules, et du transfert de quantité de mouvement d'un groupe de particules en mouvement à la maille du fluide correspondante. Bien que la solution finale avec ce type d' approche n'est pas la plus précise, elle capte l'essentiel de la physique pour que les défis mentionnés ci-dessus soient gérés avec succès.

Nous étudions la nature tridimensionnelle de l'effondrement de la colonne granulaire dans le cadre d'une campagne expérimentale au cours de laquelle nous faisons varier le niveau de polydispersité de la colonne, son rapport d'aspect et l'environnement fluide. Les expériences portent sur des colonnes composées de billes de verre de différentes tailles et permettent d'étudier des systèmes monodisperses et polydisperses. Nous utilisons des billes de verre pour exclure les effets contradictoires tels que l'allongement des grains, l'angularité ou la rugosité, ce qui nous permet de nous concentrer uniquement sur l'influence de la GSD sur les écoulements granulaires. En outre, nous enregistrons la pression interstitielle basale sous la géométrie initiale de la colonne et le long de la direction principale de l'effondrement. Nous établissons un lien entre l'évolution de la pression interstitielle et la séquence de l'effondrement de la colonne, et nous révélons comment ces deux éléments sont modifiés par l'augmentation du niveau de polydispersité. Notre étude présente des preuves expérimentales sur la façon dont la polydispersité affecte la séquence d'effondrement.

Nous montrons que le niveau de polydispersité a un effet plus important sur les colonnes immergées que sur les colonnes sèches. Pour les colonnes sèches, la séquence d'effondrement reste indépendante du niveau de polydispersité, atteignant des distances similaires à des temps similaires. Cette observation est commune aux colonnes courtes et hautes. La distance d'arrêt, qui est une mesure indirecte de la résistance au cisaillement, ne varie que légèrement en fonction de la polydispersité, ce qui est en accord avec nos résultats triaxiaux montrant que la polydispersité n'affecte pas la résistance au cisaillement.

Dans le cas immergé, nous montrons que les séquences effondrements dépendent fortement du niveau de polydispersité. Nous montrons que l'augmentation de la polydispersité, affecte la dynamique d'effondrement, et plus particulièrement l'initiation de l'effondrement et la distance finale. Les variations de ces deux caractéristiques sont dues à des différences dans l'évolution de la pression interstitielle. Lorsque la colonne commence à s'effondrer, il y a un changement négatif de la pression interstitielle qui provoque une augmentation temporelle de la résistance de la colonne. Nous montrons que l'effondrement des colonnes polydisperses est retardé ce qui se traduit par une pression négative de la pression interstitielle en comparativement au cas des colonnes monodisperses. De plus, la faible perméabilité des colonnes polydisperses, due à une compacité élevée liée à la présence de petits grains, entrave l'entrée du fluide dans la colonne retardant l'effondrement. Ensuite, pendant l'étalement de la colonne, la pression du fluide mesuré à la base de la masse en mouvement, augmente. Nous avons révélé que dans les écoulements monodisperses, l'excès de pression interstitielle est rapidement dissipé, tandis que dans les écoulements polydisperses, l'excès de pression interstitielle reste plus longtemps, diminuant la résistance et produisant une fluidisation localisée qui se traduit par des distances d'écoulement plus longues.

Chapitre 7

Pour finir, nous introduisons un modèle de mobilité qui met en corrélation l'écoulement de la colonne avec l'énergie d'effondrement et qui fonctionne de manière satisfaisante pour différents niveaux de polydispersité et pour les effondrements de colonnes immergées et sèches. Nous proposons que ce modèle simplifié soit utilisé pour prédire la mobilité des colonnes granulaires en fonction de l'énergie d'effondrement de la colonne. Pour présenter ce modèle, nous nous appuyons sur les résultats obtenus à partir des simulations numériques et des expériences réalisées durant ces travaux de thèse, mais en incluant également des résultats d'études antérieures issus de la littérature.

Nous montrons que le modèle reliant énergie et mobilité reste valable pour les résultats expérimentaux et numériques. Ce modèle s'applique aux effondrements de colonnes granulaires où la vitesse d'effondrement est principalement contrôlée par la gravité et n'est pas limitée par la vitesse de Stokes (c'est-à-dire les écoulements dans le régime de chute libre, d'inertie et visqueux-inertiel). Le modèle est une simplification d'un processus physique complexe, mais il est remarquable qu'il mette à l'échelle l'écoulement final avec la cinématique de l'effondrement. Ce modèle simplifié pourrait être utilisé comme outil d'analyse inverse pour analyser et comprendre les mouvements de masse tels que les glissements de terrain ou les coulées de débris. De plus, nous étendons la mise à l'échelle entre l'énergie et la mobilité, et proposons un modèle basé sur l'énergie pour estimer l'écoulement des colonnes granulaires. Ce modèle ne nécessite que des paramètres matériaux, les variables géométriques initiales, la vitesse du front d'effondrement et un coefficient de proportionnalité unique entre l'énergie et l'écoulement.

CHAPTER 1

Introduction

The daily routine is full of moments where people interact with granular materials, or with materials that during their production were initially handled as granular materials. The grains being part of these materials have different sizes; we often refer to granular materials when grains have a diameter $d > 0.1$ mm and mainly interact by friction and collision. For materials with grains of smaller size, there are other controlling interactions like the Van der Waals forces, humidity or thermal agitations [1]. Scratching the sand beach, preparing the morning coffee, or playing the maracas are all examples of common activities when people directly interact with granular materials. Also, commonly known materials are produced with grains. Concrete, for example, is produced by mixing aggregates of different sizes, from $d = 0.75$ mm to 47.5 mm, with cement and water. Another example, and this one less intuitive, is steel. For producing steel, it is necessary to transport, storage, mix, and melt coke and ore grains of different sizes.

A process related to these materials that is of interest in several fields is the flow of granular materials. Granular flows are complex and evolving systems where grains interact with each other and, if immersed, interact with an ambient fluid. These flows occur at different velocities and state variables (e.g., different confinement pressure P_c), and could behave like solids, liquids or even gases [2]. Moreover, granular flows are involved in many circumstances and scales, from geophysical mass flows such as landslides, debris flows, pyroclastic flows, and snow avalanches, to industrial processes like pharmaceuticals, food production, and construction (see Fig. 1.1).

Figure 1.1. Examples of granular flows of different scales. (a) Flow of angular grains in a split-bottom Couette cell, (b) flow of granular materials through a pipe and then dumping to make a scour protection of a submarine foundation, (c) pyroclastic flow entering to the sea. The images (a), (b) and (c) were adapted from Cabrera & Polanía [3], Asgarpour [4] and Luckett *et al.* [5], respectively.

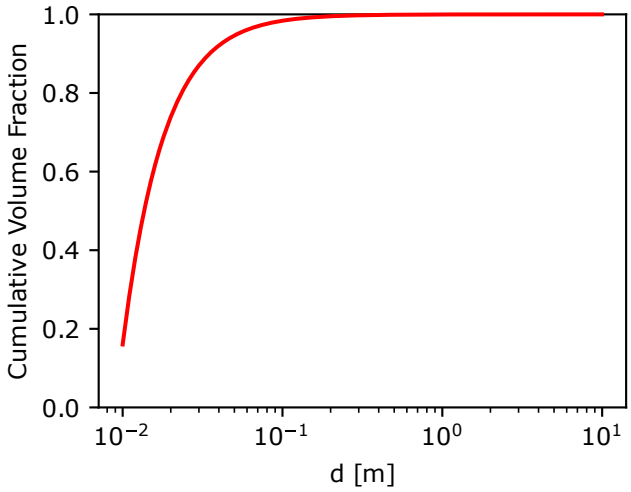

Figure 1.2. Cumulative Volume Fraction CVF as a function of the grain diameter d. The distribution here presented corresponds to the Grain Size Distribution GSD of the Saturn's rings [7]. - Yes, the planet. -

For simplicity, granular flows are commonly studied with a monodisperse distribution of grains (e.i., grains with nearly the same size); however, among these flows, the grains involved in these processes have different physical features such as shape, rugosity, density, or size. The latter, the property of having varied sizes, is termed as *polydispersity*. Debris flows are an example that clearly shows how relevant polydispersity is in granular flows. In a debris flow the gap between the minimum grain $d_{\min}$ and the maximum grain diameter $d_{\max}$ could be orders of magnitude, from micrometers to meters [6]. The grain size distribution GSD is a variable to describe the grain sizes of a material. Normally, the GSD is presented as a distribution of the Cumulative Volume Fraction CVF of a grain with diameter d. Fig. 1.2 presents an interesting example of the GSD identified by the *Voyager Radio Science Subsystem* in the rings of Saturn (the planet) [7]. This is an interesting example because it allows us to open a perspective on the importance that the GSD concept has in another discipline, such as planetary sciences. Polydispersity, besides offering the possibility of finding granular materials with different GSDs, also matters in other important parameters of granular materials such as porosity, permeability, or density [8]. The latter is usually quantified as the solids' volume concentration and is referred to as the packing fraction ϕ.

Polydispersity, as an intrinsic property of granular materials, has been widely explored in static conditions, but it is remarkable that few studies are devoted to their behaviour during transitional or steady flows and even less in its interaction with a fluid. The rheological behaviour of immersed granular materials strongly depends on materials' parameters. For example, the mobility of submersed granular collapses depends on the initial packing fraction [9]. The changes in the packing fraction, whether because it reduces or increases, produce variations of the internal fluid pressure that alter the flow mobility, and these variations are associated with the pores' size. Thus, polydispersity, that increases the packing fraction and reduces the pores's size, is likely to play an important role in the feedback between mobility

and fluid pressure evolution [10], but such description and understanding is still missing. Moreover, in the perspective of large-scale predictive modeling, one of the main challenges consists of identifying an equivalent continuous material. Normally, the material's description relies on a characteristic grain diameter, but in polydisperse materials, it is not clear whether there is a characteristic grain diameter or even if the packing fraction could provide a better representation.

Studying polydisperse granular flows remains a challenging task due to the difficulty of managing grains of different sizes and the complexity of accounting for the interactions between solid and fluid phases in such systems. Our goal is to overcome these challenges willing to answer questions that are still open about the influence that polydispersity has on granular flows. Some of theses questions are:

- Does polydispersity affect the shear strength of granular materials at large deformations?
- What distinguishes the mechanics at the grain scale of monodisperse and polydisperse granular flows when they have a high inertia level?
- How do small, large and small-large grains interact in inertial granular flows?
- How does an increase in polydispersity affect the flow of immersed transitional flows? And if there is an effect, How does it differ from the influence that polydispersity has on dry granular flows?
- Does polydispersity play an influence in the feedback between pore fluid pressure and the flow mobility?
- Does the behaviour of polydisperse granular materials is better described by a characteristic grain diameter d or by a packing fraction ϕ?

In this thesis, we will address these open questions by performing simulations of polydisperse granular flows using the Discrete Element Method (DEM) and by simulating immersed granular flows through a coupled finite element method (FEM) - DEM approach. The DEM simulations enable the modelling of individual grains, providing information about the forces, positions, and velocities of each grain. The FEM-DEM framework we employ is adept at handling high concentrations of solids due to the increased polydispersity level. We also conduct a controlled experimental campaign where we systematically vary the GSD, aiming to study the strength of polydisperse granular materials. Furthermore, we do the physical modelling of immersed and dry gravity-driven flows in the granular column collapse configuration. Our focus is on investigating the influence of polydispersity on granular flows. A novelty of our experimental setup is the capability to record basal fluid pressure along the flow's principal direction, with the aim of identifying the coupled influence of the flow motion and the fluid pressure on polydisperse granular flows.

*Mario Baos 2023, *En fotos: el drama de los damnificados por el derrumbe en Rosas, Cauca*, El Espectador, accessed 28 March 2023, https://www.elespectador.com/colombia/en-fotos-el-drama-de-los-damnificados-por-el-derrumbe-en-rosas-cauca/

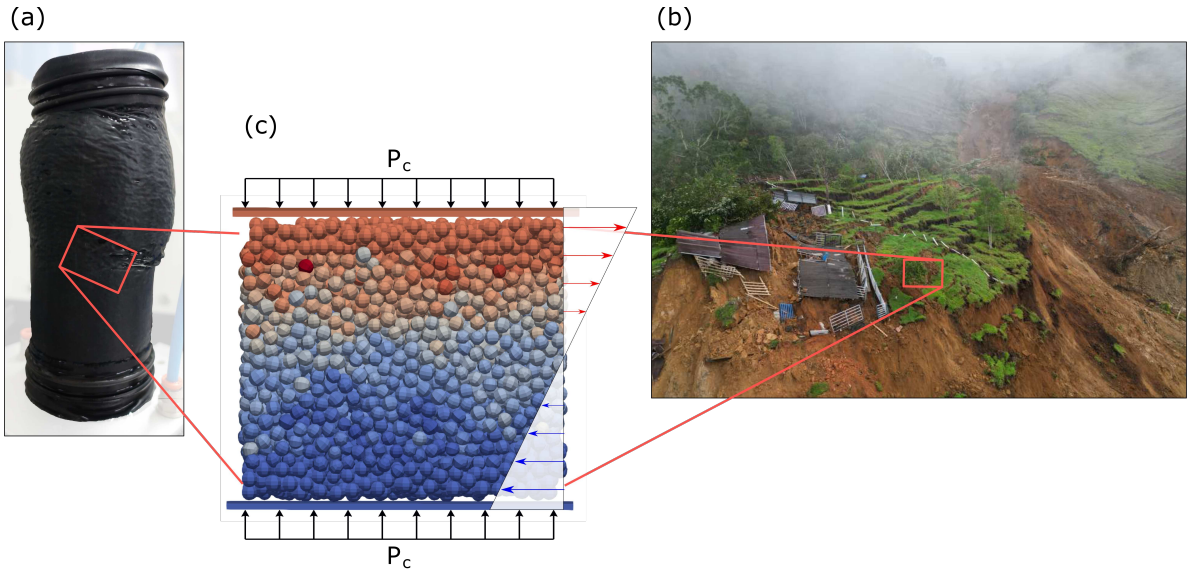

Figure 1.3. Granular flows of different scales. Figure (a) shows a cylindrical sample of ceramic beads after a triaxial test experiment. Figure (b) shows a landslide*. Figure (c) presents the geometry of a shear cell simulation made with Discrete Element Methods DEM, representing the micro-mechanism inside (a) and (b). In the shear simulation (c), the horizontal arrows stand for the shear rate at which the material is being deformed, and the vertical arrows represent the confinement pressure P_c imposed by experimental conditions (a) or by geostatic condition (b). In (c), the grains' colour represent the velocity direction and the colour's intensity stands for the magnitude.

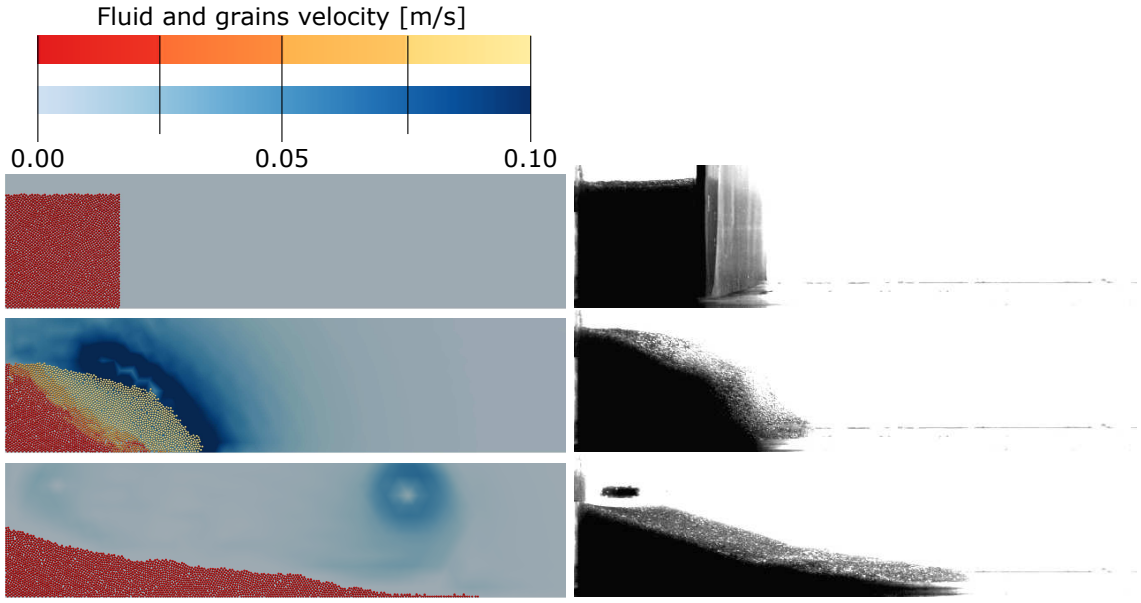

Figure 1.4. Flow of granular materials in the granular column collapse configuration. The left column presents snapshots of a DEM-FEM simulation and the rigth column showcases an experiment. The upper, middle and bottom rows show the granular column before, during and after the collapse, respectively.

This thesis is organised as follows. In Chapter 2, we discuss about previous works that led us to identify the open questions, and present an overview of how we aim to answer them. In Chapter 3 we present an experimental study developed in the triaxial test to assess the strength of granular materials, focusing on the effect that the GSD has on polydisperse samples. In Chapter 4 we present a numerical study that explores the effect that polydispersity has on granular flows with different inertial levels done with DEM. In Chapter 5 we present a numerical study of polydisperse granular flows in the granular column collapse configuration using a DEM-FEM framewok. In Chapter 6 we experimentally explore the effect that polydispersity has on immersed and dry granular flows in the granular column collapse configuration. In Chapter 7 we rely on conclusions of Chapter 5 and 6, and use the results of other authors, to propose a model that links the kinetic energy of a granular flow and the mobility that it reaches. Last, in Chapter 8, we present the thesis general conclusions, the added value of our study and the answer to the open questions introduced here. Moreover, we discuss about possible topics of research in further studies of polydisperse granular flows.

CHAPTER 2

State of the Art

2.1 | Polydisperse Granular Materials

Polydispersity in granular materials refers to the property of having varied grain sizes. In many disciplines, the distribution of the grains' sizes (or Grain Size Distribution GSD) is used to obtain essential information about the variability of this property (see Fig. 1.2). In Soil Mechanics, for example, the GSD holds such significance that 'The Unified Soil Classification System' relies on GSD information to classify soils. For instance, the soil's uniformity coefficient $\mathrm{Cu} = d_{60}/d_{10}$, where d_{10} and d_{60} are the diameters for which the GSD has 10% and 60% of the cumulative mass, respectively, is used for identifying coarse soils as poorly graded $\mathrm{Cu} < 4$ or as well graded $\mathrm{Cu} \geq 4$. This value indicates the variety of grain sizes, and somehow the polydispersity level, and holds significant importance within the community, being studied as a key parameter in the mechanical behaviour of soils [11, 12].

Polydispersity, besides offering the possibility of finding granular materials with different GSDs, also matters in other important parameters of granular materials such as the porosity, hydraulic conductivity [8], or density [13]. Although these three are closely related, the porosity and hydraulic conductivity normally refer to the pores' size* in a granular material, and the density refers to the solids' concentration. The solids' concentration is usually quantified with the ratio of the solids volume V_s and a reference total volume V as the packing fraction

$$\phi = V_\mathrm{s}/V. \tag{2.1}$$

The packing fraction ϕ† has been a subject of interest in many fields because it is a problem of volume optimisation (e.g., storing aliments in silos, compacting medicines or arranging crystallised structures [14] are all examples of the packing fraction importance). For monodisperse granular materials (i.e., materials composed of grains that have nearly the same size), reference ϕ values are the random loose $\phi_\mathrm{rlp} \simeq 0.55$ and random close packing $\phi_\mathrm{rcp} \simeq 0.64$ [15]. For polydisperse granular materials, the packing fraction is greater than in monodisperse systems, because small grains partially fill the voids between larger grains. A result dating

*The size of the pores depends on the size of the grains. The smaller the grains, the smaller the pores. In polydisperse materials, the presence of mixed grains of different sizes results in the reduction of pore size, leading to a decrease of both the porosity and hydraulic conductivity.

†In the soil mechanics community, the soil packing is generally considered with the void ratio e that can be computed as $\mathrm{e} = (1-\phi)/\phi$.

back to the early 20th century by Fuller & Thompson [16] indicates that the packing fraction ϕ of polydisperse materials is optimised by a GSD with a cumulative volume fraction CVF that follows a power law of the form

$$\mathrm{CVF} = \left(\frac{d}{d_{\max}}\right)^{\iota}, \tag{2.2}$$

with the exponent $\iota \simeq 0.5$. More recent numerical studies, by means of DEM simulations, have systematically explored the effect of ι on ϕ, confirming that the densest and better connected arrangement is obtained for $\iota \simeq 0.5$ [13, 17, 18].

As mentioned, polydispersity matters in different aspects of granular materials, and its importance relies on the range of grain sizes and the distribution they follow. In this thesis, we will refer to the exponent ι in Eq. (2.2) as the GSD's form and to the polydispersity level[‡] as the ratio between the largest $d_{\max}$ and smallest grain $d_{\max}$ as

$$\lambda = d_{\max}/d_{\min}. \tag{2.3}$$

This value is intuitive for indicating the polydispersity level and stands for the whole span of grain sizes[§].

2.2 | Shear Strength of Granular Materials

From continuum mechanics, the stress tensor is a multi-dimensional array that describes the stress state at a given point in a materials. Defining a mean stress tensor in granular material has been a matter of debate due to the discrete nature of the media [19, 20]. Nevertheless, the stress tensor provides important information about the response of a granular material to external forces and correlates any stress state into nine components, denoted as:

$$\boldsymbol{\sigma} = \begin{bmatrix} \sigma_{11} & \sigma_{12} & \sigma_{13} \\ \sigma_{21} & \sigma_{22} & \sigma_{23} \\ \sigma_{31} & \sigma_{32} & \sigma_{33} \end{bmatrix}. \tag{2.4}$$

The eigenvalues of the stress tensor $\det(\boldsymbol{\sigma} - \Gamma \mathbf{I} = 0)$, where $\mathbf{I}$ is the identity tensor, represent the principal stresses σ_1, σ_2 and σ_3, being σ_1 and σ_3 the major and minor stresses, respectively. Submitted to isotropic loading conditions, granular materials tend to reduce their volume, which implies an increase of the packing fraction ϕ, until a stable stress state and granular structure are reached. Under isotropic loading, the principal stresses are virtually the same ($\sigma_1 \simeq \sigma_2 \simeq \sigma_3$) and shear deformations do not occur. Granular materials experience large

[‡]The polydispersity level in a granular systems is presented in different forms. Notably, Cu is an indicator of how different the grains' sizes are, but it is limited to the interval determined by d_{10} and d_{60} and does not show the whole span covered by the GSD. Another common form to present the polydispersity level is the *Size Span* $S = (d_{\max} - d_{\min})/(d_{\max} + d_{\min})$ that has a domain $\mathrm{D} = (0, 1)$. Although S indicates the polydispersity level from the smallest to the largest grain, it is a value that quickly grows and it is tricky to have a notion of how large polydispersity is.

[§]It is possible to compute the the Uniformity Coefficient from λ as $\mathrm{Cu} = \frac{1+0.6^{1/\iota}(\lambda-1)}{1+0.1^{1/\iota}(\lambda-1)}$ with ι being the exponent (or shape) of the Cumulative Volume Fraction (see Eq. 2.2) [18].

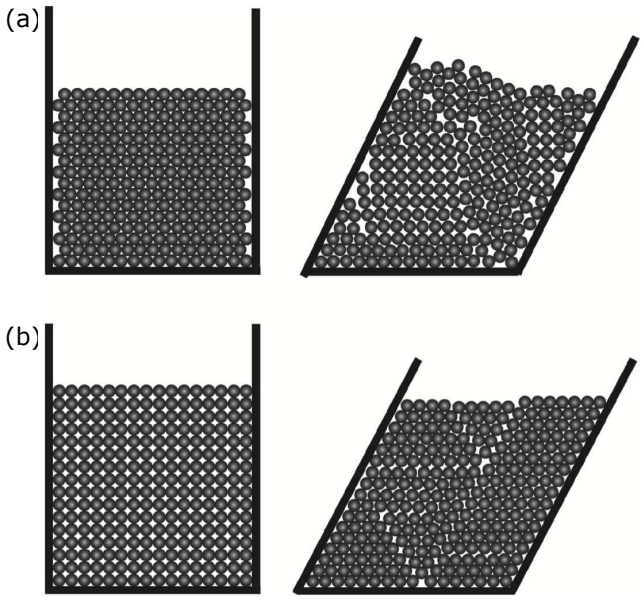

Figure 2.1. Sketch of the shearing of initially (a) dense and (b) loose granular materials. This figure was adapted from Andreotti *et al.* [1].

shear deformation, like in a granular flow, when there is an anisotropic loading condition $\sigma_1 \neq \sigma_3$.

When granular materials are sheared, they exhibit a small deformation range in which the material behaviour could be consider as elastic and deformations are reversible. As both volumetric and distortional deformations increase, the shear strength increases too, up to a limit that is highly dependent on the initial density of the arrangement. Comparing extreme case scenarios, initially dense granular materials exhibit a greater strength than initially loose because they need to overpass a limit imposed by the material dilatancy. On the contrary, initially loose granular materials contract when they are sheared due to an accommodation of grains into the material's voids. Fig. 2.1 presents a sketch of granular materials submitted to shear, showing that dilatancy and contractions are both volume changes that represent an increase and a decrease of the material's voids, respectively. Beyond the elastic regime, plasticity develops and irreversible deformations start to accumulate. Afterwards, a stationary state is reached, in which shear deformations continue to accumulate while volume and shear strength fluctuate around approximately constant values for both dense and loose materials.

The strength of granular materials is their capacity to support deviatoric stresses q. The deviatoric stress q represents the part of the stress state that is responsible for shear deformation and it is defined as the difference between the principal stresses

$$q = \frac{\sigma_1 - \sigma_3}{2}. \tag{2.5}$$

Submitted to shear deformations, initially dense granular materials need to dilate, having a peak deviatoric stress before reaching the stationary state at large strains. In this state, that is common for both initially dense and loose samples, the granular structure has a configuration

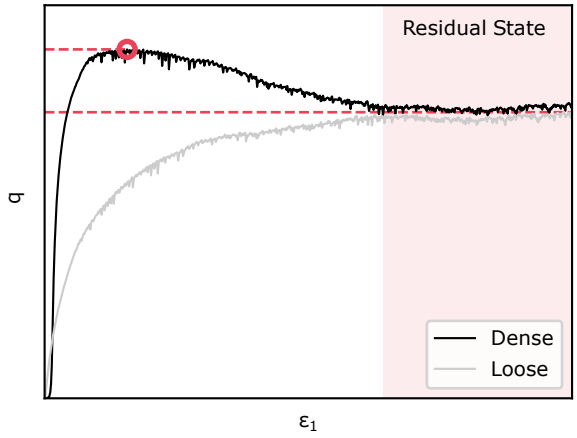

Figure 2.2. Typical curve of the deviatoric effective stress q vs vertical strain ϵ_1 of dense and loose granular materials. The shaded area is considered as the region of large deformation where the material has reached the residual strenght. The marker stands for the peak strength, and the dashed lines compare the the peak and residual strength.

that allows deformations at constant stresses. Fig. 2.2 presents a typical strength q vs vertical strain ϵ_1 curve for loose and dense samples.

In saturated conditions, when the material's voids are filled with fluid, the strength of a granular material is controlled by the effective normal stress σ' sustained by the grains. The effective stress is the stress controlling volume changes [21] and is the difference between the total stress acting on the granular system and the pore fluid pressure P

$$\boldsymbol{\sigma'} = \boldsymbol{\sigma} - P\boldsymbol{I}. \tag{2.6}$$

The dilatancy or a contracting tendency in granular materials have a strong influence on the material shear strength because they produce a variation of the pore fluid pressure P. Dilatancy generates suction, producing an inflow of fluid and reducing globally the pore pressure. On the contrary, contraction generates an excess of pore pressure because water is expelled from the granular structure. The inflow or outflow of fluid in the granular system represents negative and positive pore pressure changes ΔP, respectively. Figure 2.3 shows the strength and pore pressure change ΔP evolution for saturated dense coarse soils with different grain size distributions. Note that samples developing more deviatoric strength correspond to those having the greatest negative pore pressure change ΔP. Also note that negative ΔP is greater in samples with greater Cu, which are samples associated with high packing fraction, and with a tendency to dilate.

Geophysical mass flows, like landslides or debris flows, are part of the constant changes of the landscape and the mechanisms that trigger them are normally related with climatic, volcanic and seismic activity [23–25], or even by anthropogenic reasons like the construction of infrastructure or the change of the land usage [26]. Essentially, all these potential triggering scenarios are responsible for leading soil deposits to have stress states with shear stresses above the Mohr-Coulomb failure criterion $\tau = \sigma' \tan\varphi$, where φ is the material's angle of

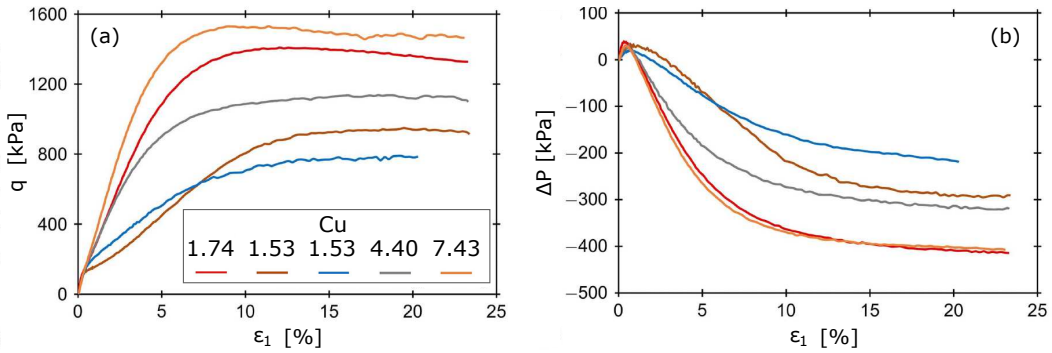

Figure 2.3. (a) Deviatoric effective stress q and (b) changes of the pore fluid pressure ΔP produced by the vertical strain ϵ_1 from an undrained triaxial test. The line's colour represents the $\mathrm{Cu} = d_{60}/d_{10}$ of the GSD. This figure was adapted from Ahmed *et al.* [22].

internal friction and σ' is the effective normal stress sustained by the grains (see Eq. (2.6)). A sudden increase of P, meaning a decrease of σ', could trigger a local instability, with the potential of transforming into an avalanche. Positive changes in the pore pressure ΔP could obey, among other reasons, to the infiltration of rainwater or variations in the granular packing. For instance, contractions in a granular system produce an excess of pore pressure, or a positive ΔP, expelling fluid from the granular structure, weakening the deposit, and enhancing a collective flow. On the contrary, stabilisation is expected to be controlled by dilatancy and the reduction of pore pressure, equivalent to a negative ΔP [27, 28].

2.2.1 Microstructure and Nature

Granular materials interact through contacts that develop extensive and complex contact force networks [29]. Fig. 2.4 (a) presents the force network of a granular assembly of discs in the residual state and shows the erratic distribution that the force network might have. Strong forces (i.e., forces greater than the average) tend to align in the direction of the major principal stress, normally perpendicular to the shear direction, but there are many other force paths without a clear direction. The force network of granular materials exists because of the sum of individual contacts between two grains that enchain the entire network.

The contact between two grains is described by the branch length vector $\boldsymbol{l}_b$, which is the vector joining the grains' centroids, and the contact force vector $\boldsymbol{f}$. For the grains in contact, a the local axes $(\boldsymbol{n}, \boldsymbol{t})$ are defined, being $\boldsymbol{n}$ the unit vector normal to the contact and $\boldsymbol{t}$ the tangential unit vector. The force contact vector $\boldsymbol{f}$ is the sum of the normal and tangential contributions as $\boldsymbol{f} = f_n\boldsymbol{n} + f_t\boldsymbol{t}$ where f_n and f_t are the magnitude of the normal and tangential force, respectively. Fig. 2.4 (b) shows the local geometry of two grains in contact.

In the force network, forces are classified as strong $(f_n/\overline{f}_n > 1)$ and weak $(f_n/\overline{f}_n < 1)$, being $\overline{f}_n$ the overall average normal force. The latter, the weak forces, are the majority in a force network and their number decays as a power law. On the contrary, the number of strong forces decays exponentially [30]. In polydisperse granular materials, the force chains principally connect large grains, excluding small grains from the network. As the level of polydispersity increases, the force network becomes more inhomogeneous, and the number of very small

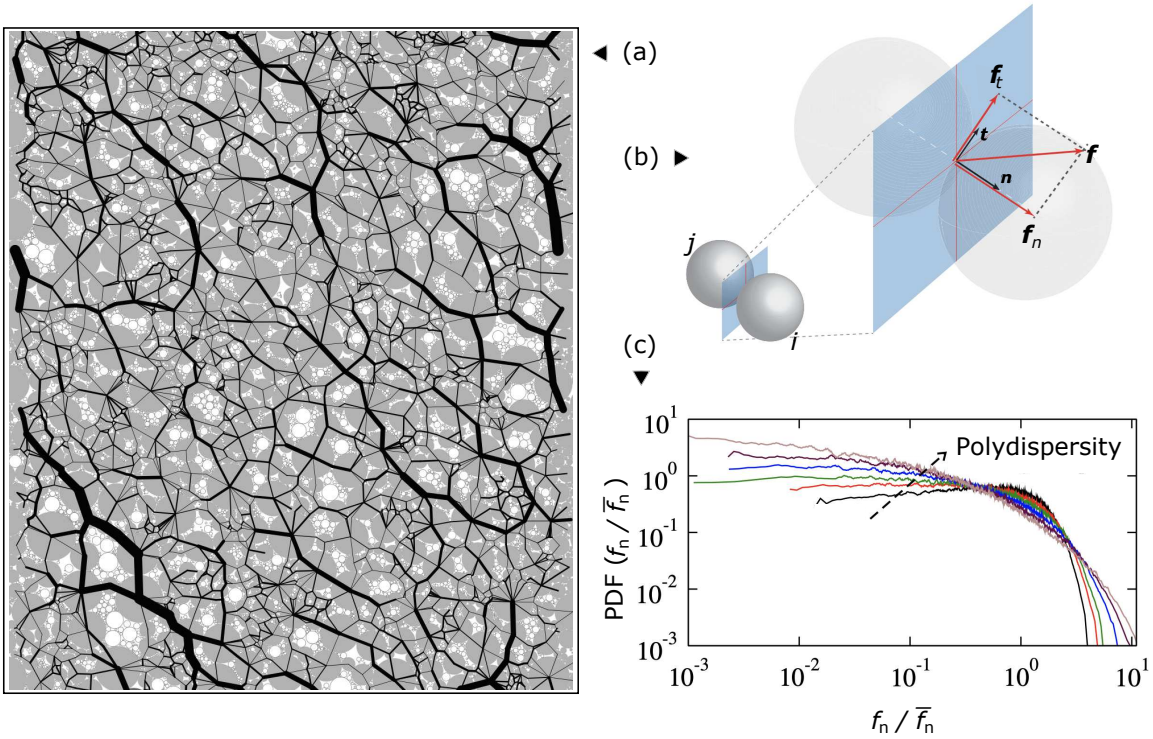

Figure 2.4. (a) Snapshot of the force network developed by a sample of polydisperse disks in the residual state. (b) Local geometry of the contact of two grains (i, j), indicating the tangential vector force $\boldsymbol{f_t}$, the normal force $\boldsymbol{f_n}$ and the resulting force $\boldsymbol{f}$. (c) Probability distribution function PDF of the normal forces f_n normalised by the overall average $\overline{f}_n$ showing the effect of increasing polydispersity. In (a), the thickness of the black lines is proportional to the normal force magnitude f_n and the white disks represent floating grains (i.e., grains with one or none contact). Figures (a) and (c) were adapted from Voivret *et al.* [31], and figure (b) was adapted from Cantor *et al.* [32].

forces and very strong forces increases, widening the forces' probability distribution function [31, 32]. Fig. 2.4 (a) shows the force network of a highly polydisperse sample of discs and Fig. 2.4 (c) shows the probability distribution function of the normal forces indicating the effect that polydispersity has on it.

For granular materials, the stress tensor $\boldsymbol{\sigma'}$ can be interpreted as a static equilibrium between the boundary and internal forces as:

$$\boldsymbol{\sigma}'_{ij} = \frac{1}{V} \sum_{c \in V} \boldsymbol{f}_i \boldsymbol{l}_{bj}. \tag{2.7}$$

This stress tensor is built with of the product $\boldsymbol{f l_b}$, which represents the contact's momentum, of all contacts c belonging to the system's volume V [33]. From the stress tensor, that can be obtained at any instant, it is possible to compute the principal stresses and, with them, the deviatoric stress q and the mean stress

$$p = \frac{\sigma_1 + \sigma_3}{2}. \tag{2.8}$$

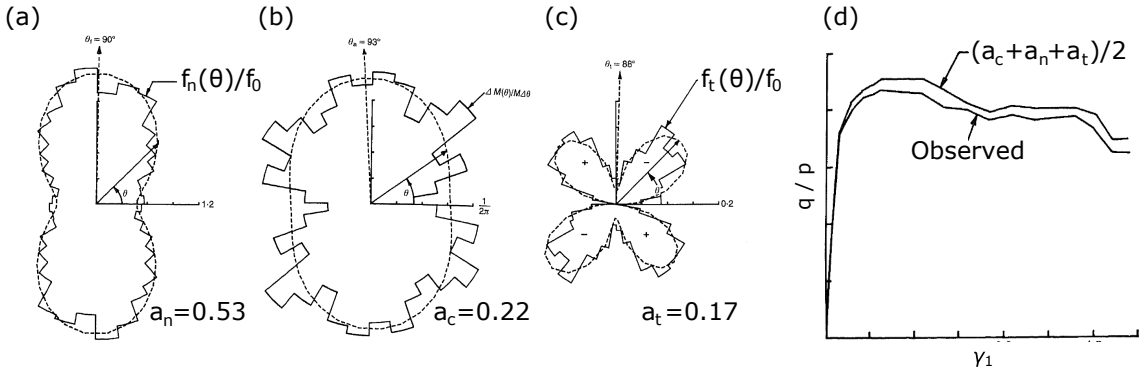

Figure 2.5. Radial distribution of the (a) contacts' direction, (b) normal forces and (c) tangential forces at the peak strength of a biaxial test simiulated with monodisperse discs. Distribution are fitted (dashed lines) with the second-order Fourier expansions in Eq. (2.9a), (2.9c), respectively. In (a), N_c refers to the number of contacts. The figure (d) presents the evolution of the deviatoric stress as q/p for a compression test and compares the result with the stress obtained with the sum of the coefficient of anisotropy (see Eq. (2.10)). This figure was adapted from Rothenburg & Bathurst [34].

The mean stress p computed with Eq. (2.8) applies for two dimensions or systems that can be assumed as two dimensional. For three dimension problems $p = (\sigma_1 + \sigma_2 + \sigma_3)/3$. The construction of the stress tensor $\boldsymbol{\sigma'}$ (Eq. (2.7)) depends on the contacts' vector forces $\boldsymbol{f}$ and vector branch lengths $\boldsymbol{l_b}$. The latter represents the system's fabric (i.e., geometrical organisation) and can be analysed with the radial distribution of the contacts' $P(\theta)$ and the radial distribution of branch lengths l_b that compose the contact network. During shear deformation, the contacts of the system tend to align in the direction of the major principal stress and decrease in the direction of the minor principal stress. This leads to a remarkably anisotropic distribution of contacts $P(\theta)$ [34]. The other feature of the system's fabric, the distribution of $l_b(\theta)$, shows a distribution that, in the case of monodisperse spheres (or discs) grains, has the same radio without anisotropy. However, in polydisperse samples, the disorder of $l_b(\theta)$ increases and larger branch vectors tend to align with the direction of the major principal stress [31, 32].

The vector forces can also be represented in a radial distribution, indicating the averaged magnitude of normal f_n and tangential forces f_t discretized in steps $\Delta\theta$. In general, the shape of the normal force distribution is similar to that of the contact distribution, although there is a remarkable difference arising from the strong and weak forces. Strong normal forces are carried by the contacts aligned with the major principal stress. On the contrary, weak normal forces are mainly in the direction of the minor principal stress. Last, the distribution tangential forces f_t presents four peaks that are rotated $\pm 45°$ from the major principal stress and tend to zero in the direction of the principal stresses [31, 32, 34, 35]. Fig. 2.5 presents the radial distribution of (a) contacts, (b) normal forces and (c) tangential forces for a simulation of a biaxial test with monodisperse discs.

All the radial distributions of $P(\theta)$, $l_b(\theta)$, $f_n(\theta)$ and $f_t(\theta)$ can be well approximated with a second-order Fourier expansion as:

$$P(\theta) \simeq \frac{1}{\pi}\{1 + a_c \cos 2(\theta - \theta_c)\}, \tag{2.9a}$$

$$l_b(\theta) \simeq \bar{l}_b\{1 + a_l \cos 2(\theta - \theta_l)\}, \tag{2.9b}$$

$$f_n(\theta) \simeq \overline{f_n}\{1 + a_n \cos 2(\theta - \theta_n)\}, \tag{2.9c}$$

$$f_t(\theta) \simeq -\overline{f_t} a_t \sin 2(\theta - \theta_t), \tag{2.9d}$$

where a_c, a_l, a_c, a_n and a_t are the parameters defining the anisotropy of the contact, branch length, normal force and tangential force distributions, respectively. Additionally, the angles θ_c, θ_l, θ_n and θ_t represent the preferential orientation of each distribution [31, 34, 36]. In Eq. (2.9b - 2.9d), the constants $\bar{l}_b$, $\overline{f}_n$ and $\overline{f}_t$ refer to the overall average branch length, normal force magnitude and tangential force magnitude, respectively.

The anisotropies are parameters that characterise the microstructure of granular materials and their evolution while shearing shows similar to the strength evolution. From the micromechanical perspective, the strength of a granular material is the addition of the contribution of different mechanisms of load transmission defined in the fabric and force networks [34]. These contributions and the shear strengh of granular materials are related as:

$$\frac{q}{p} \simeq \frac{1}{2}(a_c + a_l + a_n + a_t). \tag{2.10}$$

The mean stress form of Eq. (2.10) applies for two dimensions or systems that can be assumed as two dimensional. For three dimension problems $q/p \simeq (2/5)(a_c + a_l + a_n + a_t)$ [37]. Fig. 2.5 (d) shows the strength evolution q/p of a biaxial test simulated with monodisperse discs and compares q/p with the estimation of Eq. (2.10). The resemblance of between q/p and the sum of the anisotropies is not exclusive of monodisperse discs and it also works with polydisperse discs [31] and spheres [32], irregular polyhedra [36, 38], and it has been extended to monodisperse materials deformed at different shear velocities [35].

2.2.2 Residual (or Steady) State

The peak and residual strength of granular materials are important for characterising the material behaviour. The peak strength has great relevance in cases where large deformations are not considered, like in slope stability or ground foundations. On the contrary, the residual strength is of primary importance in the design of processes involving large deformations, like in a landslide [39, 40]. Therefore, in this study, we focus on the residual strength of granular materials (see Fig. 2.2).

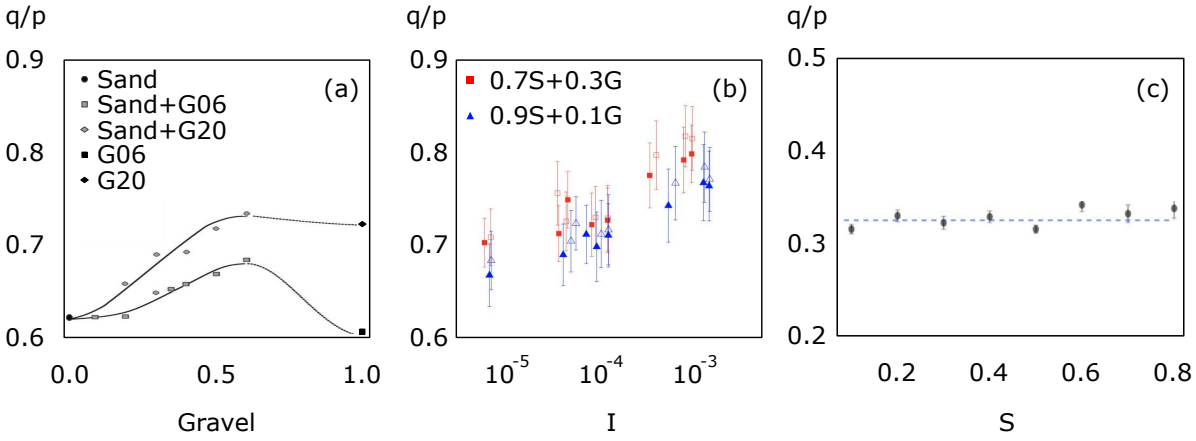

Figure 2.6. Residual strength of granular materials. (a) Strength of different mixes of sand and gravel, varying the gravel concentration and comparing the effect of the gravel G06 with uniformity coefficient Cu = 1.59 and the gravel G20 with Cu = 2.35 (see section 2.1 for more information about Cu). (b) Strength of mix of sand S and gravel G in two concentrations, varying the shear velocity here presented as the inertial number I (see section 2.2.3 for more information about I). (c) Strength of spheres, varying the polydispersity level here presented as the size span $S = (d_{\max} - d_{\min})/(d_{\max} + d_{\min})$. Note in (c) that the vertical limits were changed. Figures (a), (b) and (c) were adapted from Simoni & Houlsby [41], Liu *et al.* [42] and Cantor *et al.* [32], respectively.

It is well known that the shear strength of granular materials depends on the grain shape, mineralogy and hardness, or friction coefficient between grains [43]. These features, and many others, have been systematically studied through numerical simulations and have shown that granular materials augment their capacity to mobilize residual strength when increasing the grain's angularity [36], elongation [44], shape irregularity [45], convexity [46], and/or the rolling friction resistance [47]. Polydispersity, as a fundamental feature of granular materials, has also been explored in order to identify its influence on the shear strength. However, this relationship remains a matter of debate, specially in the soil mechanics community, even if the question is restricted to the residual effective friction $\mu = q/p$. On the one side, some experimental studies have shown that μ decreases with the level of polydispersity [48–50], while others have observed that μ increases with polydispersity [22, 41, 42, 51–53]. In the framework of Critical State Soil Mechanics, some studies have explored the effects of the GSD and shown that the critical state of soils is independent of the size [54] and level of polydispersity [55, 56]. There is thus no agreement on this effect in the soil mechanics community. On the other side, a good number of numerical studies have shown that μ is independent of the packing fraction and the GSD's shape [17, 31, 32, 57–59], explaining this independence as a compensation between the loading mechanisms of the fabric and force network (see Section 2.2.1). There is thus agreement on the independence of μ and polydispersity in the granular-DEM community. There is not an correct or wrong answer for understanding the contradictory results found in previous experimental studies, the results that lead to different conclusions might be influenced by the varying rugosity inherent in polydisperse granular materials, especially in geomaterials, or by a small size-to-system scale where predetermined shear paths could coincide with large

grains, as could occur in a direct shear test. Fig. 2.6 presents experimental and numerical results that indicate different effects that polydispersity has on the residual effective friction μ. The residual effective friction μ, also interpreted as an indicator of energy dissipation, is an important feature of granular flows that controls, for example, their final deposit. Therefore, an intuitive question is about the effect that polydispersity has on the strength of granular materials. The fact of having conclusions pointing to different results from different communities shows a gap of knowledge, but most importantly, it shows that there is interest to clarify the effect that polydispersity has on the residual strength of granular materials.

2.2.3 Inertial Effect

In dry granular flows, the collective motion of the grains is governed by the system's inertia. Assuming rigid grains within a large system and utilising dimensional analysis, a single dimensionless number that governs the system was identified [60, 61]. This dimensionless number relates the material's general deformation time and the time of a grain relaxation (or depositing) and is called the Inertial number

$$I = \frac{\dot{\gamma} d}{\sqrt{P_{\mathrm{c}}/\rho_{\mathrm{s}}}}, \tag{2.11}$$

with $\dot{\gamma}$ being the shear rate, P_{c} being the confinement pressure, ρ_{s} being the grains' density, and d being a characteristic grain diameter.

During flow, and depending on the inertial level, granular materials can exhibit behaviours resembling those of solids, liquids, or gases. Granular flows can be classified into three regimes according to the inertial number I, each of which exhibits *state of matter-like* characteristics. The *quasi-static* regime ($I < 10^{-3}$), where granular materials behave like solids, neglects the flow inertia and grains interact through contacts of long duration. The *dense regime*[¶] ($10^{-3} < I < 1$) of granular flows occur when the inertia becomes important and grains interact through contacts of short duration. For this regime, granular flows are expected to behave like viscous fluids. Last, there is a regime where granular materials behave like gases ($I \gg 1$) and is characterised by the rapid motion of grains with few contacts that principally interact through collisions. [2, 62].

The inertial number I, as a dimensionless quantity that controls granular flows, is a standard for implementing friction $\mu(I)$ and volume laws $\phi(I)$ [62–64]. For a granular systems subjected to increasing shear velocity, the strength in the residual state increases [35, 65], and if it is allowed to change its volume, the system expands, leading to a reduction of the packing fraction ϕ. The fact that the shear strength increases with the flow inertial level can be understood as a change in the grains contact forces. As the inertia of a granular flow increases, the force magnitude between grains increases as well [66, 67]. Additionally, the grains start to interact through contacts of short duration that have high linear momentum transfer [68]. From a microstructure perspective, in granular flows with $I > 0.1$, the contribution of the normal

[¶]The *dense regime* is also commonly known as the *inertial regime*; however, for avoiding confusions with a latter definition, we decided to call the regime of fluid-like behaviour as *dense regime*.

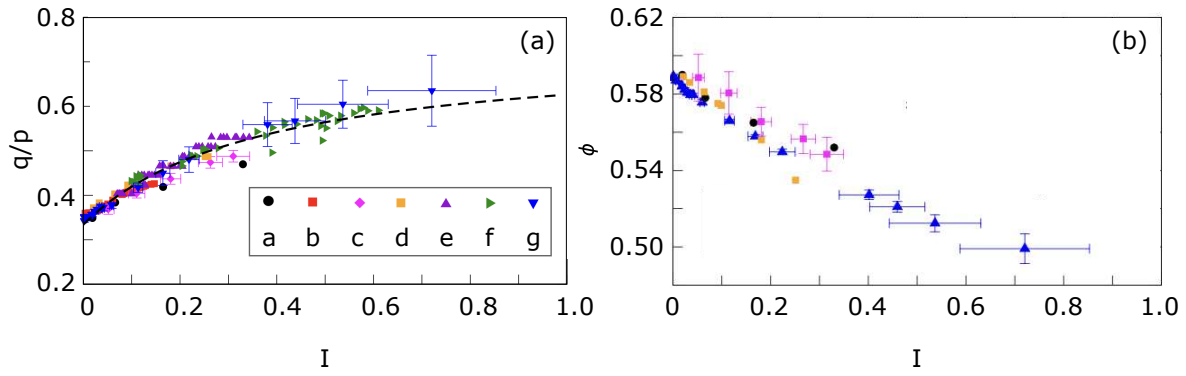

Figure 2.7. (a) Shear strength $\mu = q/p$ and (b) packing fraction ϕ as a function of the inertial number I. The markers labeled as a, b, c, d, e, f and g present data from the studies of Silbert *et al.* [70], da Cruz *et al.* [61], Azéma *et al.* [35], Baran *et al.* [71], Pouliquen [72], Savage [73], and Azéma & Radjaı [69], respectively. This figures was adapted from Azéma & Radjaı [69].

and tangential forces stabilise near a residual value. The increase in strength is attributed to the augmentation of contact disorder (the contact anisotropy a_c) [69]. This implies that the erratic formation and disorder of contacts play a significant role in contributing to the shear strength increase. Fig. 2.7 shows the shear strength and the packing fraction ϕ as a function of the inertial number I for monodisperse granular systems.

Although the study of polydisperse materials has focused on systems with low inertia in the quasistatic regime and has provided a rich understanding of the influence that polydispersity has on the shear strength and micromechanics (see section 2.2.1 and 2.2.2), there are some studies exploring the effect of polydispersity in systems with increasing inertia through simulations [59, 74, 75] and experiments [42], concluding that polydisperse granular materials follow a friction law similar to that of monodisperse materials. Nevertheless, it is still missing a description of a volume law that could possibly describe polydisperse materials that intrinsically have different packing fractions. Moreover, it also lacks a description of the microstructure features of polydisperse granular materials in highly inertial systems.

Lastly, the quantity that controls the flow of granular materials is the inertial number I (see Eq. (2.11)) and it relies on a characteristic grain diameter d. In polydisperse granular materials, the characteristic grain diameter is not an intuitive length to interpret because these materials account for many grain sizes in varied GSD. From the perspective of a continuum material for modelling processes of large deformation, the grain diameter d becomes the foremost variable for describing the material. Rognon *et al.* [76] showed for steady segregated uniform flows that local friction laws $\mu(I)$ work for bidisperse grains and depend on I, taking into account the average diameter of the grains [76]. Other studies with polydisperse materials have proposed the use of a different characteristic d, such as the mean diameter, cubic mean, or the Sauter mean, which is a relationship between the grains' volumen and surface [74, 75, 77, 78]. Thus, there is still no consensus about this characteristic length d for describing polydisperse granular materials.

2.3 | Fluid - Grain

Granular flows occur in varied ambient fluids (e.g., air, water) where grain-fluid interactions significantly influence their behaviour, balancing the forces associated to the collective grains inertia and the ambient fluid viscosity. The influence of the fluid-grain interactions varies and depends on grains (e.g., ρ_s and d) and fluid parameters like density and viscosity. Courrech du Pont *et al.* [79] propose three flow regimes as a function of the Stokes number

$$\mathrm{St} = (\rho_s \Delta\rho g d^3)^{1/2}/(18\eta_f\sqrt{2}) \tag{2.12}$$

and the density ratio

$$\chi = \sqrt{\rho_s/\rho_f}, \tag{2.13}$$

where d is the grain diameter, g is the gravitational acceleration, η_f is the fluid dynamic viscosity, ρ_s and ρ_f are the solid and fluid densities, respectively, and

$$\Delta\rho = \rho_s - \rho_f \tag{2.14}$$

is the density difference between grains and fluid. The three flow regimes and the limits between them are the *free-fall* that occurs for $\mathrm{St} \geq \mathrm{St}^*$ and $\chi \geq \chi^*$, where $\mathrm{St}^* = 10$ and $\chi^* = 4$ are the transition limits to the *inertial* and *viscous* regimes. In the *inertial* regime the grain-grain and grain-fluid drag interactions are strong, and occurs for any pair of St and χ below their transition values and for a ratio $\mathrm{St}/\chi > 2.5$. In the *viscous* regime, the grains' motion is limited by the Stokes velocity, and this regime occurs for $\mathrm{St}/\chi < 2.5$ (see section 2.5.3 for an example of the importance of the parametric space St, χ).

2.3.1 Viscous and Inertial Shears

In section section 2.2.3, we introduced the inertial number I that is the quantity that, under certain assumptions, governs dry granular flows (see Eq. (2.11)). Similarly, for viscous granular flows, there is a single dimensionless number that control the whole system. Assuming that the system is viscous and the grains' density is negligible, that grains are rigid, and that grains interact through hydrodynamics or frictional contacts, the single dimensionless quantity is the *viscous number*

$$J = \frac{\eta_f \dot{\gamma}}{P_c}. \tag{2.15}$$

The constitutive friction and volume laws also can be written as a function of the viscous number as $\mu(J)$ and $\phi(J)$, respectively. The friction coefficient μ is increases continuously as a function of J, while the packing fraction ϕ decreases with the increase of J. The limit where J tends to zero, the friction coefficient and the packing fraction have critical values μ_c and ϕ_c, respectively [80, 81].

In viscous systems, the friction and volume laws depend on J that accounts for the fluid's viscosity and the shear rate $\dot{\gamma}$. In inertial systems, the these laws depend on I that accounts

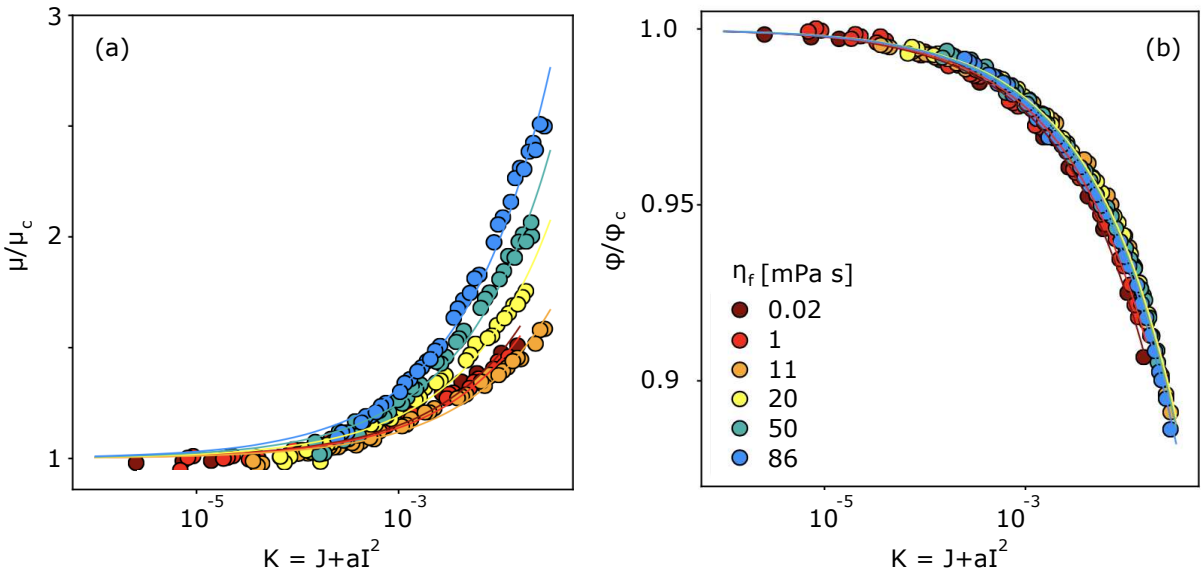

Figure 2.8. (a) Shear stress μ and packing fraction ϕ as a function of the dimentionless number K (see Eq. (2.16)) for monodisperse grains. Both μ and ϕ are normalized by their critical values μ_c and ϕ_c, respectively, when K tends to zero. In the horizontal axis $a = 1/\mathrm{St}$ with $\mathrm{St} = 10$. The markers' colour stands for the fluid's viscosity η_f that includes air and water with $\eta_\mathrm{f} = 0.02$ and 1 mPa s, respectively. This figure was adapted from Tapia *et al.* [84].

for the grains' diameter d and density ρ_s and, again, the shear rate $\dot{\gamma}$. Nevertheless, these two controlling quantities can be unified into a single dimensionless number based on stress addition provoked by the viscous and inertial contributions, represented as

$$K = J + aI^2, \tag{2.16}$$

where a is a constant that stands for the energy dissipation due to the fluid-grain force interaction [82, 83]. The transition between viscous and inertial systems is consider to occur when the viscous and inertial stress have virtually the same magnitude. The study of Tapia *et al.* [84] shows that the transition occurs from viscous to inertial occurs, independently of ϕ, for $a = 1/\mathrm{St}$ with $\mathrm{St} = 10$. Fig. 2.8 shows the friction $\mu(K)$ and the volumne $\phi(K)$ rheology for monodisperse spheres in flows with different fluids.

The friction and volume laws have been extended to transitional flows, evidencing that volume changes follow contractions and dilatancy *paths* determined by the controlling dimensionless number [85] (see also section 2.5.3). Moreover, these rheological laws have been successfully implemented in continuum approaches modeling gravity-driven flows without imposing pressure P_c or porosity ϕ, accounting for changes in fluid pore pressure P, as well as dilatancy and contraction of the solid phase [86].

2.3.2 Interactions

The interactions between the solid and fluid phases add complexity to the study of granular flows. Notably, flows exhibit different behaviours depending on the specific regime they belong to,

which significantly influences flow features like velocity, mobility, and duration. As mentioned earlier, the interaction between the fluid and grains plays a crucial role in determining the flow behaviour. Typically, studies on immersed granular flows consider the buoyancy and drag forces as the primary interactions governing flow. Nevertheless, there are other interactions, such as added (or virtual) mass [87], grain lubrication [88], and hydrodynamic torque [89], which also contribute to the flow behaviour.

Buoyancy

Buoyancy is a force $\boldsymbol{f}_{\mathrm{b}}$ that accounts for the differential fluid pressure that an object, or a grain, has. Although it is not always the case, the buoyancy force is normally assumed to be contrary to the gravity force because the fluid gradient pressure is strong in the gravity's direction. In gravity driven flows, the gradient pressure is principally controlled by g and the buoyancy force could be assumed as $\boldsymbol{f}_{\mathrm{b}} = \rho_{\mathrm{f}} g V_g$ where V_g is the grain's volume. Nevertheless, the grains' collective motion and the momentum transfer with the fluid changes the fluid gradient pressure $\boldsymbol{\nabla} P$ and the buoyancy force is more accurately computed as $\boldsymbol{f}_{\mathbf{b}} = V_g \boldsymbol{\nabla} P$.

Drag

The drag force of an individual grain is a force contrary to the grain's displacement direction and is given by $\boldsymbol{f}_{\mathbf{d}} = \frac{1}{2}\rho_{\mathrm{f}} \boldsymbol{v}^2 C_D(\mathrm{Re}) A_r$, where v is the grain's velocity, A_r is the grain's cross section area perpendicular to v, and $\mathrm{C_D(Re)}$ is the drag coefficient that is a function of the Reynolds number $\mathrm{Re} = \rho_{\mathrm{f}} v d / \eta_{\mathrm{f}}$[‖]. In a granular flow, the drag force of an individual grain is affected by the interactions with the neighbouring grains. This effect can be taken into account by means of a voidage function $g(\phi)$ that multiplies the drag of an single grain as $\boldsymbol{f}_{\mathbf{d}} = g(\phi) \boldsymbol{f}_{\mathbf{di}}$ [94, 95]. This interpretation of the drag force is been found to be satisfactory for dense flows with a packing fraction above the random loose packing ϕ_{rlp} [96]. For polydisperse systems, although alternative methods to compute the drag force have been recently proposed [97–99], a drag model formulation for polydisperse and highly dense granular flows is still a question that generates debate in the community.

The drag force, that accounts for the fluid viscous effects, has a notable effect on the terminal velocity v_t of a grain. A grain falling in a fluid reaches $v_{\mathrm{t}} = \sqrt{(2 V_g \rho_{\mathrm{s}} g)/(\rho_{\mathrm{f}} A_r C_d(\mathrm{Re}))}$ which is the velocity that compensates the gravity force $\boldsymbol{f}_{\mathrm{g}} = V_{\mathrm{g}} \rho_{\mathrm{s}} g$ and the opposite drag force $\boldsymbol{f}_{\mathrm{d}}$[**]. It is easy to interpret that small grains have a lower terminal velocity than big grains; however, for polydisperse systems, the behaviour depends on the bulk interaction and not on individuals grains. For example, the high packing fraction ϕ in polydisperse granular flows reduces the bulk settling velocity compared with the v_t of individual grains [100, 101].

[‖] The drag coefficient C_D for a sphere reduces with the Reynolds number Re and there are several equations to compute the C_D as a function of Re [90–93]. Choosing any of those depends mainly on how the equation satisfies the problem (or situation) faced. Although limited to a range $\mathrm{Re} \approx [1000 - 200000]$ and depending on the considerations made, the drag coefficient for a sphere could also be assumed constant $C_D \approx 0.47$.

[**] For simplicity, the buoyancy force is omitted when computing the terminal velocity.

2.3.3 Common Methods for Solving Grain-Fluid

Granular flows are complex systems that have to be simplified when studied with numerical methods. There are two main approaches for studying granular flows: continuum methods and discrete coupled methods. Each method offers distinct advantages and limitations, but their application offers comprehensive insights of the interactions between solids and the surrounding fluid.

Two-Phase Continuum Approach

The continuum approach as an alternative for simulating granular flows assumes that the both phases, solid and liquid, are continuum phases. The solution of this approach averages the Newton's law of motion for the solid phase and the Navier-Stokes equations for the fluid phase into continuum equations that balance the momentum between both phases [102]. This kind of approach offers a solution that solves solid-solid and solid-fluid problems at small computation cost and allow the simulation of large scale problems, providing averaged results of the solids and fluid velocity, as well as the fluid pressure. As the solids are solved in a coarse scale, their solution depends on the constitute relations applied on them. Pirulli & Mangeney [103] showed, in the context of geophysical flows, that the success of continuum approaches relies on the choice of the appropriate constitutive law and the specification of the rheological parameters.

In the case of polydisperse materials, there are continuum approaches that account for grains of different sizes and are capable of modelling size segregation, but they are limited to few grain sizes [104–106]. Up to date there are not continuum solutions that account for polydispersity and most constitutive and rheological relations rely on the packing fraction ϕ [80, 82, 83] (see Fig. 2.8).

Coupled Discrete Element Methods (DEM)

The discrete element methods DEM coupled with continuum solutions allow the modelling of solids as individual grains, obtaining state variables impossible to get from a continuum approach such as the position, velocity and the forces on each grain. The discrete modelling provides a tool for studying granular materials as they are, a divided media. The physics of the solid phase is well represented by individual grains in DEM, but its applicability is constrained by the scale of the processes it can address. Current computational capacity allows the simulation of DEM models with approximately hundreds of thousands of grains, which suffices for triaxial tests[††] but falls short for accurately modelling, for example, landslides due to the much larger number of grains involved.

Through DEM, Newton's equations of motion are solved in a time step for obtaining the grains' forces and trajectories. Then, these forces and trajectories are used, in an iterative way, as constraints imposed on the neighbouring grains and boundaries. DEM commonly refers to the smoothed and explicit solutions as it was initially conceived [107]. Under this

[††]A triaxial test made in a cylindrical sample of 7 cm diameter and 14 cm heigth, a packing fraction $\phi = 0.6$, and grains of 1 mm diameter, requires 617400 grains.

idea, the time step for solving the grains' interaction must be small because of the explicit time integrators. During the time step, the interpenetration between grains is allowed for obtaining the elastic and plastic deformations, and the reacting forces between them. On the contrary, there exist a 'family' of DEM called Non-Smooth Contact Dynamic (NSCD) that considers the grains as perfectly rigid bodies for which deformation and interpenetration are not allowed [108, 109]. This method accounts for main characteristics of contact and friction in a multi-bodies problem, and the solver requires long time steps that are time consuming [110]. Despite NSCD consuming a long time for solving body interactions in a time step, the fact that it does not allow interpenetration makes it a well adapted methodology for granular flows especially if accounting for polydisperse systems.

In a coupled DEM simulation, the resulting forces of the grain-fluid interactions are added to those obtained by solving Newton's equations. The forces added to the grains from hydrodynamic interactions depend on the representation of the fluid that interacts with the grains. There are two main fluid methodologies for coupling the fluid-grain interactions and the grain-grain interactions obtained with DEM. The fine-scale solutions, like Smoothed Particle Hydrodynamics (SPH), Immersed Boundary Method (IBM), Distributed Lagrange Multiplier/Fictitious Domain (DLM/FD), or Lattice Boltzmann Methods (LBM); and the coarse-graining solutions, like the Particle-in-cell (PIC) or the Volume-Average-Navier-Stokes (VANS).

Fine-Scale solution

There are methods that couple the DEM with a fine-scale solution for the fluid. In these methods, the scale used for solving the fluid is smaller than the grain scale (e.g., 10 - 16 times smaller than the grain diameter d), providing a full solution capable of solving in detail the fluid-grain interactions in the pores and in the grains' boundaries [111, 112]. These kind of solutions allow the study of flows without the need of, for example, constitutive laws; however, the small scale solution results in CPU time expensive simulations. For polydisperse simulations, this issue is intensified because the fluid scale has to be chosen as a function of the smallest grains [113].

Coarse-Graining solution

Contrary to fine-scale solution, the Coarse-Graining provides a coupled solution of the grains with a fluid solved as continuum representation at a larger scale (e.g., 2 - 5 times larger than d). This kind of approach offers a good solution of the fluid phase that could transit from being fully fluid to being a mixture of dense grains at a small computational cost [85, 114, 115]. However, an issue in Coarse-Graining approaches arises from the different scales that represent the fluid and solid phases. The balance between the fluid phase, solved at the coarse scale, and the solid phase, solved at the grain scale, has to be parameterised and a solution at the small scale does not exist because fluid state variables (i.e., velocity and pressure) are not available at that scale. Therefore, in this framework, normally effects such as the hydrodynamic torque and lubrication forces are neglected.

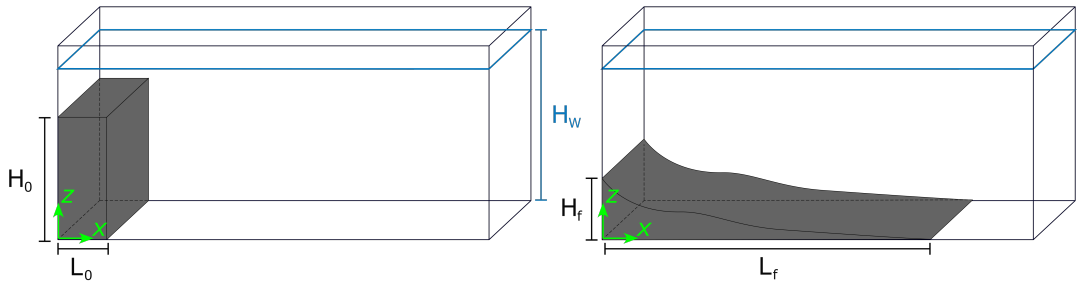

Figure 2.9. Sketch of the granular column collapse configuration. The column initial geometry is characterized by an initial heigth H_0 and length L_0, having an aspect ratio $A = H_0/L_0$. The column collapses by self weight over a horizontal plane, and after the collapse a final deposit is described by a height H_f and length L_f. For immersed columns, the fluid level is H_w.

2.4 | Study Case: Granular Column Collapse

There are many configurations for studying granular flows. In some of them, the flow is imposed by the boundaries and does not account for gravity like in the shear plane [61], the annular shear [116], or the annular shear with split bottom [3]. In others, the flow is driven by gravity like in the Vertical Chute [117], the Incline Plane [72], the Heap Flow [118], and the Rotating Drum [79]. All these configurations have a common feature, they produce steady flows with a nearly constant deformation rate $\dot{\gamma}$. Granular flows occur in different scenarios, leading to transitional flows where $\dot{\gamma}$ is not constant and flows experience phases of acceleration and deceleration, like in debris flows or landslides. A benchmark study case for transitional granular flows is the *Granular Column Collapse* that bridges experimental and numerical observations with geophysical granular flow behaviours [119].

In the Granular Column Collapse configuration a granular assembly is built with an initial height H_0 and an initial length L_0, having an aspect ratio

$$A = L_0/H_0 \tag{2.17}$$

is let to collapse by self-weight on a unique principal direction over a horizontal plane [120]. The column collapse sequence begins with a vertical and an horizontal acceleration of grains and it is followed by a stage of constant horizontal spreading where the collapse front displaces with nearly constant velocity U. Then, the collapse decelerates and stops, leaving a final deposit with height H_f and runout L_f [121, 122]. Fig. 2.9 presents a sketch of the Granular Column Collapse in the initial and final configurations.

The Granular Column Collapse is widely used and many features can be varied and studied on it. The most common column configurations are the axisymmetric column, that has an initial radius r_0 and collapses on a (X, Y) plane, and the semi-two-dimensional column with initial length L_0 [123] (see Fig. 2.9 for this latter configuration). Changes in the column initial configuration, like the initial cross-section, can be varied for identifying the effect on the column collapse [124]. There is also a planar column collapse configuration that allows, among other things, to identify the motion of individual grains [125, 126]. Moreover, certain

features of the column configuration can be modified aiming to explore the influence of the slope on the collapse [127] or the formation of waves produced by the collapse [128, 129].
Previous works have focused on the influence that grain, fluid and column variables have on the column collapse. Studies have focused on the effects that the column aspect ratio A [130, 131], the fluid's density ρ_f and viscosity η_f [132, 133], the grains' friction and restitution coefficients [134], the grain's shape [135], the grain's density ρ_s [136], and grains' cohesion have on granular flows [137].
The Granular Column Collapse has been widely studied through numerical simulations. Notably, DEM has been one of the most popular tools for studying this configuration, solving the solids interactions at the grain scale and including grain-fluid interactions with coupled simulations in fine-scale solutions, like with the Lattice Boltzmann Method [113], or in coarse-graining solutions like the Volume-Average-Navier-Stokes method [85]. Additonally, rheological models have been satisfactorily implemented in two-phases continuum approaches for studying granular column collapses [86, 138–140].

2.4.1 The Collapse Sequence

In the granular column, once the column is let to collapse, a wedge of grains starts to move vertically and then spreads horizontally. Throughout the collapse process, the granular system loses contacts during their fall and horizontal spreading, but starts to gain contacts again when the collapse decelerates and comes to a halt at L_f [141]. During the collapse process, there is a temporal decrease of the effective stress σ' held by the grains and the bulk is fluidezed, having a fluid-like behaviour even in dry conditions. The evolution of the front[‡‡] position, during the collapse processes, provides information on the entire collapse sequence. With the front position evolution, the collapse stages, the collapse velocity or the column runnout can be easily identified (see Fig. 2.10 (a)).
Granular column collapses have a characteristic stage of steady propagation with nearly constant velocity

$$U = \Delta L/\Delta t. \tag{2.18}$$

Although there are several variables that affect U, it strongly depends on the column H_0 and the collapse flow regime. Bougouin & Lacaze [133] showed that the maximum front velocity is proportional to the theoretical free-fall velocity of a grain falling a height H_0 as

$$U_{ff} = \sqrt{2g^* H_0} \tag{2.19}$$

where g^* is a scaled gravity due to the buoyancy force provoked by ambient fluid density

$$g^* = g\Delta\rho/\rho_s, \tag{2.20}$$

[‡‡]Some authors, especially those from the earth science community, might refer to the front as the *head* of the flow.

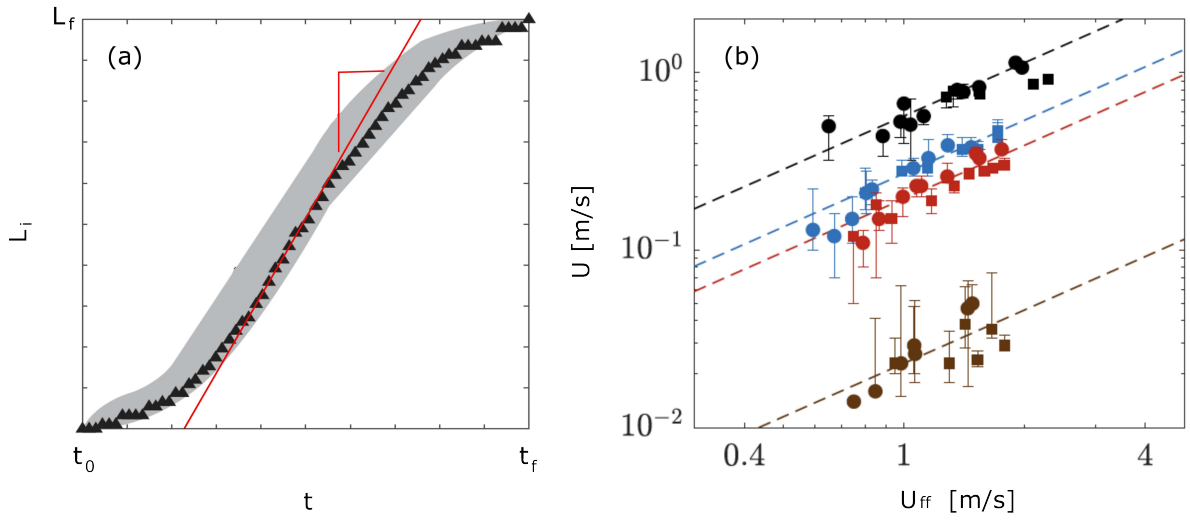

Figure 2.10. (a) Typical evolution of the front position L_i. The red line represents the front velocity during constant spreading U (see Eq. (2.18)). (b) Maximum front velocity U as a function of the theoretical free-fall velocity U_{ff} (see Eq. 2.19) for collumn collapses in the free-fall (black), inertial (blue), viscous-inertial (red), and viscous regime (brown). Figures (a) and (b) were adapted from Pinzon & Cabrera [126] and Bougouin & Lacaze [133], respectively.

and concluded that $U/U_{\mathrm{ff}} \approx [0.024, 0.196, 0.27, 0.55]$ for viscous, viscous inertial[§§], inertial, and free-fall regimes, respectively (see Fig. 2.10 (b)).

It was previously mentioned that there are several variables controlling the collapse velocity and, in general, the collapse sequence. For immersed columns, the initial packing fraction ϕ_0 has an important role in the flow dynamics, notably affecting the collapse initiation, velocity and mobility. The effect of ϕ in granular flows was initially discussed in the works of Pailha *et al.* [142] and Pailha & Pouliquen [143], and extended to granular columns by Rondon *et al.* [9] who showed that initially loose columns start sooner the collapse process and their U is greater compared with dense columns. Rondon *et al.* [9] revealed that the mechanisms controlling the behaviour of dense and loose collapses are similar to the pore pressure feedback mechanism in landslides [27, 144]. Dense columns are delayed and have a slower collapse process because they need to dilate in order to initiate the flow, producing suction and resulting in a negative change of the pore pressure ΔP. The reduction of the pore pressure temporally produces an increase of the effective stress σ' and, consequently, increases the column strength (see Eq. 2.6). On the contrary, loose columns need to contract and expel fluid, provoking positive ΔP and leading to a partial fluidization [9, 145]. Moreover, the effect that the packing fraction has on the column collapse has been well captured by the rheological friction $\mu(J)$ and volume $\phi(J)$ laws [85] (see section 2.3.1), evidencing the contraction or dilatancy processes at the column collapse initiation and an equilibrium when the collapse comes to a halt. Fig. 2.11 (a and b) present the time evolution of the front position and fluid pore pressure changes ΔP beneath the column for a dense and a loose system. Additionally, Fig. 2.11 (c and d) show

[§§]The *viscous inertial* regime is sort of a transitional regime between the viscous and inertial regimes.

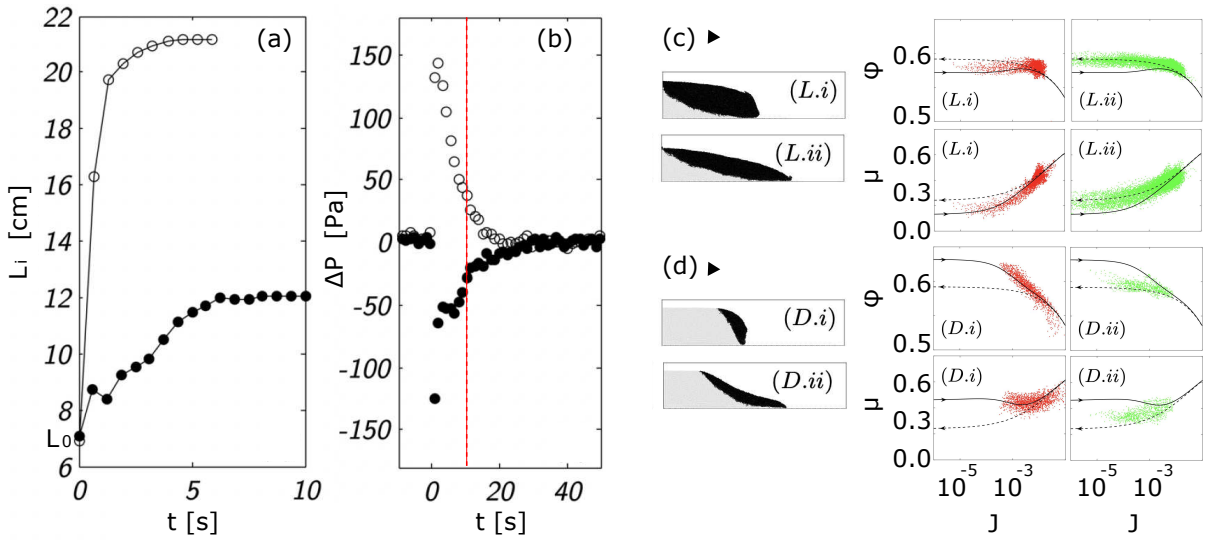

Figure 2.11. Evolution of (a) the front position L_i and (b) the pore pressure changes ΔP beneath the granular column for a pore pressure transducer placed at $\sim L_0/2$. These are the results of immersed column collapses in a mixture of water and Ucon oil (collapse in the viscous regime) with $A \approx 0.67$. The empty ($\circ$) and full markers ($\bullet$) stand for initially loose ($\phi_0 = 0.55$) and dense columns ($\phi_0 = 0.60$), respectively. In (b), the dashed red line is the the x limit of (a) at $t = 10$ s. (c) and (d) show the packing fraction ϕ and the effective friction coefficient μ as function of the viscous number J (see Eq. (2.15)) during two stages of a column collapse, comparing the influence of a loose L and a dense column D. The column collapse sketches of (c) and (d) present motion (black) and motionless grains (grey). Figures (a) and (b) were adapted from Rondon *et al.* [9], and Figures (c) and (d) were adapted from Lacaze *et al.* [85].

the column's packing fraction ϕ and effective friction coefficient μ during two stages of the collapse, comparing the behavior of a loose and a dense column.

In the granular column, the feedback pore pressure mechanism and the influence of ϕ have been mainly reported for collapses in the viscous regime, both numerically and experimentally. However, there are no results evidencing the effect of ϕ on columns within other flow regimes, probably because of the rapid dissipation of excess pore pressure. Despite previous studies that have well identified the influence of pore pressure changes on the initiation of collapse, it only represents the initial stage of the collapse process, and its role in the propagation of the collapse remains unexplored. Lastly, the influence of polydispersity on immersed granular columns has not been studied yet. Due to the increasing packing fraction ϕ that polydispersity generates, immersed granular flows might be strongly influenced by pore pressure changes, even in the inertial regime.

2.4.2 What Does the Final Deposit Tell About the Collapse?

The collapse of a granular column, and a debris flow, stops when the energy has being dissipated and leaves a deposit characterised by a final runout distance L_f and height H_f. The deposit geometry is a macro representation of the effective friction coefficient μ of the granular materials that compose the debris flow [146, 147] or the granular column [134, 148,

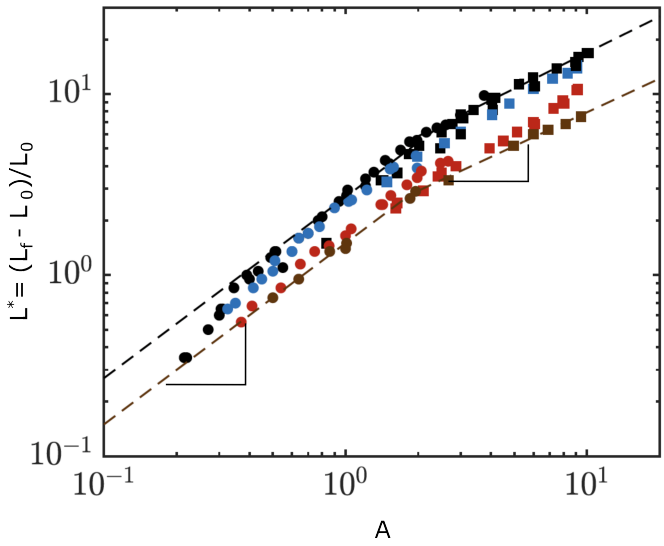

Figure 2.12. Normalised final runout L_f as a function of the column aspect ratio A. The marker colour indicates collapses in the free-fall (black), inertial (blue), viscous-inertial (red), and viscous regime (brown). The dashed lines indicates the best fittings for the free-fall and intertial regimen, and viscous-inertial and inertial regime according to Eq. (2.22). Note that the slope varies beetween short and tall columns ($A \approx 2$). This figure was adapted from Bougouin & Lacaze [133].

149]. Several studies have shown that the mobility of granular columns, also understood as L_f, or in its normalised form

$$L^* = \frac{L_f - L_0}{L_0}, \tag{2.21}$$

increases and scales with the aspect ratio A for different flow regimes [122, 130, 132, 133, 136]. In general, when the grain-fluid drag interaction augments, the final runout decreases because the viscous force exerts an additional resistance to the grain's motion. Moreover, the scale between the column A and the final runout follows a power law function

$$L^* = aA^b \tag{2.22}$$

that distinguishes short and tall columns, having tall columns with a power index $b < 1$ and short columns with $b = 1$ [120, 122, 126, 133, 150, 151]. Although there is not an exact A for classifying columns, normally short columns have $A \lesssim 2$ and tall columns have $A \gtrsim 2$ (see table 2.1). The distinction between short and tall columns arises from the collapse sequence. Short columns spread horizontally since the beginning of the collapse, while tall columns have a first stage of free-fall, followed by a stage where grains collide, dissipating energy and augmenting the number of contacts, and then spread horizontally [141]. Fig. 2.12 presents data of an extensive experimental campaign exploring the effect of A in monodisperse column collapses in different regimes.

A motivation for studying granular flows is to understand their behaviour when systems with different grain sizes are considered, and then link observations on small scale systems with those found in nature (i.e., volcanic avalanches, debris flows). Grain size segregation is an

intrinsic phenomenon in granular materials under shear, developed when differences in size or density are found in the constituting grains [105]. Previous works observed that the mobility of bidisperse granular columns augments due to a segregation layer [152, 153]. This effect is enhanced when the ratio between big and small grains increases, and when the column is immersed [154]. The mobility of columns is also affected by the heterogeneity of grain layers of different sizes, increasing the runout distance of initially segregated columns [149, 155]. For polydisperse systems, numerical studies have pointed out that mobility increases with polydispersity [156], and have argued that small grains enhance mobility because they lubricate the system [157]. However, it was found that the lubrication mechanism is a biased interpretation of small system-to-grain size ratio and showed that the mobility of dry granular columns is independent of polydispersity [59]. This latter result was supported with the independence of the shear strength of polydisperse granular materials when they reach a residual stage at large deformation [32, 38, 45]. Despite these previous works, the effect that polydispersity has on immersed granular columns remains still insufficiently investigated.

2.4.3 Mobility Models

In the study of granular flows, mobility models provide a simplified interpretation of a complex process. These models relate granular flows of different scales with the initial and/or flow conditions. Normally, these models consider variables from the column initial geometry and the collapse kinematics.

The model that scales the column final runout L^* and the initial aspect ratio A (see Eq. (2.22)), although simple, comes from a force balance between the basal frictional force, as a function of the front velocity U, and an opposing force related to a reference wedge weight [123]. Among several authors, this scaling normally collapses L^* and A in a linear trend (i.e., Eq. (2.22) with $b = 1$) for short columns and in a trend with a lower exponent ($b < 1$) for tall columns. The fact that b reduces for tall columns stands for a variation of the effective coefficient that links A and L^*. Despite the break in the tendency that remarks an issue of continuity, this scaling is valid for different flow regimes and a wide range of aspect ratios; nevertheless, the parameters a and b and even transitioning A considerably varied among previous studies (see Table 2.1). Fig. 2.13 presents the trends found by different authors according to Eq. (2.22). Moreover, a case that does not follow the frictional approach given by Eq. (2.22) is the one influenced by the initial packing fraction ϕ_0 (see Fig. 2.11). Rondon *et al.* [9] showed that ϕ_0 affects both the collapse velocity U and the final column runout L^*, and proposed that final column runout could be linked with the initial column variables (A, ϕ_0), but did not focus on the collapse kinematics.

Other studies have shown a link between the column mobility and certain features of the collapse kinematics. Considering the the motion at the grain scale, Topin *et al.* [132] proposed a scaling with the analogy of a falling grain subjected to a viscous drag force, and found a satisfactory relationship between L^* and the peak horizontal kinetic energy held by a grain $E_{\mathrm{g}}^{\max}$. This scaling collapses L^* and $E_{\mathrm{g}}^{\max}$ in trends which slopes depends on the mixture's effective viscosity (see Fig. 2.14). Other studies have proposed a scaling considering the

Table 2.1
Summary of the values a and b in the scaling between the column aspect ratio A and the column mobility L^* in Eq. (2.22) reported by different authors. In the table, A^* refers to the transitional aspect ratio between short and tall columns, and the sub-indexes s and t stand for the reported values for short and tall columns, respectively. In the *Regime* column, Exp and Num in the brackets refers to experimental and numerical results, respectively. This list is organised chronologically. The information presented as '-' was not reported by the authors.

Author(s)	Regime	A^*	a_s	b_s	a_t	b_t
Lajeunesse *et al.* [123]	[Exp] Free-fall	3	1	1	1	0.67
Staron & Hinch [130]	[Num] Free-fall	-	3.25	0.7	3.25	0.7
Meruane *et al.* [122]	[Num] Free-fall	3	-	1	-	0.56
Lagrée *et al.* [140]	[Num] Free-fall	7	2.2	1	3.9	0.7
Rondon *et al.* [9]	[Exp] Viscous	-	-	0.5	-	0.5
Topin *et al.* [132]	[Num] Free-fall and Inertial	4	2.45	1	4.3	0.6
Topin *et al.* [132]	[Num] Viscous	4	1.21	1	1.5	0.87
Bougouin & Lacaze [133]	[Exp] Free-fall and Inertial	2	2.7	1	3.7	0.64
Bougouin & Lacaze [133]	[Exp] Viscous-Inertial and Viscous	2	1.5	1	1.9	0.64
Pinzon & Cabrera [126]	[Exp] Inertial	-	1	0.74	1	0.74
Lee [127]	[Exp] Inertial	-	1.31-1.96	1	1.31-1.96	1
Cabrera & Estrada [141]	[Num] Free-fall	2.38	3.18	1	3.73	0.8
Sarlin *et al.* [158]	[Exp] Free-fall	3	1.85	1	2.67	0.67

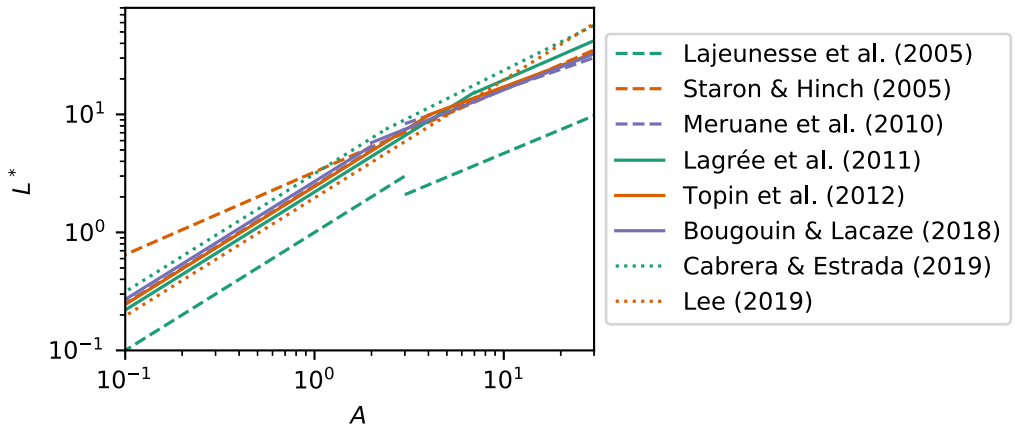

Figure 2.13. Scaling between the normalised final runout L^* and the column aspect ratio A with the trends found by different authors according to Eq. (2.22). This figure was made with the values of (a, b) and the transitioning A between short and tall columns reported by Meruane *et al.* [122], Lajeunesse *et al.* [123], Staron & Hinch [130], Topin *et al.* [132], Bougouin & Lacaze [133], Lagrée *et al.* [140], and Cabrera & Estrada [141] and Lee [127].

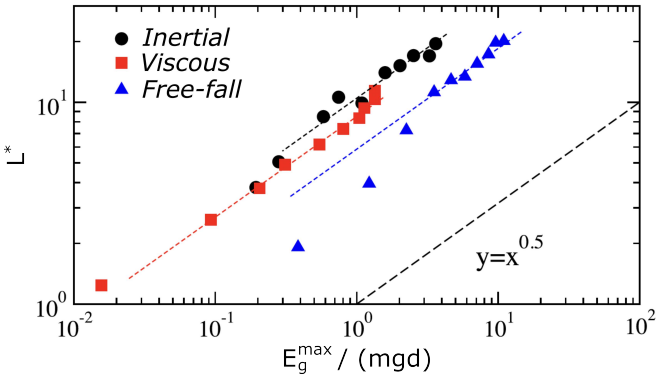

Figure 2.14. Normalised runout distance L^* (see Eq. (2.21)) as a function of the grain peak horizontal energy $E_{\mathrm{g}}^{\max} = mv_{\mathrm{x}}^2/2$ normalised by the grain characteristic energy mgd, where d is the grain's diameter, m is the grain's mass and v_x is the grain's horizontal velocity. The markers' shape and colour indicates the granular column collapse flow regime. This figure was adapted from Topin *et al.* [132].

motion at the flow scale [159–161]. Notably, the work of Yang *et al.* [159] propose a scaling between L^* and the Froude Number $\mathrm{Fr} = U/\sqrt{\Delta\rho g h_{\mathrm{fr}}/\rho_{\mathrm{f}}}$, with h_{fr} being the height of the collapse front, that can be extended to granular flows of different scales. These models work well for flows with monodisperse grains, but depend on fitting parameters or flow variables, such as the flow average height h_{fr} or the peak energy of a single particle $E_{\mathrm{g}}^{\max}$, that are a variables difficult to interpret in transitional flows. Therefore, a model that links column mobility and the collapse kinematics and that can account different grain sizes is still missing.

2.5 | Thesis Overview

The review of the bibliography on granular materials, and specifically on granular flows, allowed us to identify missing elements on this matter. Our objective is to address these identified gaps and provide answers to the open questions presented in Chapter 1, and highlighted and discussed in this chapter. In the following subsections, we present a summary and motivation of the work done, with the specific aim of addressing these key unresolved issues.

2.5.1 Triaxial Experiments: Quasi-static Granular Flows

We have discussed the importance of the residual strength of granular materials on granular flows and the relevance that it has in processes that involve large deformations. The effect that polydispersity has on the residual state of granular materials is still a matter of debate (see section 2.2.2). Therefore, we aim to conduct a set of systematic and controlled triaxial test experiments in order to confirm if the shear strengh μ is independent of polydispersity, described in terms of grain size d, size span λ (see Eq. 2.3), and grain size distribution (λ and ι, see Eq. (2.2)). To our knowledge, a systematic experimental campaign aiming to explore the link between polydispersity and the residual shear strength has not yet been presented. Moreover, providing these results with an experimental proof would close a gap of knowledge

between experiments and simulations. The results and findings that aim to answer this question are presented in the Chapter 3.

2.5.2 Shear Cell Simulations: Inertial Granular Flows

Granular flows develop in a wide range of inertial levels. While there is extensive research on polydisperse granular flows with low inertial values, there is a lack of exploration into highly inertial flows with varying polydispersity levels. To address this gap, we conducted a series of DEM simulations of the NSCD type. Our primary focus is to investigate granular flows with different polydispersity levels and various levels of inertia. The main objective of this study is to gain insights into the micro-mechanical processes governing polydisperse granular flows characterized by high inertia. To achieve this goal, we conduct simulations that imitate the shear cell configuration of constant confinement pressure P_c, allowing volume changes. This choice was made because volumetric variations are integral to most flow processes. Our aim is to comprehensively describe the strength and packing fraction of polydisperse granular flows as a function of their inertial levels. Moreover, we aim at understanding the micro mechanical differences between systems with different polydispersity in varying inertial levels. Lastly, we aim to resolve, or at least to contribute to, the debate regarding the characteristic length, or diameter d, that best describes a polydisperse granular flow. The results and findings of this study are presented in the Chapter 4.

2.5.3 Granular Column Collapse

We use the Granular Column Collapse configuration to study the influence of the grain size polydispersity on immersed and dry granular flows driven by gravity. We aim to extend the observations on monodisperse column collapses to polydisperse columns by exploring different Grain Size Distributions GSDs, ranging from relative initially loose to initially dense packings. We focus on clarifying the role of polydispersity on the column collapse sequence, velocity and final runout. To achieve this goal, we undertake both numerical and experimental studies of monodisperse and polydisperse granular column collapses across different flow regimes, ranging from the transitional viscous-inertial regime to the free-fall regime (see Fig. 2.15).

Numerical

In Chapter 5, we present a study conducted with a coarse-graining approach in a coupled Finite Element Method (FEM) with a Discrete Element Method (DEM), simulating the collapse of a granular column in different ambient fluids. The simulation of such systems is computationally expensive due to the large number of grains required for representative polydisperse granular samples, the necessary short computation time step for avoiding particle inter-penetrations on the smallest grains, and the challenging coupling of the momentum transfer from a moving particle cluster to the fluid mesh. Although the solution in the coarse-scale approach results

¶¶Dy column collapse simulations, classified in the free-fall regime, were done without the effect of an ambient fluid (i. e. fluid viscosity and density were set to zero), but for place them in the parametric space St, χ we assumed the ambient fluid with the air viscosity and density.

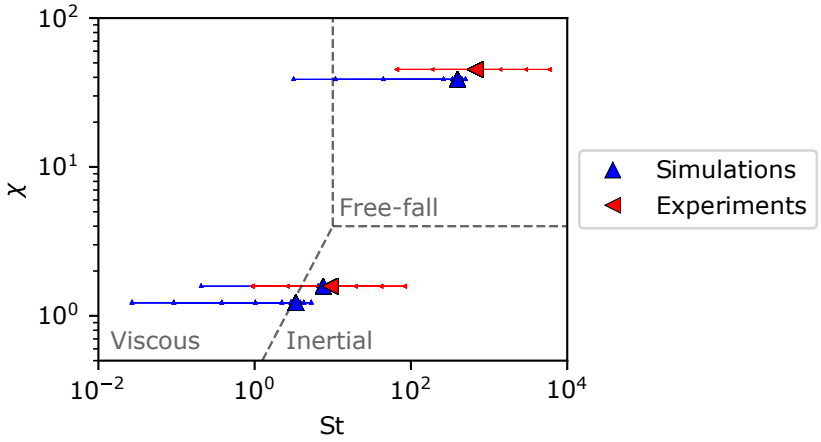

Figure 2.15. Parametric space Stokes number St (Eq. (2.12)) and the density ratio χ (Eq. (2.13)), indicating the regime limits proposed by Courrech du Pont *et al.* [79]. The big markers correspond to the position of the granular columns in the St, χ plane computed with d_{50}. The position St, χ for the small markers was computed with extreme diameters, the maximum $d_{\max}$ and minimum $d_{\min}$, in polydisperse granular column collapses[¶¶].

in the computation of particle-fluid interactions that are not precise, the challenges above mentioned are successfully managed in the simulation campaign, guaranteeing that there is no penetration during the contact solution in the non-smooth DEM and employing a fluid solution that can manage high packing fractions.

Experimental

We study the three-dimensional nature of the granular column collapse in an experimental campaign where we varied the column polydispersity level, aspect ratio and fluid environment. The experiments explore columns consisting of glass beads of different sizes and allow the study of monodisperse and polydisperse systems. We use glass beads for excluding conflicting effects like grain elongation, angularity or rugosity, and allowing us to only focus on the influence that the GSD has on granular flows. Moreover, we register the basal pore pressure beneath the column initial geometry and along the collapse principal direction. We link the evolution of the pore pressure with the sequence of the column collapse, and reveal how these two are influenced by the increase on the polydispersity level. Our study presents experimental evidence on how polydispersity affects the collapse sequence and mobility of dry and immersed granular columns that are in the free-fall and inertial regime, respectively (see Fig. 2.15). The results, discussion and conclusions of the experimental study of granular column collapse are presented in Chapter 6.

Mobility Model

Lastly, we introduce a mobility model that correlates the column runout with the collapse energy that satisfactorily works for different polydispersity levels, and for immersed and dry column collapses. We propose that this simplified model can be used for predicting the mobility of granular columns based on column's collapse energy. For presenting this model, we rely on the results obtained from the numerical simulations and experiments, but also include results

from previous studies. The discussion and conclusions of the mobility model are presented in Chapter 7.

CHAPTER 3

Let it shear: Independence of the shear strength to the size polydispersity

This chapter is based on the paper *Grain size distribution does not affect the residual shear strength of granular materials: An experimental proof* by Oscar Polanía, Miguel Cabrera, Mathieu Renouf, Emilien Azéma, and Nicolas Estrada published on May 12th 2023 in Physical Review E **107**, L052901 [162].

Resume

Granular materials are used in several fields and in a wide variety of processes. An important feature of these materials is the diversity of grain sizes, commonly termed as polydispersity. When granular materials are sheared, they exhibit a predominant small elastic range. Then, the material yields, with or without a peak shear strength depending on the initial density. Finally, the material reaches a stationary state, in which it deforms at a constant shear stress, which can be linked to the residual friction angle φ_{r}. However, the role of polydispersity on the shear strength of granular materials is still a matter of debate. In particular, a series of investigations have proved, using numerical simulations, that φ_{r} is independent of polydispersity. This counter intuitive observation keeps elusive to experimentalists, and specially for some technical communities that use φ_{r} as a design parameter (e.g., the soil mechanics community). The aim of this work is to conduct a set of systematic and controlled experiments in order to confirm if φ_{r} is independent of polydispersity, described in terms of grain size (d), size span (λ), and grain size distribution (λ and ι). In order to do so, we built samples of ceramic beads and then sheared these samples in a triaxial apparatus. We varied polydispersity, building monodisperse, bidisperse, and polydisperse granular samples; this allowed us to study the effects of grain size, size span, and grain size distribution on φ_{r}

3.1 | Methodology

We performed a set of drained (i.e., dry) triaxial tests with spherical ceramic beads of different sizes. Using these grains, we built 18 samples with different GSDs: monodisperse, bidisperse, polydisperse with a uniform distribution by volume fraction , and polydisperse with a Fuller and Thompson distribution. Our samples had size spans $\lambda = d_{\max}/d_{\min} \in [1.0 - 12.7]$ (see

Fig. 3.1). We used this type of grains in order to exclude the effects of angularity, elongation, and contact friction, which allowed us to observe solely the effects of the GSD.

The triaxial test is widely used in soil and rock mechanics. In this test, the cylindrical granular samples are placed inside a flexible membrane, which allows for applying a lateral confining pressure σ_3 that is kept constant throughout the experiment. Then, the samples are compressed axially at a constant rate $\dot{\epsilon}_1$, inducing a vertical stress σ_1. In our experimental campaign, we used samples of height $H = 140$ mm and diameter $D = 70$ mm. The vertical strain ϵ_1 was computed as $\epsilon_1 = \Delta H/H$. An advantage of this test is that the shear band develops naturally inside the sample and not on pre-imposed failure planes. In the triaxial test, although the shear direction is not controlled and the shear stress can not be measured directly, a normalized shear stress q/p can be computed from the mean p and deviatoric q*.

For monodisperse samples, we varied d between 0.35 and 1.9 mm. In bidisperse samples, the mass of each specie was 50% of the total mass. For polydispese samples, we used samples that had from 3 to 6 grain sizes, with which we built two different GSDs: uniform distributions by volume fraction, and Fuller and Thompson distributions (i.e., GSDs with $\iota = 1$ and 0.5, respectively (see Eq. (2.2)). The cumulative volume fraction CVF of the 18 samples used in this work is shown in Fig. 3.1. The use of the linear GSDs was motivated by numerical studies showing the independence of the shear strength of granular materials to the size polydispersity employing these distributions [32, 38] and the motivation behind using the Fuller and Thompson distribution is because it produces the densest and better connected granular configuration [13, 18]. We used ceramic beads with density $\rho = 6.05\ \mathrm{g/cm^3}$ of the type *ZY* produced by Sigmund Lindner GmbH. We acknowledge that many granular systems, specially those involved in geophysical processes [6, 164], might have larger values of λ than the ones we explored, but we consider that the size span used is representative to study the residual resistance of polydisperse granular materials.

Segregation is an intrinsic phenomenon in granular materials that occurs when they have different physical features; size in our case. For testing segregation during the samples' construction, we first did a series of test in a big cylinder of diameter $D^* = 200$ mm and height $H^* = 150$ mm. For these tests, we first placed two empty small cylindrical samplers of diameter $d^* = 60$ mm and height $h^* = 20$ mm at the base of the big cylinder, and then fill the big cylinder in layers of 50 mm with bidisperse mixes of grains in two manners: funneling the mix, and spooning the mix. After filling a layer, we placed two other samplers and repeat the process until reaching H^*. Finally, we recovered the samplers, six after filling the cylinder, and did granulometry test with each. We used bidisperse mixes because they tend to segregate easier than polydisperse. We did these tests with three distributions of bidisperse grains and did three repetitions. Figure 3.2 shows the results of these tests, where each marker corresponds to the average of the granulometry of twelve samplers.

*The notation of p, q presented in Eq. (2.8), (2.5), respectively, correspond to the MIT. In this chapter we will used the alternative notation known as the Cambridge notation with $p = (\sigma'_1 + 2\sigma'_3)/3$, $q = (\sigma_1 - \sigma_3)$ and $\sin\varphi = 3q/(6p - q)$ [163]

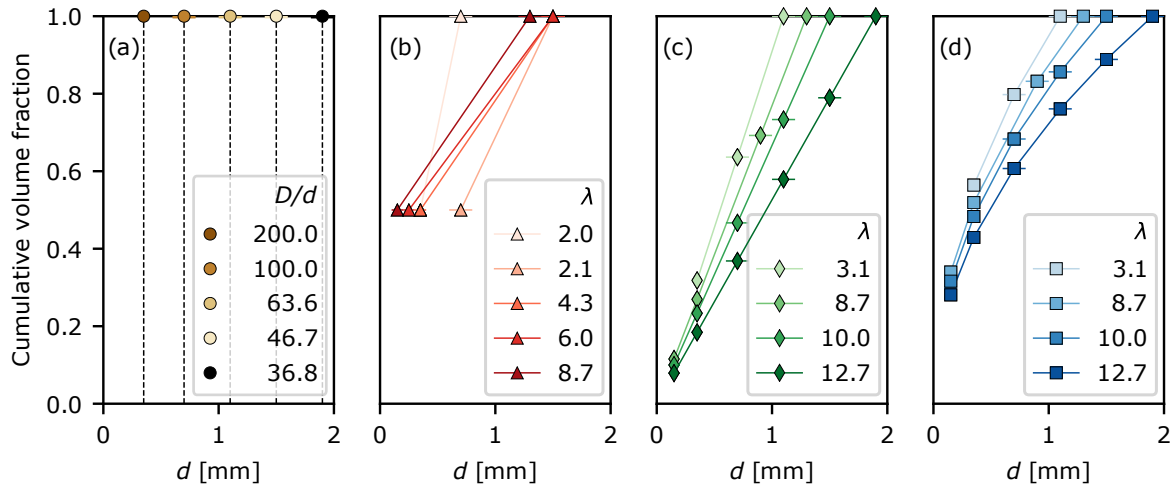

Figure 3.1. Cumulative volume fraction CVF as a function of grain diameter d, for the four types of grain size distributions explored in this work: (a) Monodispese samples; (b) Bidispese samples; (c) polydisperse samples with a uniform distributions by volume fraction following $\mathrm{CVF} = (d/d_{\max})^{1.0}$; and (d) polydisperse samples with a distribution following $\mathrm{CVF} = (d/d_{\max})^{0.5}$. Symbols represent the average and horizontal bars represent the range in size reported by the supplier Sigmund Lindner GmbH. $\lambda = d_{\max}/d_{\min}$ is the size ratio between the maximum $d_{\max}$ and minimum grain diameter $d_{\min}$. For monodisperse samples (a), D/d is the system-to-grain size ratio, with $D = 70$ mm being the sample's diameter.

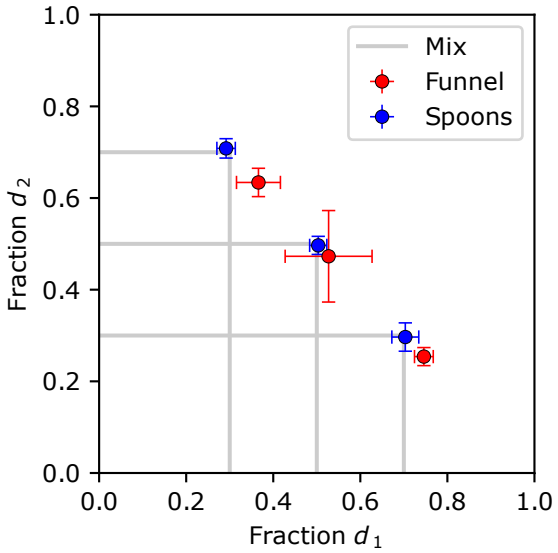

Figure 3.2. Fraction of grains with diameter $d_1 = 0.9$ mm and $d_2 = 1.9$ mm obtained from granulometry. The gray lines indicate the mix fraction of each grain size. The red and blue markers stand for the granulometry done to the samples constructed by funeling and spooning the grains mix, respectively. Error bar show the minimum and maximum value between repetitions.

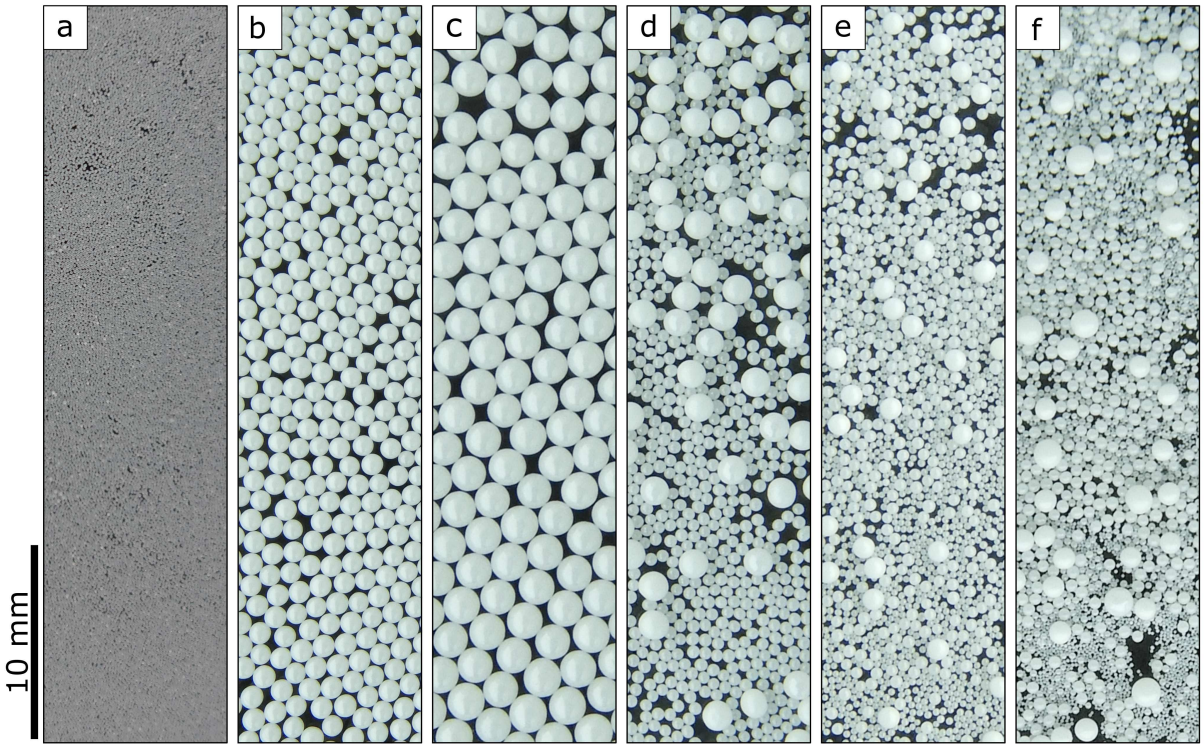

Figure 3.3. Close-up scale views of some of the tested granular systems. (a), (b), and (c): grains with diameters $d = 0.15 \pm 0.05$ mm, $d = 1.1 \pm 0.1$ mm, and $d = 1.9 \pm 0.1$ mm, respectively; (d) bidisperse sample with $\lambda = 2.1$; and (e) and (f) polydisperse samples with $\lambda = 3.1$ and 10, respectively. A 10 mm scale is shown in the figure lower-left corner.

For the construction of the triaxial samples, we found satisfactory to hand-mix the grains in a wide bowl and then gently fill the cylinder of diameter D in three layers, densifying each layer by tamping and shuddering up to a flat surface. The initial packing fraction ϕ_0 rapidly increased with λ, and it reaches a plateau for $\lambda > 4$ at $\phi_0 \approx 0.71$. The maximum ϕ_0 occurred for $\lambda = 12$ and $\iota = 0.5$. Excluding monodisperse systems and bidisperse with $\lambda = 2$, our samples had initial packing fractions that were larger than that of the random close packing ϕ_{rcp} (see Fig. 3.4).

The test inertial level is computed with the inertial number I (see Eq. (2.11)), considering the confinement pressure P_{c} as σ_3, the shear rate $\dot{\gamma}$ as $\dot{\epsilon}_1$, and the characteristic d as either $d_{\max}$ or $d_{\min}$. Tests were conducted at a confinement pressure $\sigma_3 = [100, 200]$ kPa and the vertical strain rate is set to $\dot{\epsilon}_1 = 0.0001/\mathrm{s}$, resulting, in all cases, in quasi-static experiments with $I < 10^{-4}$. Samples were deformed up to $\epsilon_1 = 0.2$ and the residual strength was considered at $\epsilon_1 \in [0.15 - 0.2]$. Finally, we sieved the samples and confirm that no modifications of the GSD (e.g. grain crushing) had occurred at the end of the test. In order to quantify variability, we conducted three repetitions for one GSD of each set (i.e. three repetitions of the monodisperse sample with $d = 1.1$ mm, the bidisperse sample with $\lambda = 6$, the polydisperse sample with $(\lambda, \iota) = (10, 1)$, and the polydisperse sample with $(\lambda, \iota) = (10, 0.5)$).

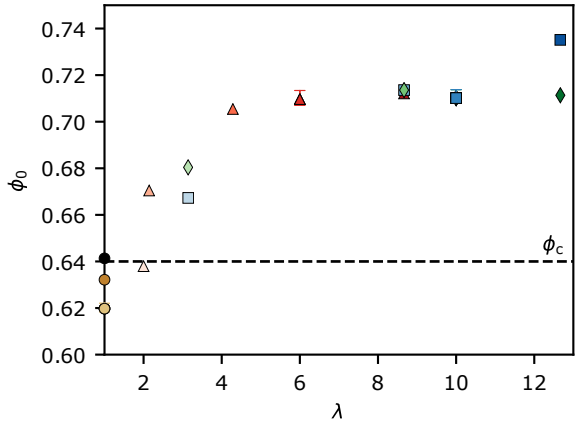

Figure 3.4. Initial packing fraction ϕ_0 as a function of the size span λ. The known limit of the random close packing for monodisperse spheres, $\phi_{\mathrm{rcp}} = 0.64$, is shown by the dashed line [15]. Error bars are the minimum and maximum values between sample repetitions. Monodisperse samples ($\circ$); bidisperse samples ($\triangle$), polydisperse samples with uniform distributions by volume fraction (i.e., with exponent $\iota = 1$) ($\diamond$); and polydisperse samples with Fuller and Thompson distributions (i.e., with exponent $\iota = 0.5$) ($\square$). The symbols' colour match those on Fig. 3.1.

3.2 | Results and discussion

Figure 3.5 shows the evolution of the normalized shear stress q/p for the four GSDs used in this work. For monodisperse systems, we found that the shear strength of samples with $d = 1.9$ mm if affected by grain-size effects (i.e., for a system-to-grain size ratio $D/d < 37$). This holds true for both values of σ_3. For samples with $D/d > 46$, q/p converges to a common value (see Fig. 3.5 (a)). This result shows that, provided that the sample is sufficiently large compared to the grains' size, the shear strength is independent of the grain size, which is in agreement with previous experimental results [54, 165]. After identifying the grain-size effect for samples with $D/d < 37$, we decided to not include grains with $d > 1.9$ mm in bidisperse samples. Interestingly, for all values of the size span λ in bidisperse experiments, q/p also tends to a common value. This result shows that the residual strength is not only independent of grains size, but it is also independent of the size span (see Fig. 3.5 (b)). Polydisperse samples with exponents $\iota = 1$ and 0.5 show, with greater clarity, that q/p is in fact independent of both λ and ι (see Figs. 3.5(c) and (d)). This result confirms experimentally that the residual shear strength is independent of the grain size distribution, being in agreement with previous results obtained by means of DEM simulations [17, 31, 32, 44, 45, 57–59].

Now, let us compare the residual shear strength of all GSDs analysed in this work. Figure 3.6 shows the residual friction angle φ_{r} for all samples as a function of the size span λ and the initial packing fraction ϕ_0. It can be seen that all values collapse around a common value of $\varphi_{\mathrm{r}} \simeq 24°$. Bidisperse samples exhibit higher variability; even though φ_{r} is close to that of monodisperse and polydisperse samples. This result is in disagreement with the one presented in [166], where a strong contrast between bidisperse and polydisperse systems was found. It can also be seen that polydisperese samples with $\iota = 0.5$ have a slightly larger φ_{r} than the rest

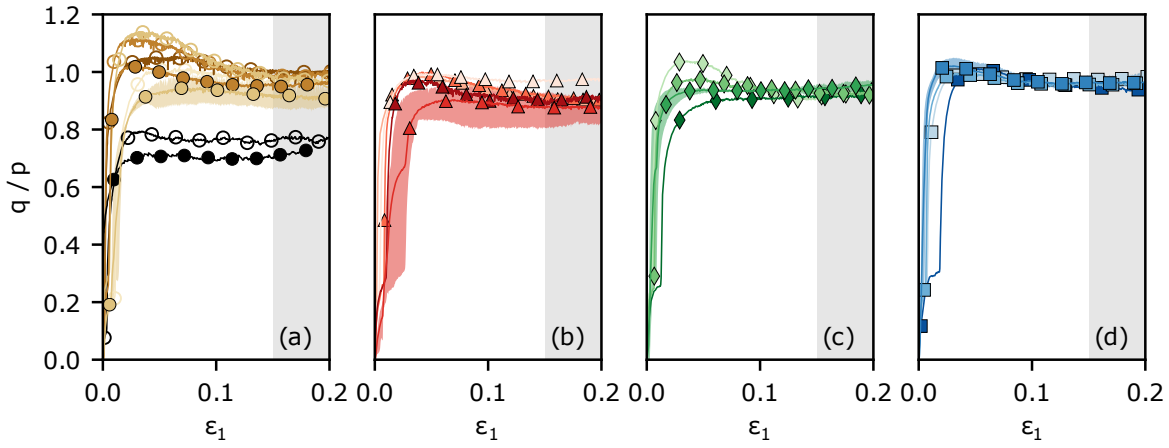

Figure 3.5. Evolution of the normalized shear stress q/p as a function of the vertical strain ϵ_1 for: (a) monodisperse samples; (b) bidisperse samples; (c) polydisperse samples with uniform distributions by volume fraction (i.e., with exponent $\iota = 1$); and (d) polydisperse samples with Fuller and Thompson distributions (i.e., with exponent $\iota = 0.5$). Shaded areas represent the variability between repetitions with envelopes indicating the minimum and maximum values. The gray shaded region between $\epsilon_1 \in [0.15, 0.2]$ is the region where the residual shear strength is computed. In (a), empty (○) and full markers (●) correspond to experiments with confinement pressure $\sigma_3 = 100$ kPa and 200 kPa, respectively. The symbols shape and colour match those on Fig. 3.1.

of GSDs. In order to understand this small difference, one must take into account that these are also the samples with the highest initial density and, that by design, the triaxial test is incapable of fully reaching a steady state. For example, the triaxial tests conducted in this work reach a maximum $\epsilon_1 = 0.2$ before the sample collapse. It is thus probable that the shear strength of these samples is still marginally affected by the sample' initial density.

3.3 | Conclusions

We conducted an experimental campaign of dry triaxial tests, varying the grains' size, size span, and size distribution of samples composed of ceramic beads. Our experiments allowed us to study the effects that these three features have on the residual shear strength of granular materials, since all samples were built with spherical grains, with the same contact friction coefficient, and at a level of confinement that was low enough in order to prevent crushing. Our results confirm that the residual shear strength of granular materials is indeed independent of the grain size, of the level of polydispersity, and of the CVF shape, as it has been shown numerically [17, 31, 32, 44, 45, 57–59] and as it has been suggested in previous experimental works [55, 56].

The experimental results presented in this work are important because they fairly close the gap of knowledge between experiments and simulations of quasi-static polydisperse systems, confirming that the shear strength of granular materials is independent of the grain size distribution. They also work as a link, connecting results coming from the granular physics and the soil mechanics communities, and directing the discussion of the residual strength towards

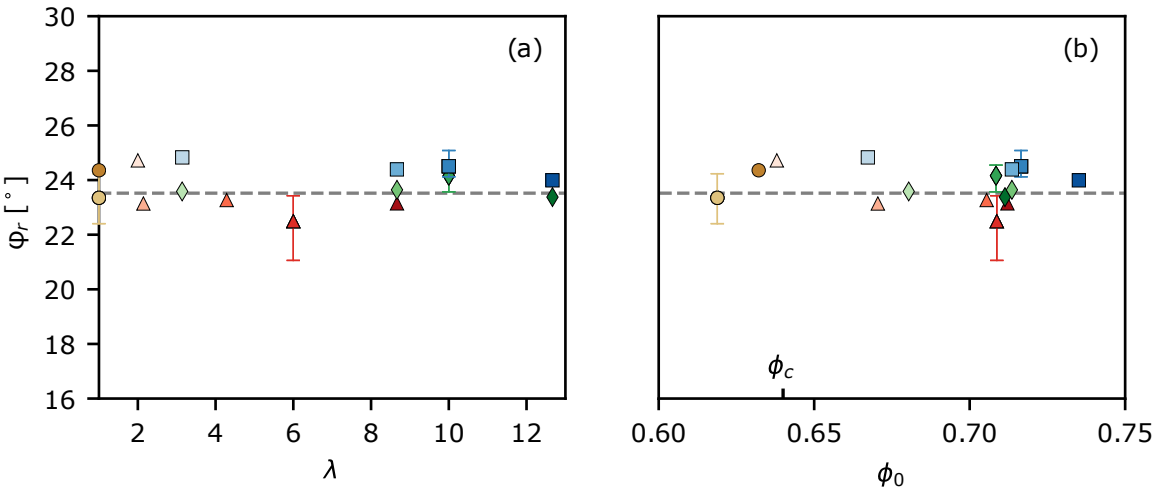

Figure 3.6. Residual friction angle φ_{r} as a function of the (a) size span λ and (b) the initial packing fraction ϕ_0. The friction angle φ_{r} was computed as $\sin\varphi = 3q/(6p - q)$. The dashed line shows the mean value for all experiments. Vertical bars indicate the maximum and minimum values between repetitions. Monodisperse samples (○); bidisperse samples (△), polydisperse samples with uniform distributions by volume fraction (i.e., with exponent $\iota = 1$) (◇); and polydisperse samples with Fuller and Thompson distributions (i.e., with exponent $\iota = 0.5$) (□). The symbols' colour match those on Fig. 3.1.

a common conclusion. The results of this work contribute to the knowledge of polydisperse granular materials behaviour that is a matter of interest in natural and industrial processes. Further studies focusing on resistance of granular materials might look into other details, such as the link between packing fraction and peak shear strength, or the role of grain shape on the shear response. Contributions of this kind would enrich the understanding of polydisperse granular materials.

CHAPTER 4

Inertial Effect On Polydisperse Granular Flows

The results presented in this chapter were obtained from simulations conducted in the final phase of the PhD. We believe that these simulations add significant value to our study as they bridge observations from flows in the quasi-static regime to transitional flows, which are later discussed in this thesis. Although some of the simulations did not finish, the general trend of the results provides rich information that allowed us to discuss and draw conclusions about the influence of polydispersity on highly inertial granular flows.

Resume

The flow behavior of granular materials undergoes various behaviours that depend on the system's deformation rate and stress state. Granular materials are generally studied in the quasi-static regime, where the grains interact through long-lasting contacts. However, granular flows can also occur under highly agitated conditions, where grains interact through collisions and contacts of short duration. In this latter scenario, granular materials, particularly polydisperse ones, have not been extensively studied. In this research, we conduct numerical simulations using Discrete Element Methods to study polydisperse granular flows in systems spanning orders of magnitude in their inertial levels. The objectives of this study are to evaluate the macro behaviour of polydisperse granular materials as the system's inertia increases and to gain insights into the contacts between grains in polydisperse systems.

4.1 | Methodology

The simulations conducted for this study were carried out using Discrete Element Method (DEM) of the type Non-Smooth Contact Dynamic (NSCD) [109, 110]. The NSCD relates the impulse of each contact with the changes of the relative velocity during a time step dt. In this method, no elastic repulsion resulting from grain interpenetration or smoothing of the friction laws is necessary. We consider NSCD to be a suitable approach for studying polydisperse granular flows because it allows to obtain the motion of grains from the contact impulse, and not from the elastic repulsion, which could lead to situation difficult to manage due to the large size difference between grains in polydisperse systems. Simulations were done with the open source sofware LMGC90 developed in LMGC, Université de Montpellier [167].
The granular flows of primary interest to us generally undergo volumetric changes, resulting in both contractions and expansions that represent variations in the packing fraction ϕ. We study

granular flows in the shear cell configuration that allows volumetric changes. The shear cell geometry that we model has a length $L_x = 15d_{50}$ and width $W_y = 8d_{50}$ with $d_{50} = 1.0$ mm, and periodic boundaries in the planes XZ and YZ. In the planes XY, clusters made with grains of diameter d_{50}* ensure the shear of the sample. The bulk grains of the shear cell were initially placed by gravity in a box of dimensions L_x, W_y and $H = 17.25d_{50}$ and then they were compressed by the top and bottom clusters with force $F_Z = -22.5$ N and $F_z = 22.5$ N, respectively, applying a confinement pressure $P_c = F_z/(L_x W_y)$. The compression process, for which the grains' friction coefficient was set to 0, finished when the grains' contact network was stable, resulting in a shear cell with height $H_z \approx 16d_{50}$.

In Chapter 3, we experimentally showed that the shear strengh of granular materials is independent of the polydispersity level and the shape of the Grain Size Distribution (GSD) in systems with low inertial number I in the quasi-static regime (see Fig. 3.4). Therefore, in this chapter, we decided to use linear GSDs (i.e. Eq. 2.2 with $\iota = 1.0$). This kind of GSD, well known and used in the granular materials community, produces dense and well connected granular arrangements [168, 169]. Moreover, a linear GSD allow to make a fair comparison between grain's families (sizes) because the volume and mass of each size is the same†. We use four polydispersity levels $\lambda = d_{\max}/d_{\min} = [1.2, 4, 6, 8]$ in GSDs that share a common Cumulative Volume Fraction of 0.5 for d_{50}. All GSDs have ten grains' diameter, each one having 10% of the bulk volume and mass, linearly distributed between $d_{\min} = 2d_{50}/(\lambda+1)$ and $d_{\max} = \lambda d_{\min}$. The dimensions of the shear cell were kept constant for having simulations with nearly the same initial volume, but having different grains numbers $n(\lambda) \in [2{,}056 - 31{,}545]$ and obtaining initial packing fractions $\phi_0(\lambda) = [0.60, 0.673, 0.71, 0.78]$ after the compression. Grains were considered as rigid spheres with restitution coefficient 0, friction coefficient 0.4.

In addition to varying the sample's polydispersity, we adjusted the level of inertia in the shear cell to have samples with different inertial numbers. In order to do so, the top and bottom clusters displace with an imposed constant horizontal velocity V_x and $-V_x$, respectively, resulting in a linear and nearly steady shear rate $\dot{\gamma} = 2V_x/H_i$ with H_i being the sample's height at a given instant. The magnitude of V_x was computed as a function of the inertial number $I \in [1\text{x}10^{-4} - 5\text{x}10^{-1}]$‡ that we aimed to achieved and the initial sample height H_Z as

$$V_x = I\frac{H_z/2}{d_{50}}\sqrt{\frac{P_c}{\rho_s}}, \tag{4.1}$$

*Some grains might manage to break through the voids of the rough walls and move indefinitely in the $\pm Z$ axis. To avoid this issue, we added over the upper cluster and down the bottom cluster a plane wall that stops grains (see blue bodies in Fig. 4.1)

†There is a last, but definitively not least, reason for choosing linear GSDs. Reducing ι in Eq. 2.2 would lead to denser and better connected system; however, reducing the exponent would significantly increase the number of small particles, the number of active contacts, and the computation time. Therefore, for a pragmatic reason and knowing that the shear strength is independent of the GSD (see Chapter 3), we have used linear GSDs.

‡This group of inertial numbers was used to compute the velocity at which the system is being deformed and consider the initial sample height as the flow height; however, during the flow the height will change and so will the inertial number.

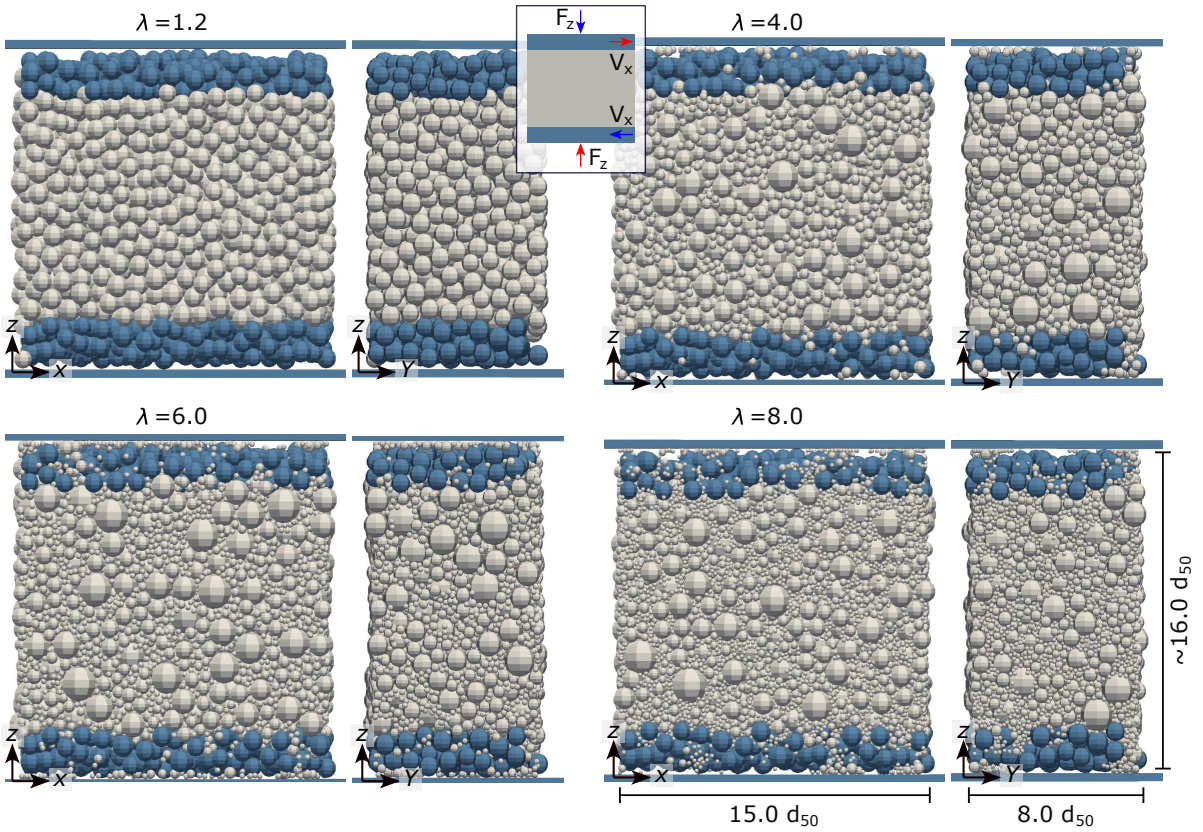

Figure 4.1. Lateral views of the shear cell configuration in the XZ and YZ planes for all the polydispersity levels $\lambda \in [1.2 - 8.0]$. The blue bodies represent the cluster where the boundary conditions are applied. The dimensions showed in the right bottom corner are the initial dimensions of the shear cell and apply for all samples. The inset between $\lambda = 1.2$ and 4.0 presents a sketch indicating the forces and velocities applied to the upper and lower clusters.

with the grains' density $\rho_s = 2500\ \mathrm{kg/m^3}$. The cluster boundaries have displacement restrain in the Y direction and rotations restrains in XY, XZ and YZ, and can freely move in Z, allowing volume changes. The inertial numbers I that we wanted to achieve allowed us to study granular flows from the quasi-static to dense regime. Fig. 4.1 presents the lateral view of the shear cell for all polydispersity levels λ and shows an sketch indicating the direction of the velocities and forces applied to the boundaries.

The variation of the inertial number in the simulations was made in a sequential form. The numerical campaign stared with the simulations of systems with the lowest inertial number (i.e., $I = 10^{-4}$). The output results of the step where the systems reached the loosest state and began to contract was used as input, using the contact network and grains' position, for the simulations with the subsequent inertial number (i.e., $I = 10^{-3}$). Launching the simulations in this sequential form prevents a strong reaction between the cluster and the grains, especially at high inertial numbers, and allows the systems to reach a stable state more quickly. Last, we found satisfactory to use as time step dt the minimum between $dt = 0.01 d_{50}/V_x$ and $dt = 0.1 d_{50}/\sqrt{P_c/\rho_s}$, having simulations marginally affected by grain interpenetration gapC with a maximum $\mathrm{gapC}/d = 2\mathrm{x}10^{-14}$.

4.2 | Results and Discussion

The results presented are divided in three subsections each one with an specific goal. Firstly, we present and discuss the results at a macroscopic scale with focus on the volume variation and the macroscopic shear strength. Secondly, we show the influence that polydispersity and inertial number have on the system's connectivity. Then, dig into the contact scale and make a evaluation of how the contact branch length and normal force evolve with I and λ Lastly, we discuss about the fabric and forces anisotropies, and evaluate how they vary with both I and λ, and how they influence the shear strengh of polydisperse materials.

4.2.1 Macroscopic Behaviour

The packing fraction, computed for the entire system, varies due to the dilatancy and/or compaction of the sample. Samples with inertial numbers $I \lesssim 10^{-1}$ have a nearly constant ϕ during the simulation. On the contrary, the evolution of the packing fraction ϕ of samples with $I > 10^{-1}$ develops in a wave-like appearance, although they have already reached an steady state. Fig. 4.2 (a) show the evolution of ϕ for all samples and compares the effect that I has on systems with the same polydispersity level λ.

The stress tensor $\boldsymbol{\sigma}$ of the systems was computed as the sum of the product between the vector force $\boldsymbol{f}$ and length branch vector $\boldsymbol{l_b}$[§] for all the grains in contact within the volume $V = L_x W_y H_z$[¶] (see Eq. (2.7)). We computed $\boldsymbol{\sigma}$ with all the output files from the simulations and, from the stress tensor $\boldsymbol{\sigma}$, we obtained the principal stresses σ_1 and σ_3 as the maximum and minimum eigenvalues of the stress tensor, respectively. Then, we computed the mean p and deviatoric stress q (see Eq. (2.8) and (2.5)), and obtained the effective friction coefficient $\mu = q/p$. Fig. 4.2 (b) show the evolution of μ for all samples and compares the effect that I has on systems with the same polydispersity level λ. Although the friction coefficient at high inertial numbers evolves with much more dispersion compared to the packing fraction ϕ, its global evolution is closely linked with the evolution of ϕ. When ϕ is at a minimum, μ tends to be at a maximum, and vice versa (see the bottom row in Fig. 4.2).

We can look at the average effective friction coefficient μ and packing fraction ϕ as a function of the inertial number I because the simulations are shear cells with impose pressure that allow volume changes (see Fig. 4.3). Three main things can be highlighted from these results.

The first one is related to $\phi(I)$. The packing fraction decreases linearly with I [170], with a shift for each polydispersity sample that depends on its maximum packing fraction. In this case, we assume the maximum to be equal to the initial ϕ_0 because it was obtained by setting the friction coefficient between grains as zero. We found that normalising ϕ by ϕ_0, trends

[§]We computed the length branch vector $l_b = ((d_1 + d_2)/2 - \mathrm{gapC})\boldsymbol{n}$ with $\boldsymbol{n}$ being the normal vector, d_1 and d_2 being the diameters of the two grains in contact, and gapC being the grains' interpenetration. However, l_b could be simply obtained as the difference between the grains position, but while processing the data one must be aware of the periodic boundaries.

[¶]For computing $\boldsymbol{\sigma}$, the contacts between the cluster-walls and free-grains were not considered.

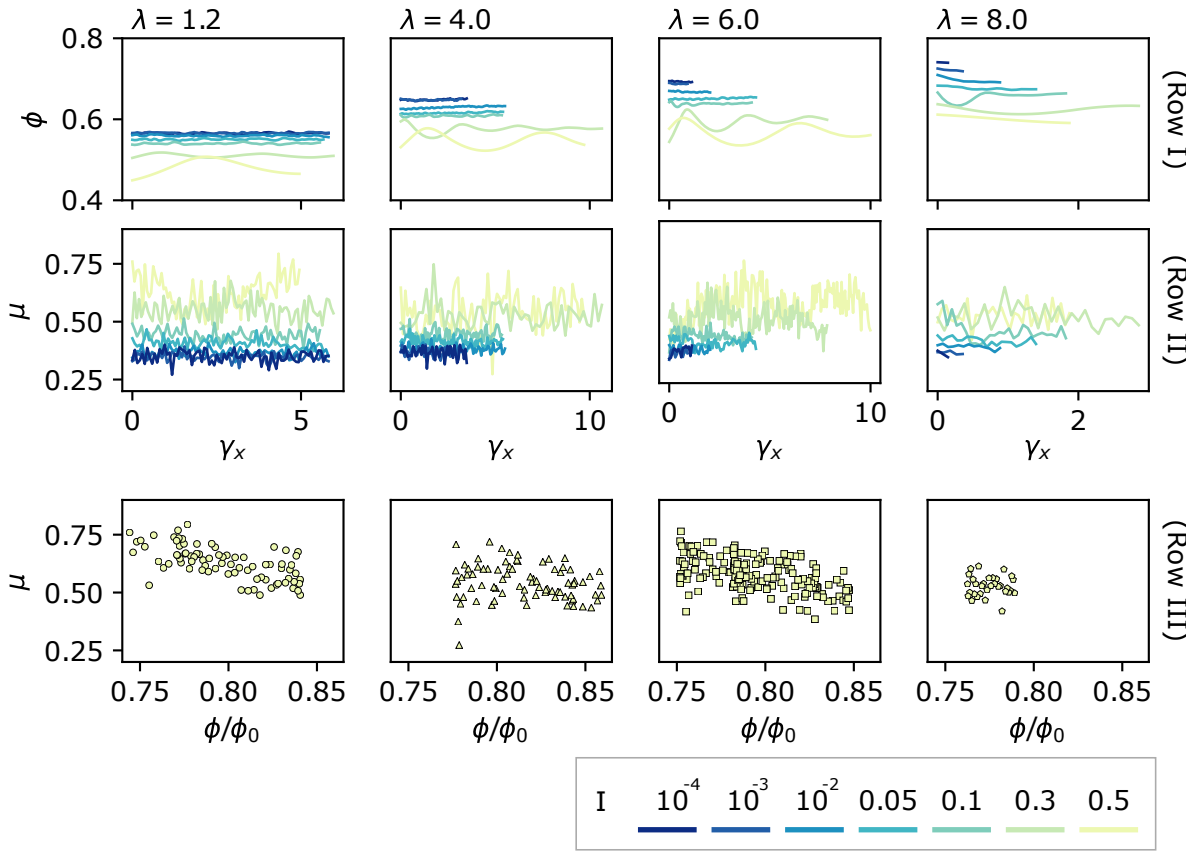

Figure 4.2. Evolution of (Row I) the packing fraction ϕ and (Row II) the effective friction coefficient μ as a function of the sample deformation $\gamma_x = \Delta X/H_z$, comparing the effect that the inertial number has on samples with the same polydispersity level λ (Columns). (Row III) ϕ vs μ for samples with $I \approx 0.5$.

collapse on a master curve defined by:

$$\frac{\phi(I)}{\phi_0(\lambda)} = 0.95 - 0.38I \tag{4.2}$$

that satisfactorily works for $\lambda \in [1.2, 4.0, 6.0]$ and deviates for largest $\lambda = 8.0$. This law is limited to quasi-static and dense flows because large inertial numbers ($I \gg 1$) would result in negative values (see Fig. 4.3 (a)).

The second important thing to be highlighted from the results presented in Fig. 4.3 is $\mu(I)$. The effective friction coefficient increases with the inertial number and, remarkably, all samples, regardless of their polydispersity level, collapse on a trend that follows the friction law proposed by Jop *et al.* [62] as:

$$\mu(I) = \mu_s + \frac{\mu_2 + \mu_s}{I_0/I + 1}, \tag{4.3}$$

with μ_s being a critical value at zero shear rate that converges to a limit μ_2 at high inertial numbers, and I_0 is a constant. Moreover, for samples with $I \lesssim 0.1$, the effective friction coefficient μ is similar for systems with different λ. This result newly evidences that μ is independent of the polydispersity level, at least up to an inertial number $I \sim 0.1$, and extends the conclusion of Chapter 3 to granular flows in the dense regime. For systems with higher inertial number $I > 0.1$, the effective coefficient of monodisperse and polydisperse samples starts to differ, being μ consistently larger for monodisperse samples.

The last observation to be made about the macroscopic behavior concerns the diameter d used to characterize polydisperse granular materials to compute the inertial number I. This characteristic length is difficult to interpret and its choice might depends on subjective, but well founded, interpretations. The discussion that we did about $\mu(I)$ and $\phi(I)$ was based on results obtained with the I computed using d_{50} [59]. The inertial number I computed with $d_{50} = 1$ mm as characteristic length provided a satisfactory evolution of the friction and volume laws for all polydisperisty levels in the range $I \in [10^{-4} - 10^{-1}]$. Therefore, for this range, we would suggest using d_{50} as characteristic length over other averaged diameters, such as the main diameter [76], Sauter mean [75] or the cubic mean [77]. For larger inertial numbers, where grains interact though collisions and the flow transits to a gas-like regime, the choice of the characteristic length might be based on changes of the force network, but the study of that regime is out of the scope of this current study. It also important to be mentioned that our observations are limited to systems without gravity, where segregation is not prone to occur. Further research like the one made by Rognon *et al.* [76] in segregated samples with bidisperse grains could be extended to polydisperse systems.

4.2.2 Connectivity

The coordination number Z, or number of active contacts that grains have, is also a representative quantity of the macroscopic behaviour. The average coordination number provides information about the system's connectivity. Fig. 4.4 presents the coordination number Z and the proportion of floating grains $P(Z_0)$ as a function of the inertial number for all the

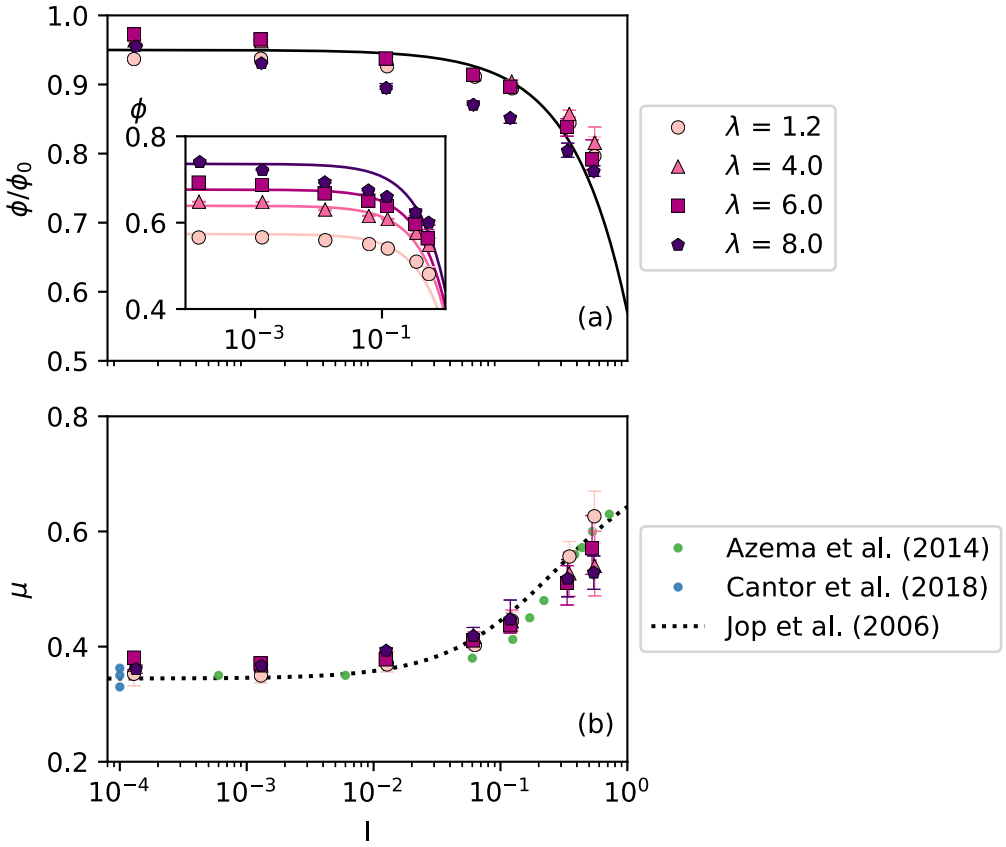

Figure 4.3. (a) Packing fraction ϕ and (b) effective friction coefficient μ in the residual state as a function of the inertial number I (see Eq. (2.11)) and for all the polydispersity levels λ. The markers represent the median value, and the vertical and horizontal error bars stand for the first and third quartile during the residual state. Horizontal error bars might be smaller than the markers. In (a), the lines follow the trend of Eq. (4.2), and the inset presents ϕ and the main figure presents ϕ normalised by the sample's initial packing fraction ϕ_0. In (b), there are included the results of Cantor *et al.* [32] and Azéma & Radjaı [69], and the constitutive law $\mu(I)$ proposed by Jop *et al.* [62] of Eq. (4.3) with $\mu_s = 0.34$, $\mu_2 = 0.73$ and $I_0 = 0.28$. The inertial number I was computed with $d_{50} = 1$ mm as the characteristic grain diameter d.

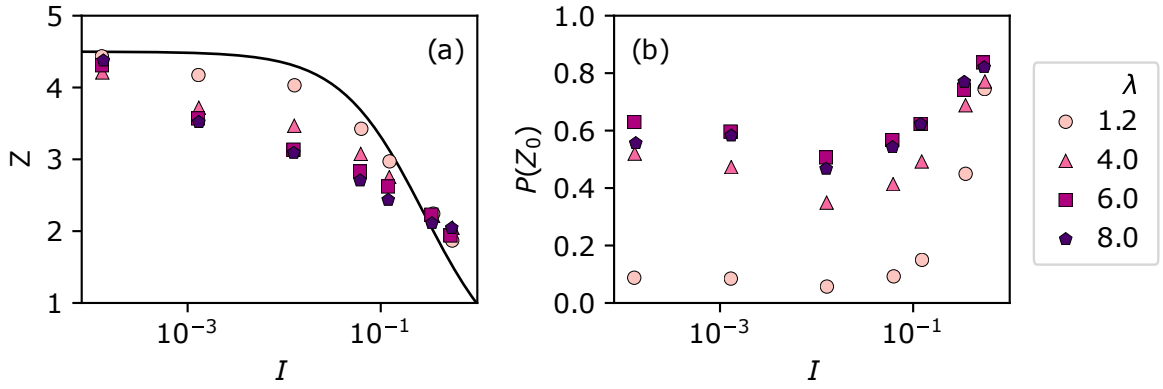

Figure 4.4. (a) Average coordination number Z and (b) proportion of floating grains (i.e., grains with no contacts) as a function of the inertial number I for all polydispersity levels λ. In (a), the continuous line follows an inverse proportion $Z(I) = Z_c/(I/I_0 + 1)$ with $Z_c = 4.5$ and $I_0 = 0.28$. The legend of Fig. 4.3 (a) applies to this figure.

simulations. At very low I, the system is expected to have the largest Z, and at high I, the sample lose contacts, indicating a transition to a fluid-like regime [35]. We computed the averaged coordination number as $Z = 2N_c/n(1 - P_c(Z_0))$ where N_c is the number of active contacts and $P_c(Z_0)$ is the proportion of floating grains (i.e., grains with no contacts). Our results show, as expected, that Z decreases with increasing I. For low values of I, we obtained an average coordination number of $Z \approx 4.2$, which drops to around $Z \approx 1.9$ for high I. Although Z seems to depends on λ, showing that monodisperse system have a larger Z than polydisperse, the general decreasing trend is consistent across all values of λ and systems with different polydispersity tend to converge for $I > 0.1$. The proportion of floating grains Z_0 strongly depends on the polydispersity level. In general, monodisperse systems have the lowest proportion of floating grains, but $P(Z_0)$ rockets for $I > 0.1$ reaching values that are similar for all λ. At large I, the fact of having a similar proportion of floating grains ($P(Z_0) \sim 0.8$) might explains that Z converges for all polydispersity levels.

Lets now discussed the effect that I and λ have at the contact scale focusing on the coordination number of each grain size. Fig. 4.5 presents the average Z for each grain diameter d for all λ. The coordination number, when evaluated for each grain size, reveals that large grains have more active contacts than small ones, implying that they are important nodes for transferring forces in the contact network [31, 32]. As polydispersity increases, the coordination of large grains also increases, while, contrarily, the coordination of small grains decreases. An increase of I leads to a loss of contacts for grains of all sizes and it is interesting to see that in polydisperse samples the average Z per grain size fall to values below one, suggesting that for high inertial numbers force chains are mainly held by large grains. Fig. 4.5 also presents the proportion of grains with a certain coordination number $P_c(Z_n)$, evidencing that grains with large Z have a low probability that quickly drops with an increase of the inertial number.

4.2.3 Normal Forces and Branches

In this section we link the contact normal forces with the contact branch length and look at the influence that the inertial number and the polydispersity have on these two. Fig. 4.6

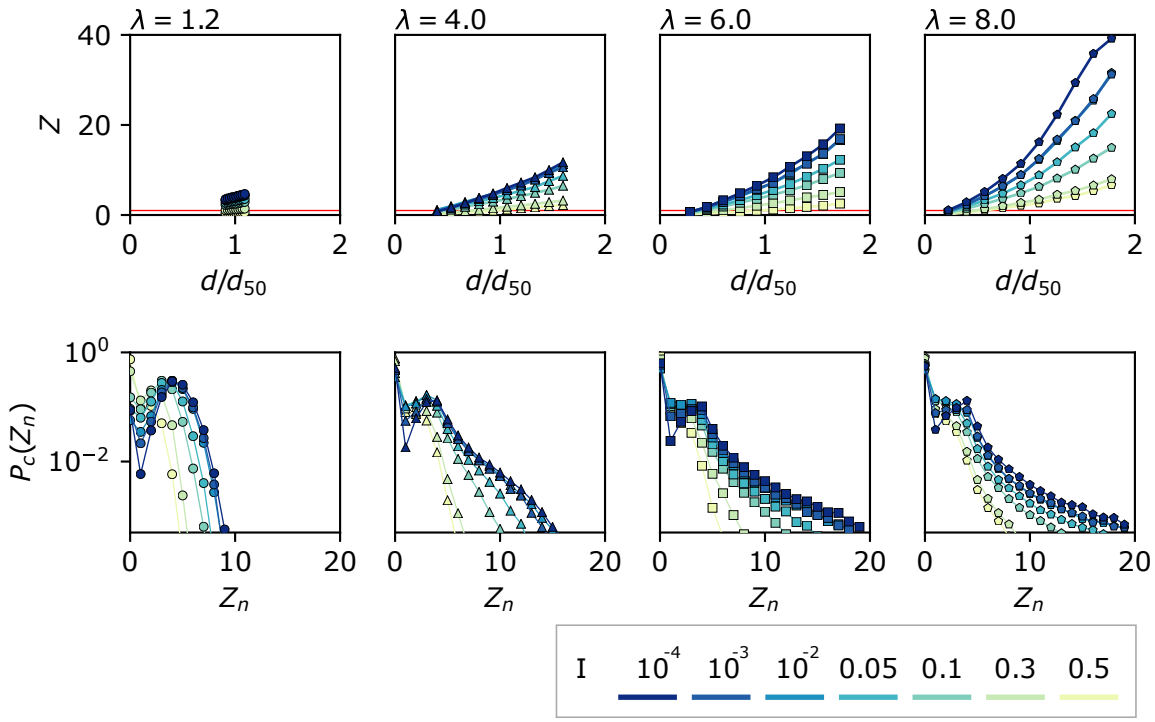

Figure 4.5. (Row I) Average coordination number Z for each grain size class. In this figure, Z is an averaged value for all grains with same diameter without excluding floating grains. The red horizontal line indicates $Z = 1$. (Row II) Probability of a grain with coordination number Z_{n}. Columns present different polydispersity levels λ.

presents a heatmap of the average normal force between two grains of diameter d_i and d_j. Both, the normal force and the grains' diameter, are presented in a reduced form to have a common domain $D = [0 - 1]$. The diameter is presented as $d^* = (d - d_{\min})/(d_{\max} - d_{\min})$ and the normal force is normalised as $f_n^* = (\overline{f}_n - \overline{f}_n^{\min})/(\overline{f}_n^{\max} - \overline{f}_n^{\min})$. In general, the normal force magnitude augments with the size of the grains in contact. Consequently, the minimum and maximum force magnitude tend to occur for the contacts between the smallest and largest grains, respectively. At low inertial numbers, there is an clear transition from the lowest normal force magnitude, occurring at the contact of $d_{\min}$ vs $d_{\min}$, to the largest normal force magnitude, occurring at the contact of $d_{\max}$ vs $d_{\max}$. As the system's inertia increases, the transition from the lowest to the largest f_n becomes disorganised, indicating the erratic characteristic of flows when they interact through collisions and rapid contacts at large inertial numbers. Despite the system's disorder, in all cases, the larger grains concentrate the larger normal forces, suggesting, newly, that force chains are principally held by large grains.

In all cases, the magnitude of the average normal force $\overline{f}_n$ increases with the inertial number and it is always largest for monodisperse systems. In polydisperse systems, the abundance of small grains, with small normal forces, makes that $\overline{f}_n$ decreases (see Fig. 4.7 (a)). As discussed in section 2.2.1, the contact forces could be classified as *weak* $f_n < \overline{f}_n$ or *strong* $f_n > \overline{f}_n$. The Probability Density Function (PDF) of contact forces show that the weak forces are the majority and that their proportion decreases in power law. Contrary, strong forces are the minority and their proportion decays exponentially. In polydisperse materials, weak and

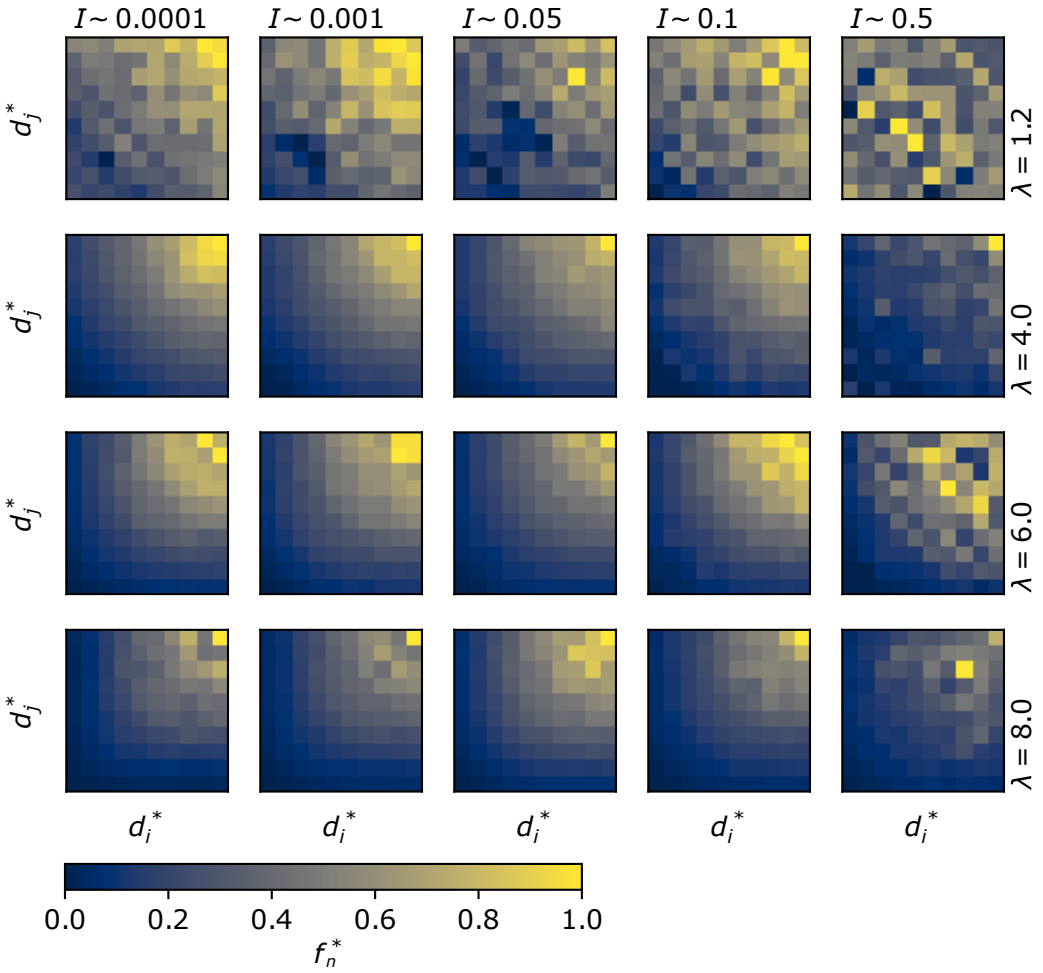

Figure 4.6. Heatmap of the average normal force magnitude $\overline{f}_n$ between two grains of diameter d_i and d_j in contact. Rows present the sample's polydispersity level λ and columns the sample's inertial number I. In this figure, the diameter and the normal force are presented in a reduced form with domain $D = [0 - 1]$. The grain's diameter is presented in the form $d^* = (d - d_{\min})/(d_{\max} - d_{\min})$ and the normal force is presented as $f_n^* = (\overline{f}_n - \overline{f}_n^{\min})/(\overline{f}_n^{\max} - \overline{f}_n^{\min})$ with $\overline{f}_n^{\min}$ and $\overline{f}_n^{\max}$ being the minimum and maximum average normal force between two grains, respectively.

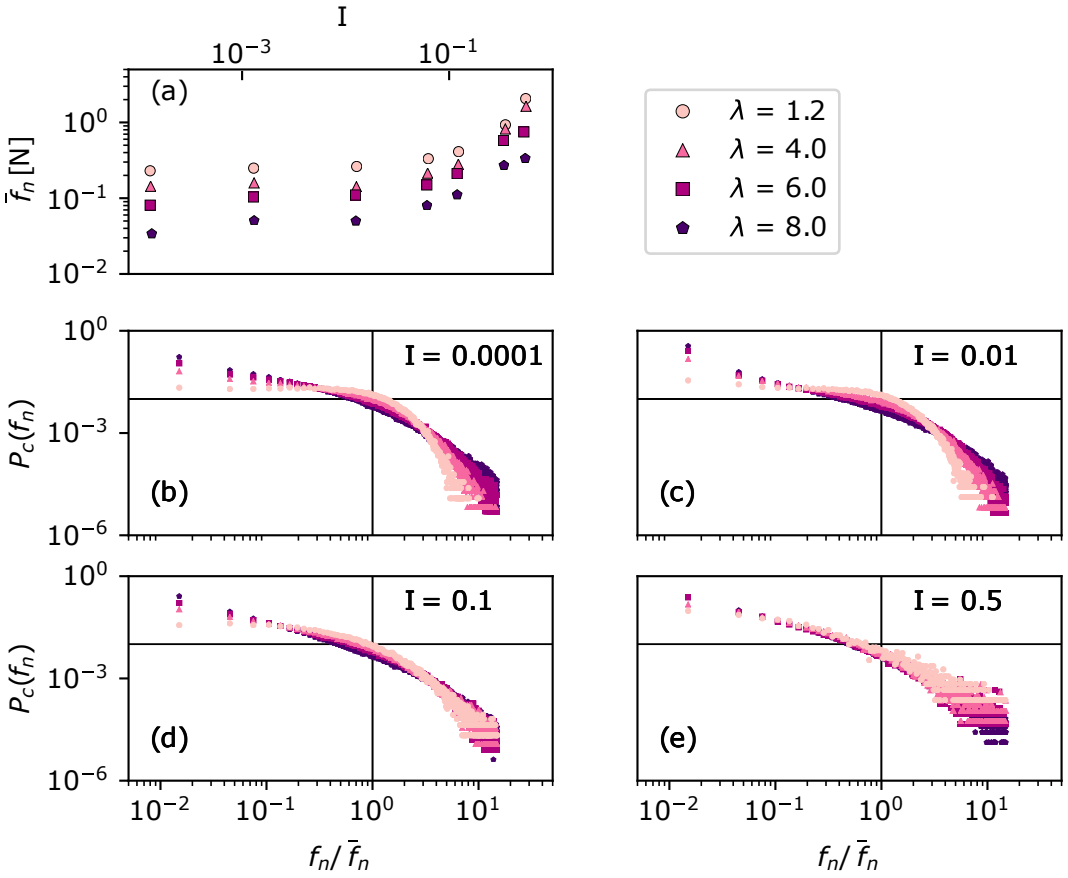

Figure 4.7. (a) Average normal force magnitude $\overline{f}_n$ as a function of the inertial number I. (b - e) Probability density functions PDF of the normal forces f_n normalised by the average $\overline{f}_n$, comparing the effect that λ has on samples with same I. The vertical line divides *weak* $f_n/\overline{f}_n < 1$ and *strong* forces $f_n/\overline{f}_n > 1$.

strong forces still decrease following a power law and an exponential function, respectively; however, they distinguish from monodisperse materials because the force's PDF is widen by extremely small and large forces [31, 32]. Our results are in agreement with previous ones and they show how the force's PDF widen with polydispersity for systems with low inertial numbers ($I \lesssim 10^{-}2$). While the system's inertia increases, the PDF of the normal forces f_n tends to an homogeneous distribution regardless of λ. This homogenisation could be interpreted as forces that are being transmitted through rapid collisions, instead of a transmission through an stable and well established force network. An important observation of the tail of strong forces for systems with $I > 0.1$ is that their proportion decays with random variations, indicating the disorder of the system's force transmission (see Fig. 4.7 (b-e)).

Previous observations can be summarised as followed: the normal force between two grains increases with the grains' size, and the increase of the inertial number disorganise the system. As a function of contact length branch l_b, the contact normal force f_n increases, this is true for all polydispersity levels λ and for all inertial numbers I (see Fig. 4.8 (Row I)). We observe that weak and strong forces coincide with, what we can be call, *short* $l_b/\bar{l}_b < 1$ and *long* branches $l_b/\bar{l}_b > 1$. We confirm that f_b increases proportional to $l_b/\bar{l}_b$, following a power

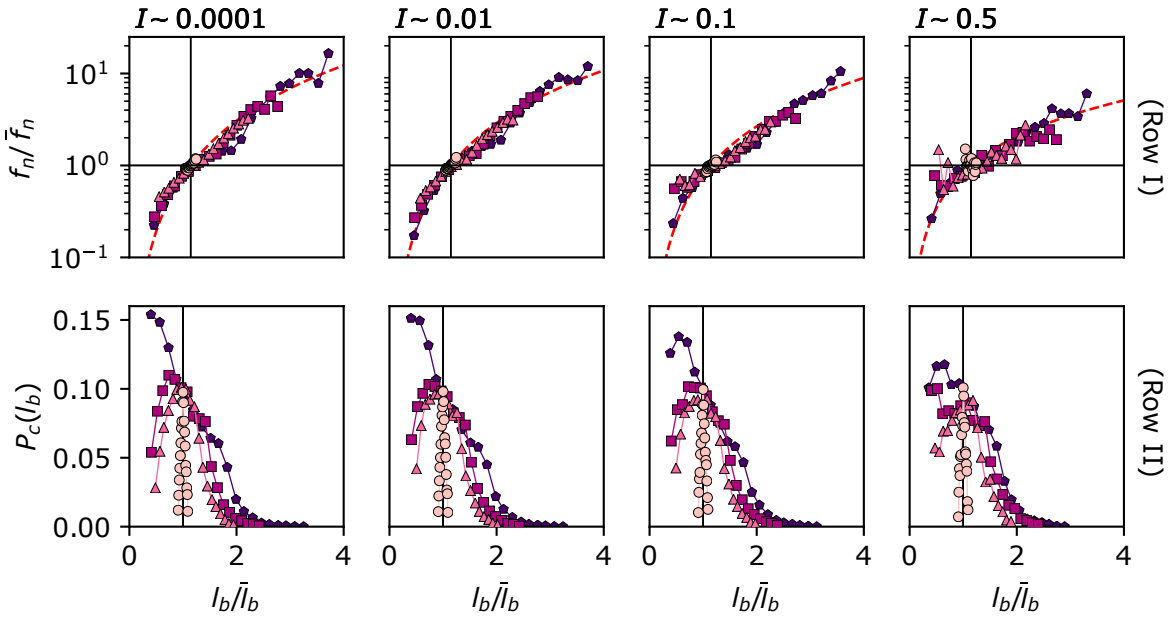

Figure 4.8. (Row I) Normal force magnitude f_n normalised by the overall mean $\overline{f}_n$ as a function of the contact length branch l_b normalised by the average length branch $\bar{l}_b$. The dashed red lines represent a power law in the form $f_n/\overline{f}_n \propto (l_b/\bar{l}_b)^{\alpha}$ with the power index $\alpha = [2.0, 1.9, 1.75, 1.3]$ for $I = [10^{-4}, 10^{-2}, 0.1, 0.5]$, respectively. The horizontal line divides weak and strong forces. (Row II) Probability distribution function of a contact having a branch length l_b/d_{50}. In both rows it is compared the effect of λ in different I (columns). The legend of Fig. 4.7 applies to this figure.

law function that satisfies all polydispersity levels as it was proposed by Cantor *et al.* [32] for $I \sim 10^{-4}$. We noticed that the proportionality $f_b \propto (l_b/\bar{l}_b)^{\alpha}$ remains true for systems with higher inertial numbers $I > 10^{-4}$, but with a consistent decline of the power index α with I. For instance, α varies from 2.0 to 1.3 for $I = 10^{-4}$ and 0.5, respectively. The decrease of the power index α represents that the normal force gap between extreme length branches decreases, augmenting the number of contacts with normal force near the global average $\overline{f}_n$. Although for $I \gtrsim 0.1$ the normal force has a noisy growth with l_b, it still follows the power law that constitute a good prediction of the force between the grains in contact.

The branch lengths vary between $l_b = (d_{\min} + d_{\min})/2$ and $(d_{\max} + d_{\max})/2$. For a nearly monodisperse distribution ($\lambda = 1.2$) the largest proportion of contacts have $l_b = d_{50}$. While for polydisperse distributions, the branch length with the peak proportion consistently reduces with λ. The increase of the inertial number I notably changes the distribution of branch lengths in polydisperse systems. The peak proportion, attributed to short branch lengths, decreases, meaning that less small grains are actively in contact. The latter is aligned with the result presented in Fig. 4.5 which showed that, in average, small grains tends to have less than one contact. Additionally, the diminishing of the proportion of short branch length implies that larger length branches becomes more significant in the force network (see Fig. 4.8 (Row II)).

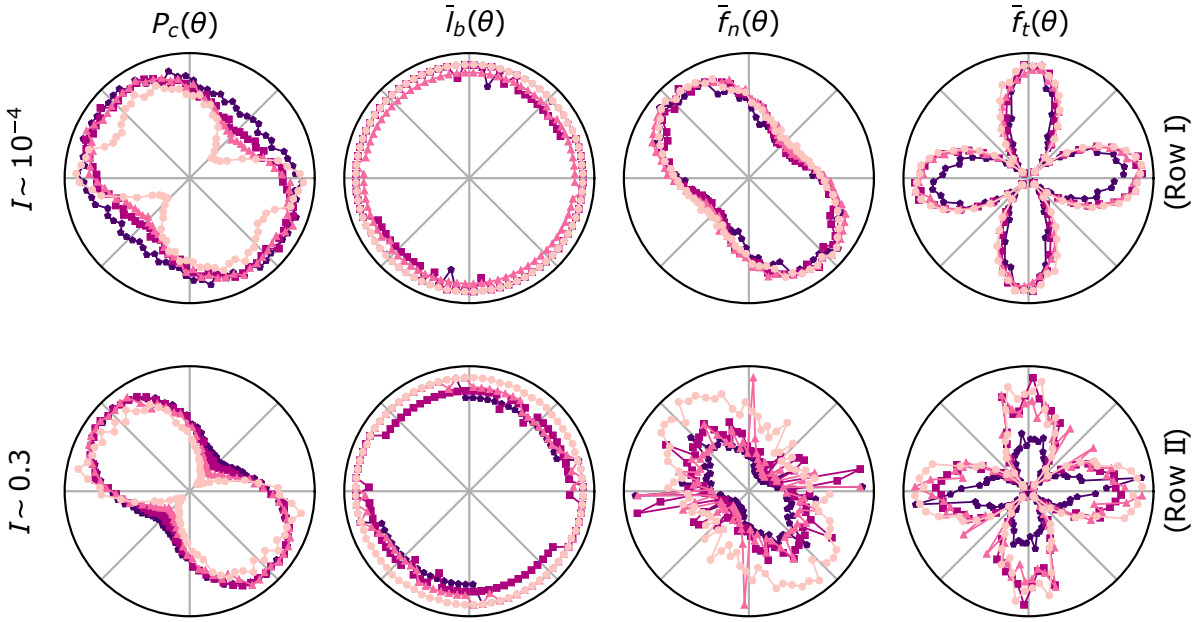

Figure 4.9. Polar representations of the distribution of the proportion of the contact's direction $P_c(\theta)$, the branch length contact $\bar{l}_b(\theta)$, the normal force $f_n(\theta)$ and the normal tangential force $\overline{f}_t(\theta)$ projected onto the shear plane (X, Z) for all polydispersity level, and for (Row I) $I \sim 10^{-4}$ and (Row II) $I \sim 0.3$. The legend of Fig. 4.7 applies to this figure.

4.2.4 Fabric and Force Anisotropies

Now, we will dig into the fabric and forces anisotropies with the aim of understanding why, at high inertial numbers, the shear strength of monodisperse and polydisperse samples differs (see Fig. (4.3)). The system's anisotropies come from the radial distribution of the system's fabric, which accounts for contact direction $P_c(\theta)$ and branch length $l_b(\theta)$, and the radial distribution of the system's forces, which account for normal force $\overline{f}_n(\theta)$ and tangential force $\overline{f}_t(\theta)$ (see Section 2.2.1). In Rows I and II of Fig. 4.10, we present the $P_c(\theta)$, $l_b(\theta)$, $\overline{f}_n(\theta)$ and $\overline{f}_t(\theta)$ projected in the shear plane (X, Z), providing an intuitive representation of the fabric and forces at the contact scale. Regardless of the polydispersity level, contacts and normal forces are aligned to $\sim 3\pi/4$ which is the angle perpendicular to the shear direction ($\sim \pi/4$). The increase of the inertial number induces a change, principally, in the contact direction distribution. For all polydispersity levels λ, $P_c(\theta)$ stretches and narrows towards $\sim 3\pi/4$ and $\sim \pi/4$, respectively. In polydisperse samples, the presence of a large number of small grains does not lead to a significant reduction in contacts in the shear direction, as is the case with monodisperse samples. Last, although is a subtle detail, the branch length distribution $\bar{l}_b(\theta)$ of polydisperse samples shows that the average l_b increases near $\sim 3\pi/4$, indicating that in the shear direction larger grains are being involved.

As our simulations are in three dimensions and the radial fabric and forces distributions are projections onto the shear plane, we found it convenient to obtain the system's anisotropies using definitions proposed by Radjai *et al.* [171] rather than fitting the radial distributions. We

then computed the fabric and force tensors, defined as

$$\boldsymbol{\chi}^{c}_{i,j} = \frac{1}{N_c}\sum \boldsymbol{n}_i \boldsymbol{n}_j, \tag{4.4a}$$

$$\boldsymbol{\chi}^{l}_{i,j} = \frac{1}{N_c}\sum l_b \boldsymbol{n}_i \boldsymbol{n}_j, \tag{4.4b}$$

$$\boldsymbol{\chi}^{n}_{i,j} = \frac{1}{N_c}\sum f_n \boldsymbol{n}_i \boldsymbol{n}_j, \tag{4.4c}$$

$$\boldsymbol{\chi}^{t}_{i,j} = \frac{1}{N_c}\sum f_t \boldsymbol{n}_i \boldsymbol{t}_j \tag{4.4d}$$

and with them, we derive the anisotropies from the principal values of the tensors as:

$$a_c = 2\frac{\boldsymbol{\chi^c_1} - \boldsymbol{\chi^c_3}}{\boldsymbol{\chi^c_1} + \boldsymbol{\chi^c_3}}, \tag{4.5a}$$

$$a_l = 2\frac{\boldsymbol{\chi^l_1} - \boldsymbol{\chi^l_3}}{\boldsymbol{\chi^l_1} + \boldsymbol{\chi^l_3}} - a_c, \tag{4.5b}$$

$$a_n = 2\frac{\boldsymbol{\chi^{f_n}_1} - \boldsymbol{\chi^{f_n}_3}}{\boldsymbol{\chi^{f_n}_1} + \boldsymbol{\chi^{f_n}_3}} - a_c, \tag{4.5c}$$

$$a_t = 2\frac{\boldsymbol{\chi}^{f^*}_1 - \boldsymbol{\chi}^{f^*}_3}{\boldsymbol{\chi}^{f^*}_1 + \boldsymbol{\chi}^{f^*}_3} - a_c - a_n, \tag{4.5d}$$

with $\boldsymbol{\chi}^{f^*} = \boldsymbol{\chi}^{n} + \boldsymbol{\chi}^{t}$. When obtaining the sample's anisotropies using these definitions and correlating the sum of them with the effective friction coefficient μ, we find a very good agreement between these two for all samples, validating this relationship for high inertial numbers and different polydispersity levels (see Fig. 4.10). Therefore, if the sum of the anisotropies serves as a clue to understanding macroscopic friction, we can rely on them to comprehend why the shear strength differs between polydisperse and monodisperse samples at high inertial numbers. Note, in Fig. 4.10, that samples with $I \lesssim 0.1$ are grouped for all λ evidencing that the residual shear strength is independent to the polydispersity. On the contrary, for $I \gtrsim 0.3$ the shear strength of monodisperse samples is considerably higher than the shear strengh of polydisperse samples.

Now, we will take a look to each one of the system's anisotropies to comprehend the origin of the samples' shear strength (see Fig. 4.11). The system's anisotropies, computed with Eq. (4.5), reveal that the contact a_c and normal force a_n anisotropies are the largest and the ones that contribute the most to the system's shear strength. The latter observation is in agreement with previous studies [31, 32, 34–36], and although there are certain differences, it holds true for all samples regardless of their inertial number or polydispersity. The increase of I notably affects the contact anisotropy a_c that constantly grows for all polydispersity levels λ,

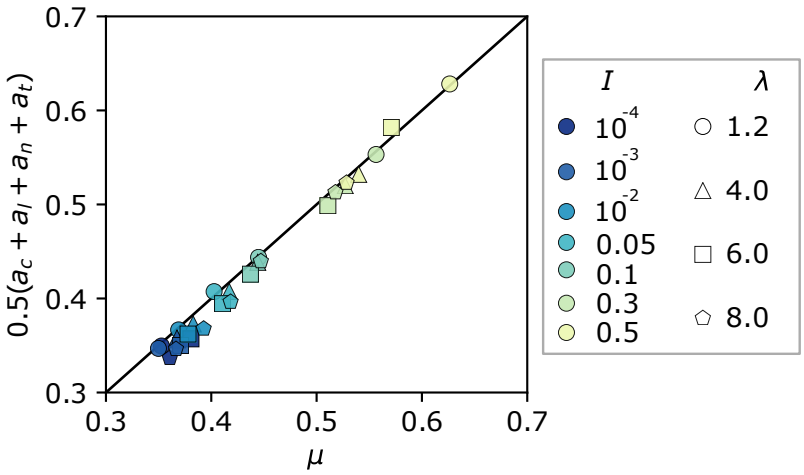

Figure 4.10. Correlation between the effective friction coefficient μ and the sum of the fabric and forces anisotropies according to Eq. (2.10) for all λ (marker's shape) and all I (marker's colour). The line stands for the 1:1 ratio

but being larger for $\lambda = 1.2$. The other fabric contribution, the anisotropy coming from the branch length distribution, is small for all cases. However, for polydisperse samples, a_l tends to have a slight increase with I because larger grains are involved in the contacts perpendicular to the shear direction. As a function of the inertial number I, the normal force anisotropy a_n has a contrasting variation that depends on the sample's polydispersity. In all cases, a_n is larger for polydisperse samples than for monodisperse samples, but the increase of the system's inertia makes that a_n for $\lambda = 1.2$ decrease while it remains nearly constant for polydisperse samples. Last, the other force contribution, the anisotropy coming from the tangential force distribution, is a small anisotropy that has a tiny growth with the inertial number for all λ.
The previous observations point to the following: the contact a_c and normal force a_n anisotropies are the foremost microstructural contributions to the system shear strength; and both depend on the polydispersity level. a_c is larger in monodisperse cases, and a_n is larger in polydisperse cases. For inertial numbers $I \lesssim 0.1$, the independence of the systems shear strength to the size polydispersity because there is a almost perfect compensation compensation between a_c and a_n. On the contrary, for $I \gtrsim 0.3$, the slow increase of the geometric anisotropy a_c and the nearly constant evolution of a_n in polydisperse systems is not enough to compensate the rapid increase of a_c in monodisperse systems, explaining the why the macroscopic friction of polydisperse and monodisperse differ at large inertial numbers.

4.3 | Conclusions

In this study we did simulations of polydisperse granular materials in a shear cell geometry through Discrete Element Methods based on the Non-Smooth Contact Dynamics approach. In this geometry, we varied the systems' inertial number for studying the macroscopic behaviour and the grains' interaction at the contact scale.

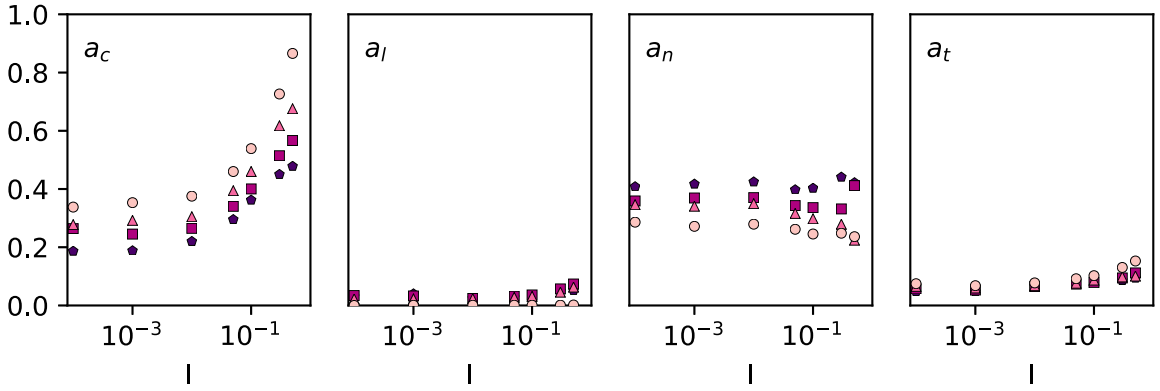

Figure 4.11. Contact a_c, branch length a_l, normal force a_n and tangential force a_t anisotropies as a function of the inertial number I. The legend of Fig. 4.7 applies to this figure.

We showed that the shear strength of granular materials is independent of the polydispersity at low inertial numbers, where the flow could be consider as quasi-static, being in agreement with the main conclusion of Chapter 3, and extended this conclusion to systems in the dense regime with higher inertia $I \in [10^{-4} - 0.1]$. For larger inertial numbers, we evidenced that the shear strength of monodisperse systems is larger than the shear strength of polydisperse. We showed that the distinction in shear strength between monodisperse and polydisperse samples arises from a distinct evolution of the system's anisotropies with the inertial number. The contact anisotropy, which is the most significant contribution, grows faster for monodisperse samples than for polydisperse samples because small grains in polydisperse samples tend to homogenise the distribution of the contact direction. Moreover, we showed that the equivalence between shear strength and the sum of the anisotropies remains true for polydisperse samples with high inertial numbers.

We evidence that the laws linking volume and friction with the inertial number remain true for polydisperse samples and they are valid for a wide range of inertial numbers $I \in [10^{-4} - 0.1]$, computing the systems inertial number with the grain diameter that holds 50% of the cumulative mass (or volume). Therefore, in this inertial number range and in the perspective of implementing rheological models for studying large deformation of polydisperse materials, we would suggest characterizing the bulk material with the diameter d_{50}.

The normal force between two grains in contact increases with the size of the grains, and strong and weak normal forces coincide with *short* and *long* branch lengths. We show that the force between grains in contact increases proportionally according to a power-law function, the exponent of which depends on the system's inertial level. As the inertial number grows, the exponent decreases, narrowing the force gap between short and long contacts and leading to a homogenisation of the contact force that tends towards the main force.

In this study, we did not account for gravity, and segregation phenomena are not prone to occur. Further research might explore the influence of polydispersity in segregated systems or investigate the impact of size segregation on the friction and volume laws and the resulting force network. We simulated shear cells where boundaries impose pressure and velocity; further

research could extend our observations to free surface systems where segregation occurs and the system's inertial number varies with height.

CHAPTER 5

Collapse of Dry and Immersed Polydisperse Columns: A 2D Numerical Study

This chapter is based on the paper *Collapse of dry and immersed polydisperse granular columns: A unified runout description* by Oscar Polanía, Miguel Cabrera, Mathieu Renouf, and Emilien Azéma published on August 22nd 2022 in Physical Review Fluids **7**, 084304 [172].

Resume

The granular column collapse is a simplified version of granular flows like landslides, avalanches and other industrial processes mobilised in air or within a fluid. In this configuration, the grains collapse in an accelerating phase, reaching a state of constant spreading velocity until they decelerate and stop. Granular flows commonly involve grains of different sizes, a property termed polydispersity. Understanding the role of polydispersity remains a challenging task that is often analysed with nearly monodisperse systems and demanding a series of simplifications when coupled with a fluid in a numerical model. Here, we study the effect of grain size polydispersity in dry and immersed granular columns, using a FEM–DEM model for fluid–grain interactions. We show that the velocity of the column collapse and runout distance decrease with an increase in the level of polydispersity in immersed conditions and remain nearly independent of the level of polydispersity in dry conditions. Moreover, we find that the runout scales with the spreading front kinetic energy, weighted by the ratio between the grain's density and the density difference between grains and fluid. This scaling helps in identifying the governing processes in polydisperse granular columns, unifying the runout description of both dry and immersed collapses, and indicating that the column initial packing fraction is the governing parameter.

5.1 | Methods

5.1.1 Coupled FEM–DEM model

We used a coupled Finite Element Method (FEM) with a Discrete Element Method (DEM) for simulating the collapse of a granular column in different ambient fluids. For the fluid motion, we employed a continuous representation solved with a finite element spatial discretization combined with an implicit temporal discretization of the incompressible Navier-Stokes equations

[115]. The granular system is simulated with the Non-Smooth Contact Dynamics approach (NSCD) developed by Moreau [108] and Jean [109]. The method couples the grain discrete solution with the fluid continuum solution by a loop solver that first obtains the packing fraction ϕ within each mesh element and then computes the resultant fluid velocity u, fluid pressure p, and grains-fluid interaction forces f with the current state variables, which are the fluid velocity u, the fluid pressure p, and the grains velocity v. Grains-fluid interactions forces considered in the model are buoyancy and drag. The coupled computation results in the grain source terms for the next time step of the DEM computation, updating the grain position. In this approach, a coupled coarse-scale solution is an appealing approximation for the fluid motion, being capable of managing polydisperse systems with high packing fractions, and demanding special care in the mesh sizing relative to the maximum grain diameter (see the equations and more details of the method in the section *Equations in the FEM-DEM simuations* at the end of this chapter). We use, out of simplicity, two open-source software for the simulation of the granular column collapse. LMGC90 is used for dry granular columns and MigFlow is used for immersed granular columns. Both software employ equivalent formulations of the DEM. We have made the necessary tests to justify the implementation of both codes, resulting in equivalent macroscopic behaviours. For faster simulations, we use parallel computing available in LMGC90 and use PETSc4py package [173] for solving the fluid motion equations in MigFlow. An immersed granular column collapse is intrinsically a three-dimensional process, allowing fluid percolation through the moving granular media in all directions. In our simulations, the granular domain is simplified into a two-dimensional representation, where fluid percolation is obstructed by a large packing fraction, larger than in a three-dimensional system. An alternative for solving the grain-fluid interaction, representing the three-dimensional packing fraction within a two-dimensional system, is to reduce the grain's diameter, seen by the fluid phase, by an ad hoc factor. Kumar *et al.* [113], employing a different framework with a DEM coupled with a Lattice Boltzmann Method, use a factor of 0.9 to model the permeability of a three-dimensional case with a two-dimensional approach. In this work, we opt for a similar solution reducing all grain diameters by a factor of 0.9 for representing a three-dimensional packing fraction in a two-dimensional simulation domain when computing the grain-fluid interactions.

We use a constant fluid mesh element size, computing the grain-fluid interaction as a function of the packing fraction. Potential limitations of this approach can be related to the size ratio between the fluid elements and the smallest grains in the system, oversimplifying the momentum transfer between fluid and small grains. However, we focus on the macroscopic effects that polydispersity has on the column collapse controlled by the packing fraction and not by the calculation of the motion of single grains, resulting in a cost-effective numerical framework. Other approaches, such as the one of Capecelatro & Desjardins [174], could be employed to model polydisperse systems and provide a more detailed solution at the grain scale, demanding a higher computational cost.

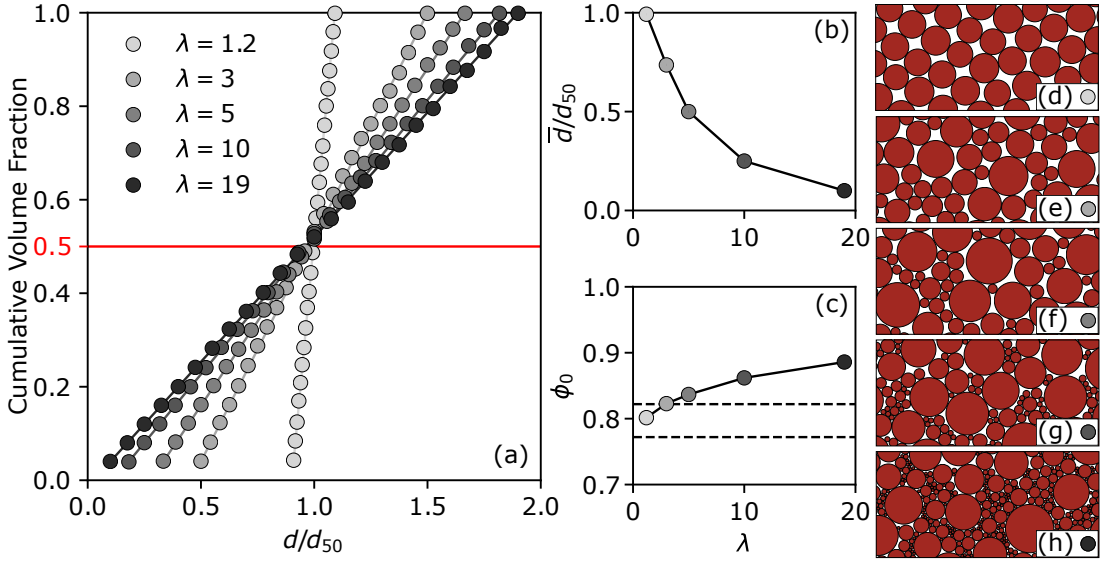

Figure 5.1. (a) Grain Size Distribution GSD as a function of the grain diameter d for all the size ratio $\lambda = d_{\max}/d_{\min}$, with a common cumulative mass of 0.5 for $d_{50} = 0.001$ m. (b) Normalized median grain diameter $\overline{d}/d_{50}$ as a function of λ. (c) Initial packing fraction ϕ_0 as a function of λ, where the dashed lines indicate the random loose $\phi_{\text{rlp}} = 0.772$ and random close packing $\phi_{\text{rcp}} = 0.822$ for monodisperse discs [176, 177]. (d-h) Close up views show the polydispersity level for $\lambda = [1.2, 3, 5, 10, 19]$.

5.1.2 Column construction and collapse

The columns studied in this work consist of a two-dimensional granular system of variable levels of polydispersity, defined by the grain size ratio $\lambda = d_{\max}/d_{\min}$, relating the size of the biggest to the smallest grain. In our simulations, we studied five values of $\lambda = [1.2, 3, 5, 10, 19]$. For all values of λ, we used a grain size distribution GSD that consists of 25 disc diameters, linearly distributed between $d_{\min}$ and $d_{\max}$. In all the resultant GSDs, the number of grains per diameter is set to have the same mass. This means that each grain diameter has $1/25$ of the mass necessary for filling the initial column dimensions. For all GSDs, the grain diameter $d_{50} = 0.001$ m has a cumulative unitary mass, relative to the column total mass, of 0.5. The minimum and maximum diameter are equal to $d_{\min} = 2d_{50}/(\lambda + 1)$ and $d_{\max} = d_{\min}\lambda$, respectively. The median diameter $\overline{d}$ ranges between [0.0001 : 0.001] m (see Fig. 5.1 (a) and (b)). The discs have $\rho_s = 1500\text{kg/m}^3$, with a friction coefficient of 0.3, typically encountered in geomaterials materials [175], and restitution coefficient of 0 found not to affect the collapse behavior of granular columns [134].

The columns initial length was fixed to $L_0 = 0.05$ m, and the initial height H_0 varied between [0.015 : 0.25] m, covering seven column aspect ratios $A = [0.3, 0.5, 0.75, 1.0, 2.0, 3.5, 5.0]$ and allowing the study of short and tall columns. Cabrera & Estrada [141] showed that grain-size effects become negligible in the column final runout when the ratio between L_0 and the average grain diameter $\langle d \rangle$ is at least 50. In this work, we fulfilled this condition in all cases, considering $\langle d \rangle$ as d_{50} or $\overline{d}$. Moreover, the total number of grains n in each column varies with A and λ, ranging between $n \approx [1000 : 110000]$.

The columns were built as an initial gravity deposit of grain in a rectangle with dimensions L_0 and H_0, and were let to settle by self-weight. The columns had an initial packing fraction ϕ_0, varying between loose to very dense packings relative to the random loose ϕ_{rlp} and random close packing ϕ_{rcp} for monodisperse discs [176, 177] (see Fig. 5.1(c)). The column collapse is stared by virtually removing the lateral wall and is driven by the grains self-weight with $g = 9.81\ \mathrm{m/s^2}$. L_{f} and H_{f} describe the deposit geometry when the collapse finishes (see Fig. 5.2). We measured L_{f} as the position of the farthest grain with three active contacts still in touch with the deposit bulk *. Three repetitions of each combination of λ and A were performed by randomly shuffling the grains location, resulting in a new gravity deposit and avoiding the effect of the initial grain spatial distribution within the column. In this work, a total of 189 simulations were performed. The time step was chosen relative to d_{min} and H_0 as $dt < d_{\mathrm{min}}/\sqrt{2H_0 g}$. For simplicity, we used $dt = 0.0001\ \mathrm{s}$ and, for extreme cases with $A = [3.5, 5.0]$ and $\lambda = [10, 19]$, $dt = 0.00001\ \mathrm{s}$. Note that both dt values satisfy the inequality.

The fluid was solved in a rectangular domain composed of a regular mesh of triangular elements of characteristic length $5d_{50}$. The domain boundaries were considered as walls with no flux across them, and with pressure set to zero only at the upper-wall. The mesh domain was found to be sufficiently large for avoiding pressure reflections at the foremost boundaries. The fluid had the properties of water with density $\rho_{\mathrm{f}} = 1000\ \mathrm{kg/m^3}$ and viscosity $\mu_{\mathrm{f}} = 0.001$ Pa s. Moreover, the physical parameters of grains and fluid that we used have been previously employed to validate the numerical framework approximation [115].

In this work, assuming the fluid density and viscosity as zero, the collapse of dry columns simulated flows in the free-fall regime with the Stokes number $\mathrm{St} \gg \mathrm{St}^*$ and $\chi \gg \chi^*$. Note that the * marks the transition limits presented by Courrech du Pont *et al.* [79] (see Fig. 2.3). Within these regimes, immersed columns focused on flows that belong to the inertial regime with $\mathrm{St} = 3.37$ and $\chi = 1.22$, both considering the representative grain diameter as d_{50}. These values of St and χ allowed the study of granular flows near the transition between inertial and viscous flows, relative to monodisperse systems, aiming at highlighting the role of the level of polydispersity in the collapse regimes. Our immersed simulations had $\mathrm{St}/\chi = 2.76$, a value that is close to the regime transition at $\mathrm{St}/\chi = 2.5$ (see figure 2.15). In Sec. 5.3 we refer to the relevance of studying polydisperse columns near this regime transition.

5.2 | Collapse sequence

During the collapse of a granular column, the grains in movement are separated from the motionless grains by a sliding or failure plane. In the sequence of dry column collapses, we observe the rapid development of this sliding plane that, regardless of the level of polydispersity, shows a similar inclination in columns with the same aspect ratio A at a similar collapse instant. This similarity in the collapse dynamics occurs from beginning to end of the collapse sequence,

*We have chosen to get the front position this way because we avoided identifying outlier grains as part of the collapse front.

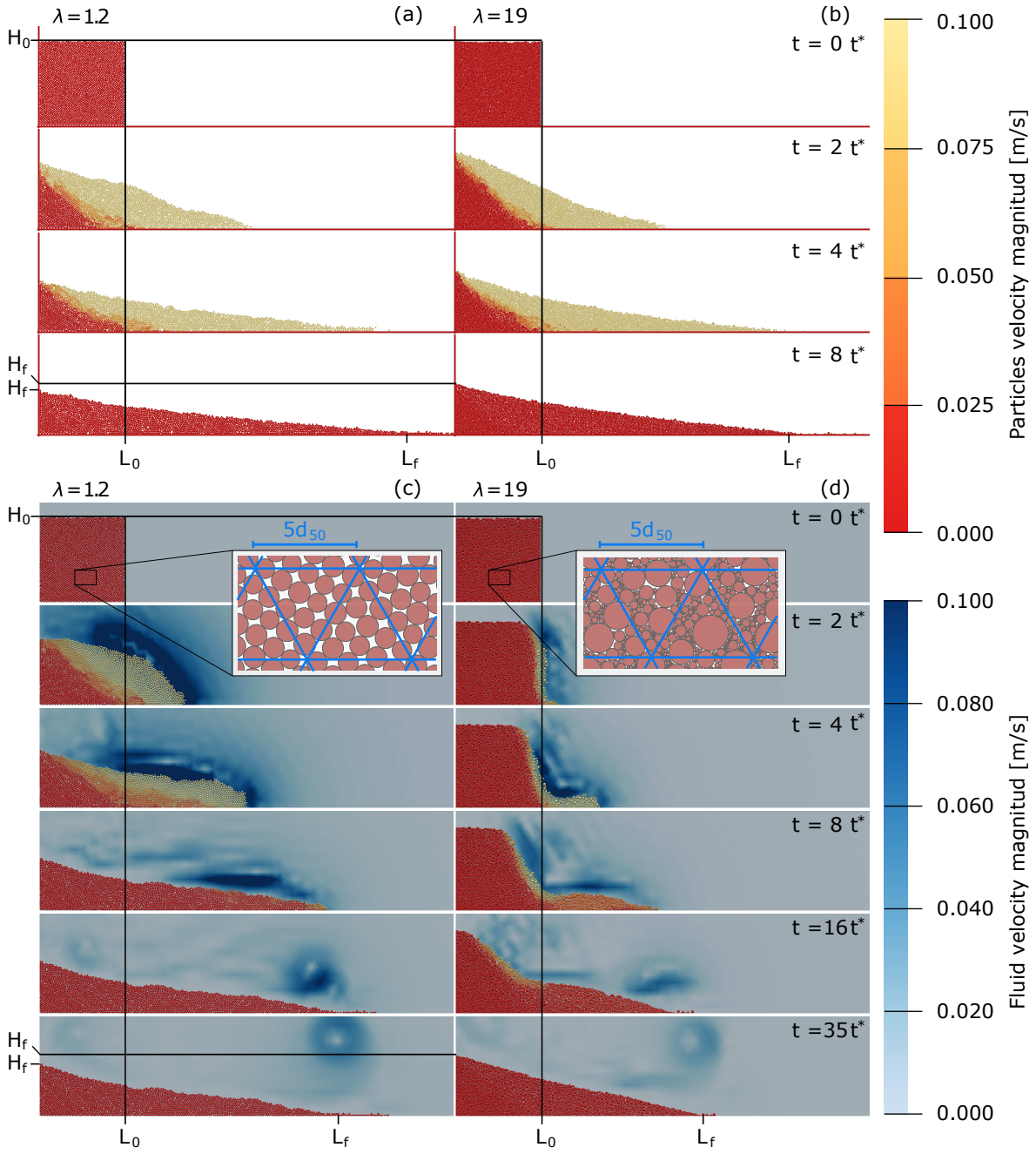

Figure 5.2. (a, b) Collapse sequence of dry and (c, d) immersed columns. The columns have an aspect ratio $A = H_0/L_0 = 1.0$ and grain size ratio $\lambda = [1.2, 19]$ (left, right). t^* is a characteristic time $t^* = \sqrt{H_0/g^*}$, where g^* stands for a reduced gravity due to the ambient fluid buoyant force $g^* = g\ \Delta\rho/\rho_s$, and $\Delta\rho = \rho_s - \rho_f$ is the density difference between grains and fluid. The insets in (c) and (d) compare the grains size with the fluid mesh size.

implying that the sliding plane is independent of λ (see Fig. 5.2 (a) and (b)). On the contrary, it becomes evident that polydispersity changes the collapse sequence of immersed collapses (see Fig. 5.2 (c) and (d)). Columns with low levels of polydispersity ($\lambda = 1.2$) rapidly develop an inclined sliding plane of a thick layer of moving grains, and at high levels of polydispersity ($\lambda = 19$) the sliding plane tends towards a thin and nearly vertical layer of moving grains, while most of the core remains nearly static. In the latter, the initial mobilization results in the free-fall of grains at the column release face, slowly propagating inwards as a sequence of steep and thin slides (see movies in the supplementary material of the published paper [172]). The inwards propagation of thin slides has been previously observed experimentally by Thompson & Huppert [178] on the study of immersed sand column collapses, suggesting that the occurrence of such behaviour is caused by the grain angularity. Here, we argument that an increase in λ leads to more stable columns, by means of denser packings (see Fig. 5.2 (b)), frustrating the fluid percolation through the whole collapse sequence. In consequence, the frustrated percolation limits the amount of mobilized grains, leading to the formation of thin nearly vertical slides.

After the initiation of the column collapse, the evolution of the front position has a distinct initial stage of acceleration until reaching a steady horizontal propagation. Later, the front decelerates and stops at the runout distance L_f. Fig. 5.3 shows the instantaneous evolution of the front position L_i normalized by H_0, for a timeline scaled by a characteristic time

$$t^* = \sqrt{H_0/g^*}, \tag{5.1}$$

where g^* stands for a reduced gravity due to the ambient fluid buoyant force (see Eq. 2.20). Here in, the factor $\Delta\rho/\rho_\mathrm{s} = 1/3$ and $\Delta\rho/\rho_\mathrm{s} = 1$ stands for immersed and dry scenarios, respectively. During the steady propagation stage, dry column collapses share a common slope regardless of λ, while for immersed columns collapses, this only occurs at low levels of polydispersity ($\lambda < 5$), and the whole column collapse lasts longer with the increment of λ. The slope between L_i and t represents the front velocity U computed in the interval where the front propagation has a steady stage with no acceleration (see inset of Fig. 5.3 (a)). Moreover, L_f is consistently longer in dry columns than in immersed columns (see Fig. 5.3 (b)). The relationship between L_f, λ, A, and U is further discussed by means of a simplified model in Sec. 5.5. A table with the parameters of each simulation and the main results that support this study is included as supplementary material in the published paper [172].

5.3 | Front kinematics

From the previous observations, we can highlight that the level of polydispersity has a significant effect on the collapse sequence of immersed columns but a minimal effect on dry columns. As a result, highly polydisperse columns last longer in immersed conditions until coming to a full halt. The common slope during the steady propagation stage for dry cases in Fig. 5.3 (a) indicates that U is a function of H_0, confirming the proportionality proposed by Bougouin & Lacaze [133], who worked with monodisperse columns, and extending it to polydisperse

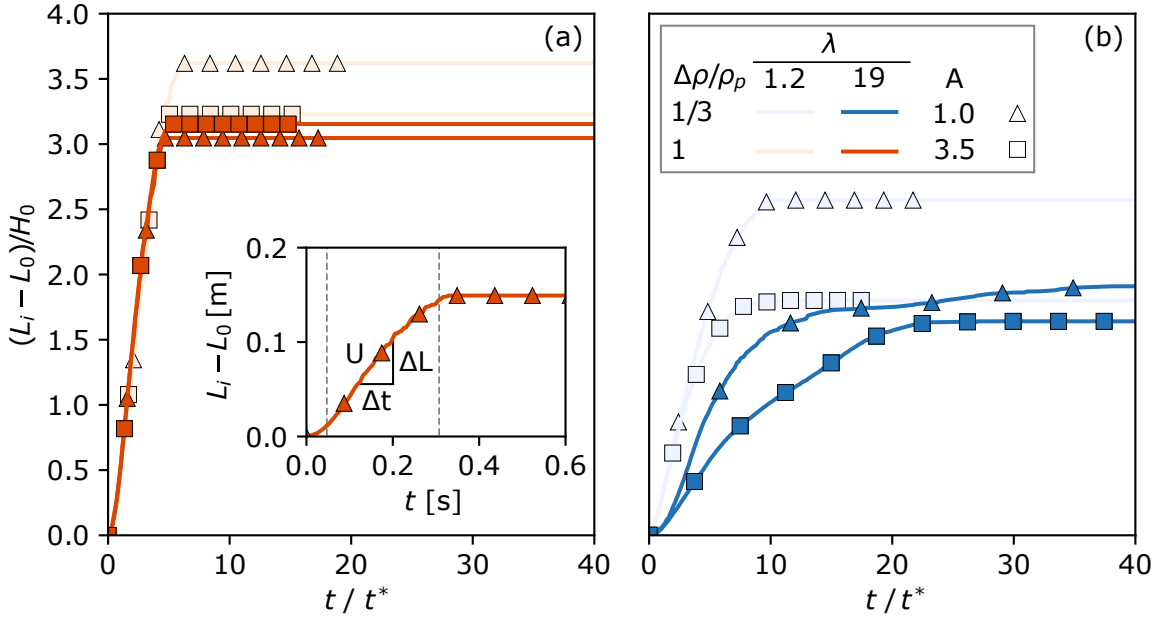

Figure 5.3. Front position evolution L_i during collapse and relative to the column initial dimensions (L_0, H_0), for (a) dry and (b) immersed columns and for $A = [1.0, 3.5]$ ($\triangle$, $\square$), respectively, and $\lambda = [1.2, 19]$. The inset in (a) shows the evolution of L_i for $\lambda = 19$ and $A = 1.0$, and dashed gray lines delimit the collapse steady propagation stage interval.

columns in dry conditions. In our results, U fluctuates around a characteristic velocity of the free-fall regime ($U^* \approx 0.55$) in dry collapses. Those fluctuations are linked to the increment of λ, which overall leads to slightly faster collapses (see Fig. 5.4). Columns with $A < 1$ present lower values of U related to a shorter accelerating stage in its collapse sequence. Moreover, the normalized front velocity ranges between $U^* = [0.19 : 0.24]$ for immersed columns with $\lambda \leq 5$. This range is found to be characteristic of collapses between the viscous inertial and inertial regimes. An increment of λ reduces U^* in immersed cases, being more evident on columns with $A \geq 2$. This observation is notable and suggests that an increment in λ makes the collapse transition towards a viscous regime and an increment in the column aspect ratio A enhances this regime transition.

Under the assumption that U is the velocity resulting from the whole column mass M, we compute the kinetic energy during the steady propagation stage as

$$E_\mathrm{K}^\mathrm{U} = MU^2/2, \tag{5.2}$$

with $M = \sum_i^n m_i = \phi_0 \rho_\mathrm{p} H_0 L_0$, where m_i denotes the mass of each grain. At first glance, immersed collapses are less energetic than dry collapses. The energy of dry collapses increases with polydispersity because columns are denser and, contrary to immersed collapses, tend to be slightly faster. On both cases, E_K^U grows as a function of A with a power law with an exponent of power index 2, regardless of the column level of polydispersity (see Fig. 5.5), while for immersed cases, this trend breaks at $\lambda > 5$. Note that, for immersed columns, the increment of λ consistently reduces E_K^U. Furthermore, the energy of tall ($A > 2$) and highly polydisperse columns ($\lambda \geq 10$) deviates from the quadratic tendency. This deviation of E_K^U

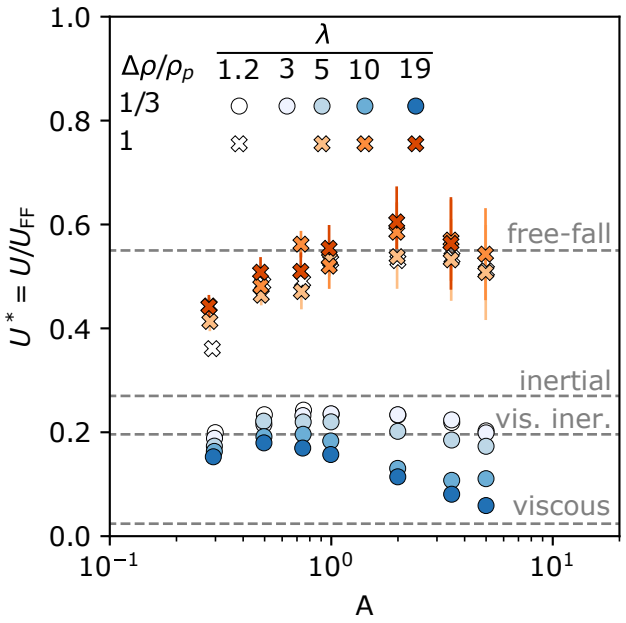

Figure 5.4. Normalized front velocity U as a function of the column aspect ratio A. U_{FF} is the free fall velocity $U_{\mathrm{FF}} = \sqrt{2H_0 g^*}$. The dashed lines are the characteristic velocities found by Bougouin and Lacaze for free–fall ($U^* \approx 0.55$), inertial ($U^* \approx 0.27$), viscous inertial ($U^* \approx 0.196$), and inertial regimes ($U^* \approx 0.024$) [133]. $\Delta\rho/\rho_{\mathrm{s}}$ is the density difference between grains and fluid $\Delta\rho = \rho_{\mathrm{s}} - \rho_{\mathrm{f}}$, and grains' density ρ_{s}, where $\Delta\rho/\rho_{\mathrm{s}} = 1/3$ for immersed cases and $\Delta\rho/\rho_{\mathrm{s}} = 1$ for dry cases. Error bars correspond to the standard deviation of U between repetitions. Note that in immersed cases, the error bar is smaller than the marker size.

coincides with the fact that the front velocity U transitions from the inertial to the viscous regime by the joined effect of the levels of polydispersity λ and the column aspect ratio A.

5.4 | Collapse mobility

A common characteristic between dry and immersed columns is that the final runout increases with A and it follows a function in the form of a power law $L^* = A^b$, where $L^* = (L_{\mathrm{f}} - L_0)/L_0$. Although the power-law holds for polydisperse systems in dry and immersed cases (see Fig. 5.6 (a)), the final runout L^* of immersed columns within an ambient fluid tends to shorten with polydispersity. L^* collapses on a power law with the exponent $\beta = 1$ for columns with $A < 2$. For taller columns $A \geq 2$, L^* deviates with $b = [0.92, 0.56]$ for dry and immersed cases, respectively, representing the transition from short to tall columns. The exponent $b = 1$ for short columns agrees with previous numerical studies [130, 132, 141]. For tall columns, the exponent $b = 0.92$ exceeds the common range $0.66 \leq b \leq 0.80$ [123, 130, 141], and for immersed collapses the result $b = 0.56$ is within the range $0.56 \leq b \leq 0.64$ [122, 132].
An interesting remark is that L^* appears to be limited by the effect of λ for both dry and immersed columns, showing common values of L^* within the same A. This limited effect of λ on L^* is independent of the polydispersity level in dry columns, confirming the conclusions of Chapter 3 and previous works [17, 32, 59, 179], and is seen in the immersed columns as a decrease of L^* when λ increases, saturating for $\lambda \geq 10$ (see Fig. 5.6 (c)). The reduction of

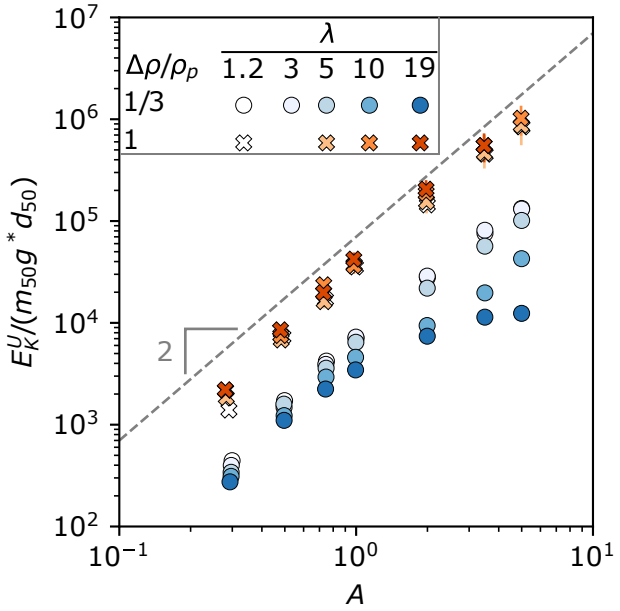

Figure 5.5. Kinetic energy $E_{\mathrm{K}}^{\mathrm{U}} = MU^2/2$ during the steady propagation stage normalized by the characteristic energy of a single grain as a function of the column aspect ratio A. M is the column mass, d_{50} is a representative grain diameter, m_{50} is the mass of a single grain with diameter d_{50}, and g^* is the reduced gravity. Note that d_{50} and m_{50} are constant for all λ. Error bars correspond to the standard deviation of $E_{\mathrm{K}}^{\mathrm{U}}$ between repetitions.

the final runout in immersed cases suggests that the macroscopic friction angle depends on the level of polydispersity up to a given value of λ, here observed for $\lambda \leq 5$.

5.5 | Scaling: kinetics and runout

Based on the previous sections, we can make global observations for dry and immersed conditions relating the collapse energy and the column final runout. Dry columns are more energetic and have a longer runout than immersed columns. In immersed columns, the energy decreases with the level of polydispersity, and the final runout tend to decrease with the increment of the polydispersity reaching a limit controlled by the macroscopic friction angle. Therefore, we propose a unified scaling for the processes involved in the column mobility and collapse kinematics for both dry and immersed cases (see Section 2.4.3 where we discussed the link between the runout a kinematic used in previous works). Here, we propose a simplified model with the analogy of a sliding block with an initial velocity and opposite resistance such that $M\ddot{x}(t) = -k\dot{x}(t)$, where $\dot{x}(t)$ and $\ddot{x}(t)$ are the block velocity and acceleration, respectively, and w is an equivalent suspension viscosity. Solving this equation, and considering the initial velocity as U and the initial position as L_0, we get at an infinite time:

$$L_{\mathrm{f}} - L_0 = MU/w. \tag{5.3}$$

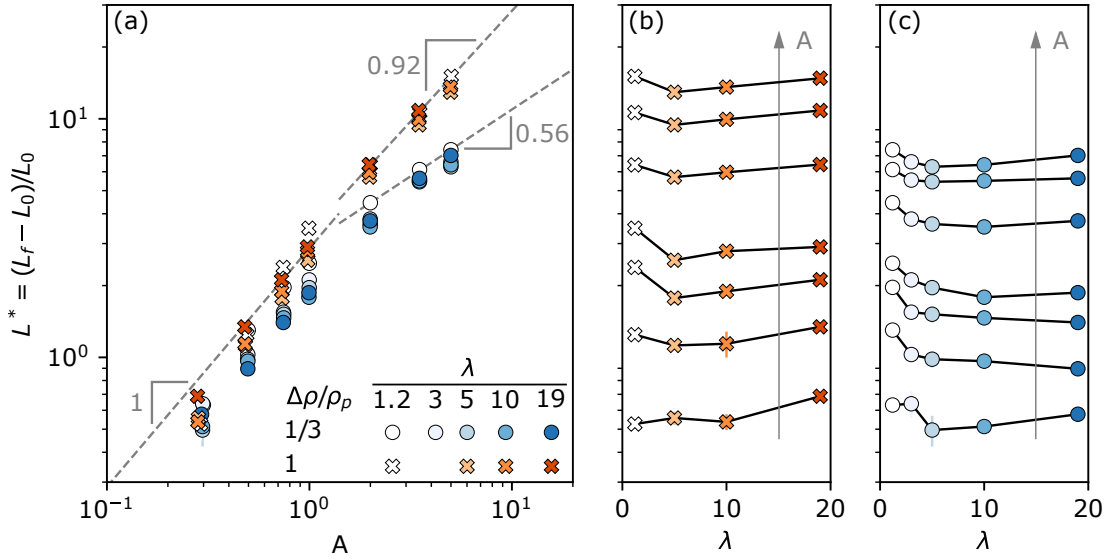

Figure 5.6. (a) Normalized final runout L^* as a function of the column aspect ratio A, and as a function of the GSD size ratio λ for (b) dry and (c) immersed cases. The dashed lines in (a) are the best fits for a function in the form of $L^* = aA^b$ for $\lambda = 1.2$ with the values of b shown in gray. L_0 is the initial column length, and L_f is the final runout. Error bars correspond to the standard deviation of L_f between repetitions.

We divide both sides by L_0 and include E_K^U in Eq. 5.3, obtaining

$$L^* = \frac{\sqrt{2}}{wL_0}\sqrt{M}\sqrt{E_K^U}. \tag{5.4}$$

Knowing that L_0 is a constant and considering that viscous effects are carried by the collapse horizontal spreading velocity U, we can interpret Eq. 5.4 as

$$L^* \propto \sqrt{M}\sqrt{E_K^U}. \tag{5.5}$$

With these considerations the column final runout and the collapse kinematics of dry and immersed cases notably scale (see Fig. 5.7). Although dry and immersed configurations scale on different slopes, it is remarkable that the simplified model collapses for all levels of polydispersity.

An evaluation of the dependency of L^* with the model variables M and E_K^U shows a clear distinction in the trend for $M > 5$, that corresponds to columns with an aspect ratio $A \geq 2$. Note in Fig. 5.6 (a) that the trend breaks for $A \geq 2$, distinguishing between short and tall columns. Consequently, M allows an alternative distinction between short and tall columns, considering that taller columns result in a larger amount of grains (see Fig. 5.8 (a)). As a function of E_K^U, there are two parallel trends that follow a power law with an exponent of power index 0.5 (see Fig. 5.8 (b)), indicating that the energy difference of dry and immersed cases depends on a relation between the grain and the ambient fluid.

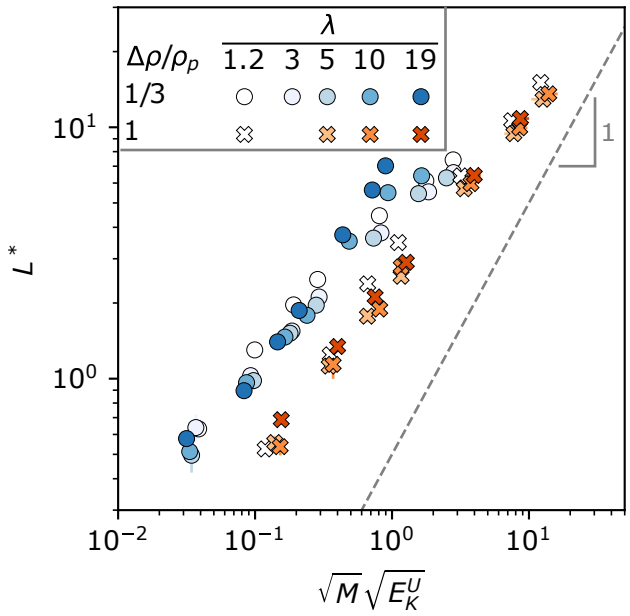

Figure 5.7. Scaling of the normalized final runout L^* with the column kinematics according to Eq. (5.4). M is the column mass, and $E_{\mathrm{K}}^{\mathrm{U}}$ is the kinetic energy. Error bars correspond to the standard deviation of L^* and $E_{\mathrm{K}}^{\mathrm{U}}$ between repetitions.

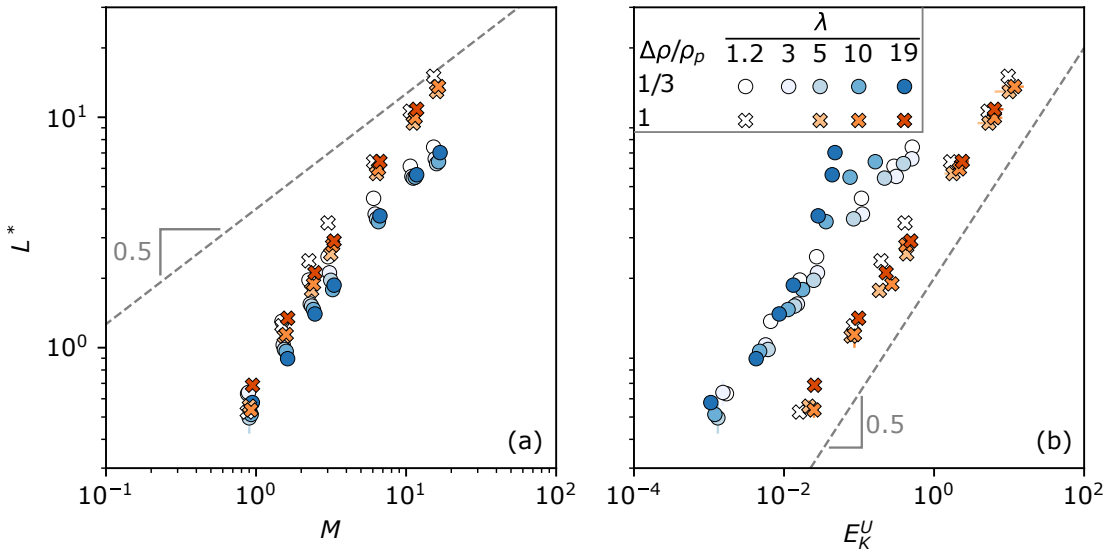

Figure 5.8. Normalized runout L^* as a function of (a) the column mass M, and (b) the kinetic energy $E_{\mathrm{K}}^{\mathrm{U}}$ during the steady propagation stage. Error bars correspond to the standard deviation of L^* and $E_{\mathrm{K}}^{\mathrm{U}}$ between repetitions.

Based on the latter observations, we include the column effective mass $M^* = M\ \Delta\rho\ /\ \rho_s$ in Eq. 5.5, and obtain:

$$L^* \propto (M^*)^{\delta} \left(\frac{\rho_s}{\Delta\rho}\right)^{\epsilon} \left(E_K^U\right)^{\zeta}, \tag{5.6}$$

where the exponents δ, ϵ and ζ weigh the influence of each of the column controlling factors. The best scaling is obtained by setting $\delta = 0$, disregarding the distinction between short and tall columns, and setting $\zeta = 0.5$ and $\epsilon = 1$ resulting in a satisfactory scaling between E_K^U and L^* (see Fig. 5.9). Notably, all columns follow a common trend, despite the ambient fluid, the level of polydispersity, and the column aspect ratio. Deviations in the trend occur for immersed tall columns with $\lambda = 19$ when there are strong fluid effects (e.g., buoyancy and drag force), reducing the collapse velocity and implying a regime transition from inertial to viscous. Moreover, we include new simulations with $\rho_s = 2500\ \mathrm{kg/m^3}$ and $\Delta\rho/\rho_s = 3/5$, showing the reliability of the scaling and suggesting that the collapse is governed by a distinct combination of the factors $\Delta\rho/\rho_s$ and E_K^U. This scaling suggests, with the considerations mentioned above, that the column kinematics are directly related with the final runout, linking a faster collapse with a longer runout. Notably, the packing fraction ϕ_0, which increases with λ, can be suggested as a key parameter that governs the column kinematics, being stronger in immersed granular flows, and allows the characterization of the granular assembly by a characteristic grain diameter (e.g., $\langle d \rangle$, d_{50}, $\overline{d}$).

We acknowledge that the proposed scaling is an oversimplification of the entire physical problem. However, it is remarkable that this simple scaling captures the final runout and kinematics of a granular column collapse when dry or immersed, and in a wide range of polydispersity levels. Notably, the scaling works well for the polydispersity levels that we employ, but deviates when fluid effects are strong. Although the level of polydispersity is not explicit in the scaling, it is essential in the computation of E_K^U, because the column bulk density varies with λ, and we evidence the dependency of the front velocity U to the level of polydispersity.

5.6 | Conclusions

We studied the collapse of granular columns in dry and immersed conditions with a coupled Finite Element Method and Discrete Element Method. We systematically varied the column aspect ratio, covering a range of short and tall columns while exploring different levels of polydispersity. Our results with monodisperse systems, for both dry and immersed conditions, are in agreement with previous experimental and numerical results. Moreover, we evidenced that the motion of immersed collapses is highly dependent on the level of polydispersity. We showed, in immersed columns, that the increment of the column polydispersity enhances the fluid–grains interactions, by increasing the column packing fraction and affecting the collapse sequence evolution. On the contrary, polydispersity does not have a strong effect on the collapse sequence and final runout of dry columns. The principal effect of high levels of polydispersity is the change in the collapse sequence that results in slower front velocities, especially for tall columns, and a retrogressive thin sliding layer. Despite similar initial flow

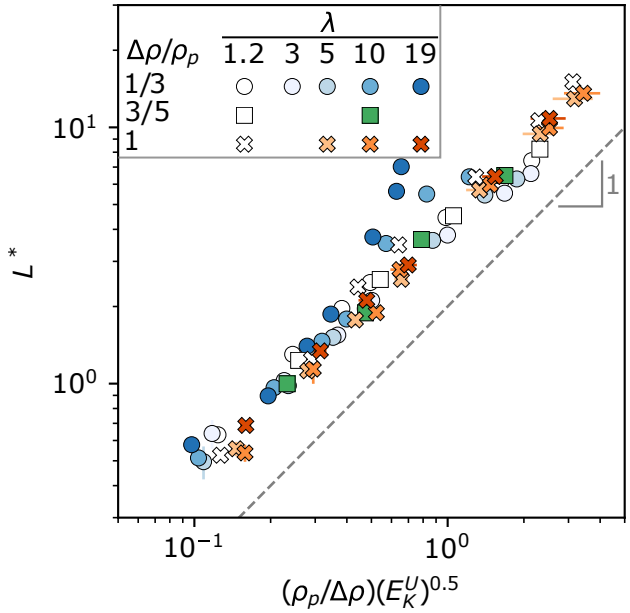

Figure 5.9. Scaling of the normalized runout L^* with the column kinematics according to Eq. (7.1) with $(\delta, \epsilon, \zeta) = (0, 1, 0.5)$. ρ_s is the grains' density, $\Delta\rho$ is the density difference between grain and fluid, and E_K^U is the kinetic energy during the steady propagation stage. Error bars correspond to the standard deviation of L^* and E_K^U between repetitions.

conditions between columns, relative to the Stokes number and the density ratio, there is evidence that an increase in the level of polydispersity results in the reduction of the front velocity, leading the column to transition from an inertial regime towards a viscous regime.

We propose a scaling, that is an analogy of a simple sliding block model that has an initial velocity and an opposite resistance, between the final runout and the front kinetic energy. In this scaling, and for immersed cases, we assume that the front carries all the viscous effects. Remarkably, the variables of the scaling can be easily measured in the laboratory and in numerical experiments. Moreover, this model suggests that, with the considerations mentioned above, the initial packing fraction is the governing factor of the column final runout and kinematics, allowing the characterization of the granular assembly by a characteristic grain diameter. Interestingly, we show that the scaling does not require a distinction of the involved mass, indicating that the final runout is only a function of the fluid-grains density ratio and the front kinetic energy. Regardless of its simplicity, it is notable that this simple scaling captures the final runout and kinematics of a granular column collapse when dry or immersed. Although the level of polydispersity is not explicit in the scaling, it is essential in the computation of the front kinetic energy, and we evidence the dependency of the front velocity to the level of polydispersity.

Finally, this work indicates that polydisperse immersed granular flows do not occur suddenly, rather they progressively slide over thin layers, as the level of polydispersity increases. These results show that highly polydisperse flows will last longer and develop slower flows. The practical implications of this model could be of great use in the hazard assessment of offshore infrastructure against submarine landslides or in the handling of immerse industrial granular systems like fresh concrete, or in pharmaceutical and cosmetic applications.

Although our results are limited by the physical considerations that we have made, they agree with previous experimental and numerical results for monodisperse cases and contribute a novel perspective in the study of immersed polydisperse flows. Further studies could employ more precise physical assumptions, including lubrication to determine if it has a significant role on dense granular flows, or implementing drag forces formulations for polydisperse systems.

Equations in the FEM-DEM simulations

For the fluid phase motion, the incompressible Navier-Stokes equations are solved and averaged using a weight function for considering the influence of particles on the fluid [115]. The packing fraction ϕ is the weight variable that represents the fluid volume $\nu = 1 - \phi$ in the fluid mesh elements. The particle motion is solved with the Non-Smooth Contact Dynamics approach (NSCD). In this method, perfectly rigid particles interact by volume exclusion and Coulomb friction [108, 109]. The method is a class of the DEM, where perfectly rigid bodies interact by volume exclusion and Coulomb friction. In this method, the equations of motion are integrated in a time step obtaining the particles kinematics. This method is convenient for the simulation of highly polydisperse systems, because volume exclusion allows a complete interaction between small and big particles without the need of tailored stiffness parameters as in the smooth DEM class. Also, the method employs a stable integration scheme without the need of stabilization techniques [110].
The following are the equations solved in the FEM-DEM model as proposed in the original paper [115]. The conservation laws for the fluid phase are:

$$\rho_{\mathrm{f}}\left(\frac{\partial \boldsymbol{u}}{\partial t} + \boldsymbol{\nabla}\cdot\frac{\boldsymbol{u}\boldsymbol{u}}{\nu}\right) = \boldsymbol{\nabla}\cdot\left[2\mu_{\mathrm{f}}\nu\boldsymbol{d}(\boldsymbol{u}) - p\boldsymbol{I}\right] + \boldsymbol{f} + \nu\rho_f\boldsymbol{g}, \tag{5.7}$$

$$\frac{\partial \nu}{\partial t} + \boldsymbol{\nabla}\cdot\boldsymbol{u} = 0 \tag{5.8}$$

where $\boldsymbol{u} = \nu\boldsymbol{w}$ is the mean velocity of the fluid phase, p is the pressure, $\boldsymbol{f}$ is the force of the particle-fluid interaction, $\boldsymbol{I}$ the identity tensor, and $\boldsymbol{d}(\boldsymbol{u})$ is the rate of deformation tensor, computed as:

$$\boldsymbol{d}(\boldsymbol{u}) \triangleq \left(\boldsymbol{\nabla}\frac{\boldsymbol{u}}{\nu} + \left(\boldsymbol{\nabla}\frac{\boldsymbol{u}}{\nu}\right)^T\right). \tag{5.9}$$

Both pressure p and fluid velocity $\boldsymbol{u}$ depend on the packing fraction that is computed every time step with the particles position.
The particles motion results from their contact interaction, solved with NSCD, and the particle-fluid interaction. The velocity of a single grain i is computed with Newton second law of motion:

$$\frac{d}{dt}(m_i\boldsymbol{v}_i) = m_i\boldsymbol{g} - V_i\boldsymbol{\nabla}p|_{\boldsymbol{x}_i} - \boldsymbol{F}_{\mathrm{di}}, \tag{5.10}$$

where m, V, $\boldsymbol{x}$ and $\boldsymbol{v}$ are the mass, volume, position, and velocity of a single grain, respectively. The particles-fluid interaction force $\boldsymbol{f}$ (see Eq. 5.7) is represented by the combination of $V_i \boldsymbol{\nabla} p|_{\boldsymbol{x}_i}$ and the drag force $\boldsymbol{f}_{\mathrm{di}}$. Note that for dry simulations, particle-fluid interaction forces are zero.

In our study, the solution is considered two-dimensional assuming the particles as discs of unitary depth and, as consequence, the drag force $\boldsymbol{F}_{\mathrm{di}}$ is computed as:

$$\boldsymbol{f}_{di} = g(\nu|_{\boldsymbol{x}_i}) C_d \; d_i \; \frac{\rho_f}{2} \left(\boldsymbol{v}_i - \frac{\boldsymbol{u}_i}{\nu}\bigg|_{\boldsymbol{x}_i} \right) \left(\boldsymbol{v}_i - \frac{\boldsymbol{u}_i}{\nu}\bigg|_{\boldsymbol{x}_i} \right) \tag{5.11}$$

where d is the diameter of a single particle and C_d is the drag coefficient computed as:

$$C_d = \left(0.63 + \frac{4.8}{\sqrt{Re_i}} \right)^2, \tag{5.12}$$

and the Reynolds number

$$\mathrm{Re}_i = \frac{\sqrt{2d}\nu|_{\boldsymbol{x}_i}}{\mu_{\mathrm{f}}}. \tag{5.13}$$

The function $G(\nu|_{\boldsymbol{x}_i})$, that multiplies the drag force of a single particle, considers the effect that the surrounding particles have on the fluid-particle interaction [96].

$$g(\nu|_{x_i}) = \nu^{-1.8}|_{\boldsymbol{x}_i} \tag{5.14}$$

More details of the Non-Smooth contact Dynamics approach can be found in [108–110] and an extensive description of FEM-DEM model for granular flows can be found in [115].

CHAPTER 6

From Monodisperse to Polydisperse: An Experimental Study of Granular Collapses

This chapter is based on the paper *Polydispersity effect on dry and immersed granular collapses: An experimental study* by Oscar Polanía, Nicolas Estrada, Emilien Azéma, Mathieu Renouf, and Miguel Cabrera submitted to a peer reviewed journal on July 2023.

Resume

The column collapse experiment is a simplified version of natural and industrial granular flows. In this configuration, a column built with grains is let to collapse and spread over a horizontal plane. Granular flows are normally studied with a monodisperse distribution of grains; however, the variety of grain sizes, known as polydispersity, is an important feature of these flows. In this work, we experimentally study the effect that polydispersity has on dry and immersed granular columns. We do an experimental campaign with glass beads of different size for avoiding conflicting effects like grain elongation, angularity or rugosity, allowing us to focus only on the influence that the grain size polydispersity has on granular flows. In our experimental setup, we have included a network of pore pressure transducers along the collapse principal direction. Our work provides a novel insight of the study of polydisperse granular flows, linking the influence that basal pore fluid pressure evolution has on the collapse sequence of systems with increasing polydispersity.

6.1 | Methodology

6.1.1 Experimental Setup and Materials

We conducted the column collapse experiments in a rectangular glass channel $100\ \mathrm{cm}$ long, $60\ \mathrm{cm}$ high, and $18\ \mathrm{cm}$ wide, in dry and immersed conditions. For immersed experiments, we used tap water with density $\rho_{\mathrm{w}} \approx 1000\ \mathrm{kg/m^3}$ and viscosity $\eta_{\mathrm{w}} \approx 0.001\ \mathrm{Pa\ s}$, and up to a level $H_{\mathrm{w}} \simeq 50\ \mathrm{cm}$. The granular columns had an initial length $L_0 \simeq 8.5\ \mathrm{cm}$ and an initial height $H_0 \simeq [4.2, 8.5, 17, 24]\ \mathrm{cm}$, allowing the study of short and tall columns with aspect ratios $A \simeq [0.5, 1, 2, 2.8]$ (see Fig. 6.1). A novelty of our study is the releasing mechanism of the granular column, for which we placed an acrylic gate 18 cm wide and 0.8 cm thick at L_0, and covered it with a 0.05 cm thick and 15.24 cm wide PTFE film. One end of the PTFE film

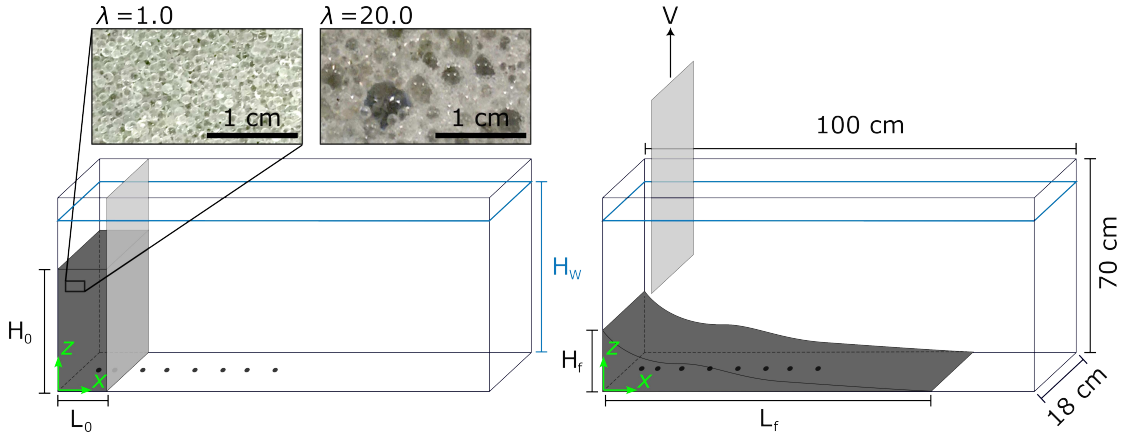

Figure 6.1. Sketch of the column collapse experimental setup. The column initial geometry is the height H_0 and length $L_0 \simeq 8.5$ cm. The column collapses after vertically removing a gate with velocity $V \simeq 0.85$ m/s. At the end of the experiment, the deposit geometry is given by the final height H_f and length L_f. For immersed collapses, the water level is $H_\mathrm{w} \simeq 50$ cm. Dots at the base of the channel represent basal pore pressure transducers PPT placed at $X = [3, 7, 10, 15, 20, 25, 30, 35]$ cm. The close-up lateral views show two tested granular systems with size ratios $\lambda = d_\mathrm{max}/d_\mathrm{min} = 1$ and 20, where d_min and d_max are the minimum and maximum grain diameters, respectively.

was fixed to a roller and the other end, facing the granular column, had displacement restraints. A motor rotated the roller and pulled the PTFE film from one end, removing vertically the gate with a velocity $V \simeq 0.85$ m/s. The lower part of the gate have rounded edges so the PTFE film can slide easier. This mechanism diminishes the effects generated by the relative displacement of the gate and the grains as they are not in direct contact (see FIG. 6.2). In all cases $V > 0.4\sqrt{gH_0}$, meaning that the gate up lift velocity did not influence the column collapse [158].

We studied four values of $\lambda = d_\mathrm{max}/\mathrm{min} = [1.0, 3.8, 12.6, 20.0]$. The samples' grain size distribution (GSD) had a cumulative volume fraction (CVF) that followed a power law (see Eq. (2.2)). For each λ, we chose an exponent $\iota = [1, 1.38, 0.69, 0.47]$, having a common

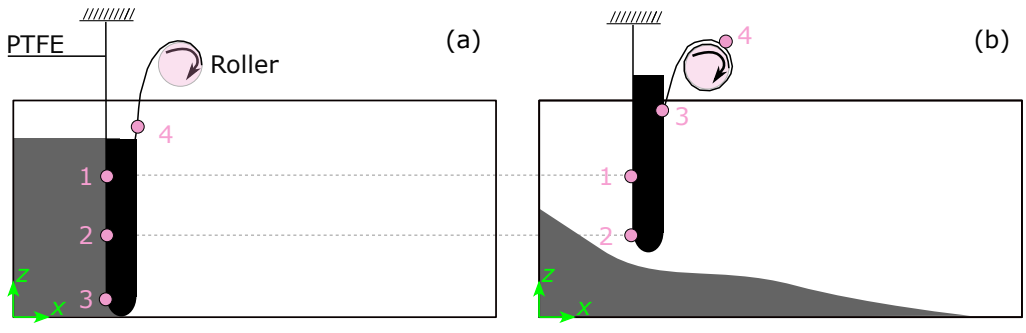

Figure 6.2. Sketch of the gate's releasing mechanism. The gate is covered by a PTFE film that has displacement restraints in one end and is fixed to a roller in the other. A motor makes the roller lift-up the gate, pulling vertically one end of the PTFE film. In this releasing mechanism, the grains and the gate are not in direct contact. (a) and (b) present the releasing mechanism before and after the collapse, respectively. Note that points 1 and 2 do not displace.

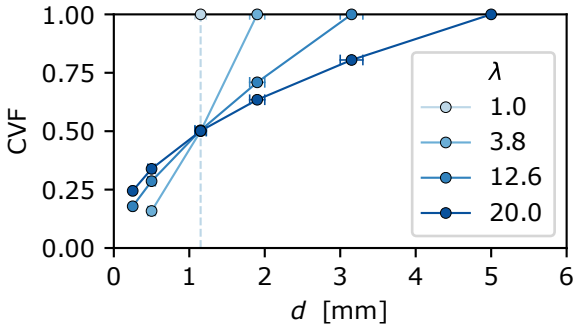

Figure 6.3. Cumulative volume fraction (CVF) as a function of the grain diameter d with a distribution following a power law function (see Eq. (2.2)) with $\iota = [1, 1.38, 0.69, 0.47]$ for the size ratios $\lambda = [1, 3.8, 12.6, 20]$, respectively. All grain size distributions have a common CVF of 0.5 for $d_{50} = 1.15$ mm. Markers are the mean size and horizontal bars represent the range in size reported by the supplier Sigmund Lindner GmbH. The close-up views in Fig. 6.1 show the granular systems with $\lambda = 1$ and 20.

CVF of 0.5 at $d_{50} = 1.15\ \mathrm{mm}$. For these GSDs, the lower ι the greater the concentration of small grains (see Fig. 6.3). We used these GSDs to build samples having an initial packing fraction $\phi_0 \simeq [0.64, 0.68, 0.76, 0.77]$, studying dense columns with ϕ_0 that was comparable to or exceeded the random close packing of monodisperse spheres $\phi_{\mathrm{rcp}} \simeq 0.64$ [15]. We used silica-lime glass beads with density $\rho_{\mathrm{s}} = 2500\ \mathrm{kg/m^3}$ of the type S and M produced by Sigmund Linder GmbH. All GSDs had d_{50} as representative grain diameter and the experiments were not affected by grain-size effects because the ratio L_0/d_{50} was sufficiently large [141]. Considering d_{50} as the characteristic grain diameter d, the immersed and dry granular column collapses are in the inertial and free-fall regime; however, the flow regime of small particles in immersed collapses is in the viscous regime (see Fig. 2.15). The difference of flow regimes might affect the column collapse, enhancing a transition to the viscous side as it was evidenced in the previous Chapter 5.

Besides the initial packing fraction ϕ_0, the bulk specific surface $\mathrm{M_s}$ is another column property that changes with the polydispersity level. For a sphere of diameter d, the specific surface per unit of volume is $M_{\mathrm{s}} = 6/d$, therefore, the smaller the grain the greater the specific surface. We theorised the specific surface of the bulk as the sum of the M_{s} for each grain size times its respective mass fraction in the GSD (see Fig. 6.3). The specific surface in highly polydisperse columns ($\lambda = 20.0$) considerably increases compared with monodisperse columns. For columns with $\lambda = 20.0$, the contribution of the smallest grains to M_s is above the 50%, even when their fraction in the GSD is lower than the 25%. Columns with the polydispersity levels $\lambda = 12.6$ and 20.0 have a similar initial packing fraction $\phi_0 \simeq 0.76$ and 0.77, respectively, but their specific surface M_s is considerably different (see Fig. 6.4). Even if they have a similar ϕ_0, the difference in M_s might play an important role on the column collapse.

We recorded the column collapse with a Motionblitz-cube-4 high speed camera. The experimental setup was backlighted with a LED panel, improving the image contrast and allowing a better recognition of the moving mass. We registered the fluid pressure at the base of the experimental

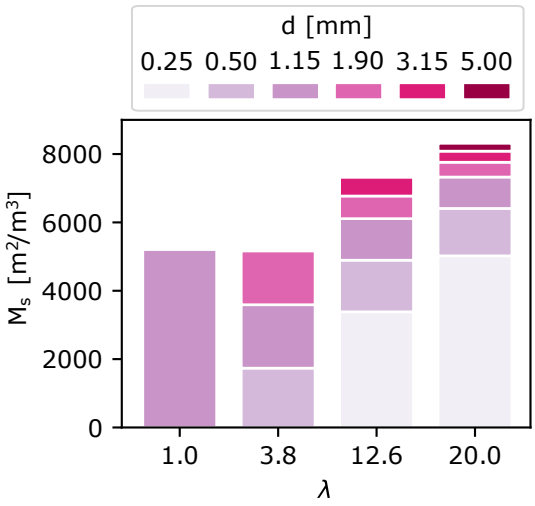

Figure 6.4. Specific surface M_s for all λ discretized by each grain diameter in the GSD. The bulk specific surface was theorise as the sum of each particle size $M_s = 6/d$ times its respective mass fraction in the GSD (see Fig. 6.3).

setup with basal pore pressure transducers PPT placed at $X = [3, 7, 10, 15, 20, 25, 30, 35]$ cm. The PPTs were of the type 26PCCFA6D produced by Honeywell, and they were tested and calibrated for a fluid pressure $P \in [98 - 4900]$ Pa. The camera and the PPTs registered data at 500 Hz, providing a detailed evolution of the collapse and the basal pore fluid pressure.
For diminishing segregation during the construction of the granular column and for having the best possible homogeneous sample, we found satisfactory to hand-mix the grains in a wide bowl and then gently pour the mix in a grid of six rectangles inside the channel. Once the grid was filled, it was pulled up and laid over the grains layer, and then the channel was gently knocked for densifying the sample. This construction process is similar to the one described and tested in section 3.2 (see Fig. 3.2). We repeated this process until reaching the desired H_0. In order to avoid air inside the granular column in immersed experiments, we did the same process with an increasing water level enough to cover the grid.
An experiment started by initiating the PPTs and camera recording. Then, we triggered the releasing gate and let the column collapse by self-weight. When the collapse came to a halt, we directly measured the deposit final runout L_f and height H_f. For immersed experiments, we drained the channel, removed the grains and let them dry during 24 hours in an oven at 100°C. Once the grains were dry, or simply removed from the channel after a dry experiment, we sieved them and prepared them for another experiment. In order to quantify the experiment repeatability, we conducted two repetitions for certain combinations (A, λ) and found consistent results between them*.

*__Short story of the experiments.__ Let's consider a column with aspect ratio $A = 2$ and with polydispersity level $\lambda = 20.0$ in immersed conditions. It was needed around 5 kg of grains with six different sizes. Preparing the mix is nice, you actually enjoy playing with the grains. It takes ~ 25 min. Then, you have to fill the 'fish-tank' with ~4 cm of water, pouring ~4 cm of grains, filling other ~4 cm of water in the fish-tank, and pouring again ~4 cm of grains, and so on. This takes ~ 35 min. Plus ~ 10 min pause. After preparing the column, you must set the camera, the light, the data adquisition system, check that camera and pore pressure transducers (PPTs) record data, and all that takes ~ 15 min. Stand in front the red bottom that triggers

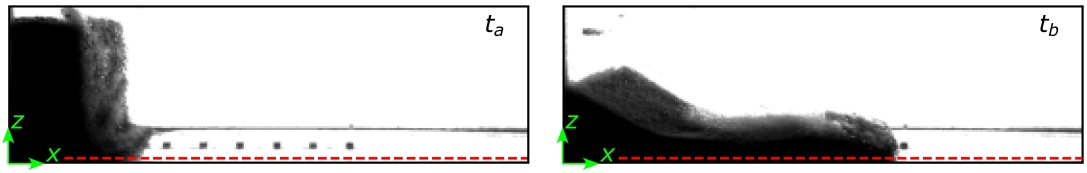

Figure 6.5. Images of the column collapse sequence after correcting the image perspective. The dashed red line indicates the pixel at the base of the column where the temporal analysis is made (see Fig. 6.6 (a))

6.1.2 Digital Image Analysis

From the digital images captured with the high speed camera, we obtained two main results: the evolution of the collapse front position $L(t)$ and the collapse height profile in the (X, Z) plane. First, we guaranteed to identify known lengths in the images. To do so, we first corrected the image perspective with known coordinates that where marked on the experimental setup. The correction of the image perspective was done with the function *'getPerspectiveTransform'* available in OpenCV [180].

Front position

For obtaining the front position evolution, we did a temporal analysis over a pixel line at the base of the column image (see Fig. 6.5), identifying a Black zone of pixels with a color code $(R, G, B) = (0, 0, 0)$ that transit through a Gray zone, and finishes at a white zone white $(R, G, B) = (1, 1, 1)$ (see Fig. 6.6 (a)). At the beginning of the temporal analysis t_0, the Black zone well captures the initial position of the column L_0. On the contrary, at the end of the temporal analysis t_f, the position of the final runout L_f is better captured by the Gray zone. For pixels near L_f at the end of the collapse sequence, the Black zone is noisy and has a discrepancy with the real L_f because the amount of grains is not enough to produce a dark contrast with $(R, G, B) = (0, 0, 0)$. For obtaining the front position evolution $L(t)$, we first identify the evolution of the Black pixels $L^B(t)$ and the evolution of the Gray pixels $L^G(t)$. Then, we weighted these two with the exponential functions $f^B(t) = 1 - 1/(1 + e^t)$ with domain $D = [1, 0]$, for the Black pixels, and $f^G(t) = 1/(1 + e^t)$ with $D = [0, 1]$, for

the experiment and think twice to be sure that you have not forgotten any tiny thing takes ~ 2 min. Closing your eyes, taking a deep breath, pushing the red bottom, doing the experiment, stopping the recording of the camera and PPTs takes ~ 0.2 min. Take manually the measurements of the final runout and height and drain the fish-tank takes ~ 25 min. Vacuum the grains from the fish-tank and place them in the oven takes ~ 30 min. Next day, you sieve the grains. It sounds easy, and it is easy, but takes time, too much time. The gap between one grain diameter and another is not huge, and you must consider that grains have a small variability. You must choose the right sieves for your grains. Sieving takes too much time because the sieves 'saturate' and you must brush the sieve to remove grains, otherwise the separation does not continue. That is why you can not use a sieving machine, it does not brush for you. Also because it is too violent with your grains and little by little you would be changing the friction coefficient. Believe it or not, sieving could take an entire day. As a rule of thumb, I knew that sieving 1 kg would take me ~ 75 min. You do by yourself the maths for 5 kg. Next day you do another experiment, hoping that you have not lost too many grains the days before.

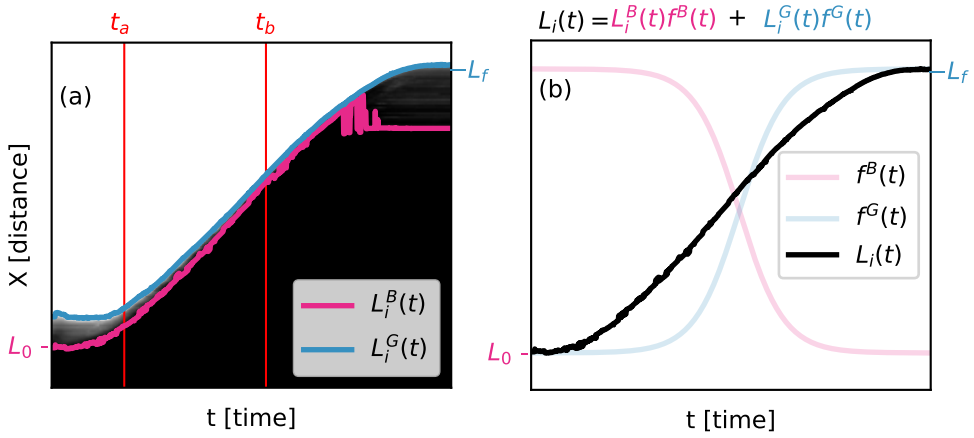

Figure 6.6. (a) Temporal analysis for a pixel line recognising the boundaries of Black and Gray zones. t_a and t_b correspond to the images presented in Fig. 6.5. (b) Front position evolution $L(t) = L^{\mathrm{B}}(t)f^{\mathrm{B}}(t) + L^{\mathrm{G}}(t)f^{\mathrm{G}}(t)$, where $f^{\mathrm{G}}(t) = 1/(1+e^t)$ with a domain $D = [0, 1]$ and $f^{\mathrm{B}}(t) = 1 - f^{\mathrm{G}}(t)$ with $D = [1, 0]$.

the Gray pixels, and obtained the front position as

$$L(t) = L_{\mathrm{i}}^{\mathrm{B}}(t)f^{\mathrm{B}}(t) + L_{\mathrm{i}}^{\mathrm{G}}(t)f^{\mathrm{G}}(t), \tag{6.1}$$

having a $L(t)$ that starts in L_0 and finishes in L_{f} (see Fig. 6.6 (b)).

Height Profiles

For obtaining the collapse profile we found satisfactory to threshold the image inset of identifying black, gray and black pixels. We used the function *'adaptiveThreshold'* available in OpenCV [180] that, in our case, helped us to identify the contour of the column while it collapsed. We assumed this contour as the height profiles of the column collapse (see Fig. 6.7).

6.1.3 Signal processing

With the PPTs, we registered the fluid pore pressure P at the base of the collapse and filtered the registered signal for obtaining a measure of P without, or with reduce, noise. In order to do so, we first got rid of the signal noise doing a moving average

$$P^{ma}(t_i) = \frac{1}{2m+1}\sum_{i-m}^{i+m} P^r(t_i) \tag{6.2}$$

with $m = 15$. Then, to the cleaned signal $P^{ma}(t)$, we apply a Butterworth lowpass filter of order 5 to obtain a signal without the dominant frequency of the PPT instrument. We used the funciton '*butter_bandpass*' available in library SciPy [181]. The signal obtained after applying the Butterworth lowpass filter to $P^{ma}(t)$ is the one that we consider as the fluid pressure evolution $P(t)$. Fig. 6.8 (a) presents the Fourier Transformation in the frequency domain for the signal $P^{ma}(t)$ and shows the applied frequency filter.

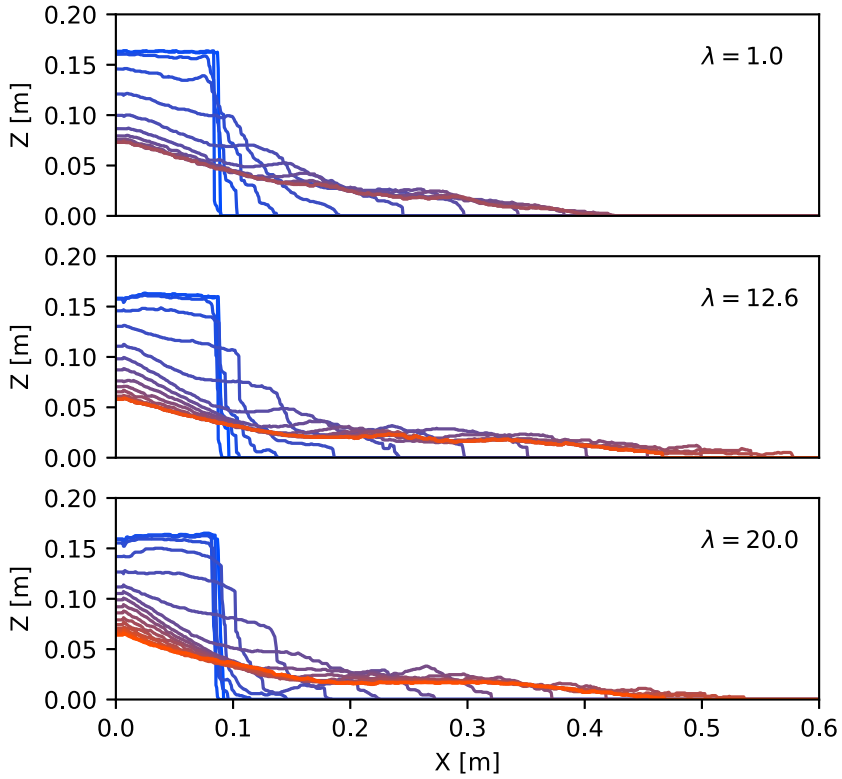

Figure 6.7. Collapse profile evolution for immersed columns with $A \simeq 2$ and for the polydispersity levels $\lambda = 1.0, 12.6$ and 20.0. The time gap between each line is 0.12 s.

The analysis of the evolution of the pore pressured was done with the changes of the pore pressure monitored as

$$\Delta P(t) = P(t) - P_0 \tag{6.3}$$

during the column collapse, with $P_0 = \rho_w g H_w$ being the initial fluid hydrostatic, where $P_0 = \rho_w g H_w$ is the initial hydrostatic pressure. Fig. 6.8 (b) compares the pore pressure changes with the raw signal ΔP^r, the signal after applying the moving average ΔP^{ma}, and the signal after applying the Butterworth lowpass filter ΔP.

6.2 | Collapse sequence

After removing the gate, the column starts to collapse, releasing a wedge of grains that moves vertically and then spreads horizontally. For dry columns, polydispersity plays a minor role on the collapse sequence. The mobilised mass of monodisperse and polydisperse columns have similar heights and reach similar horizontal distances almost at the same time (see (a) and (b) in Fig. 6.9). For immersed cases, the first stage of the column collapse reveals differences between monodisperse and polydisperse columns, showing that systems with $\lambda = 1$ collapse faster than systems with $\lambda = 20$ (see (c) and (d) in Fig. 6.9). An important remark of polydisperse columns is the initial vertical fall of grains at the column releasing face, while the core remains still. High packing fractions, due to high polydispersity levels, frustrate the rapid percolation of water into the granular structure and produce a retrogressive collapse mechanism.

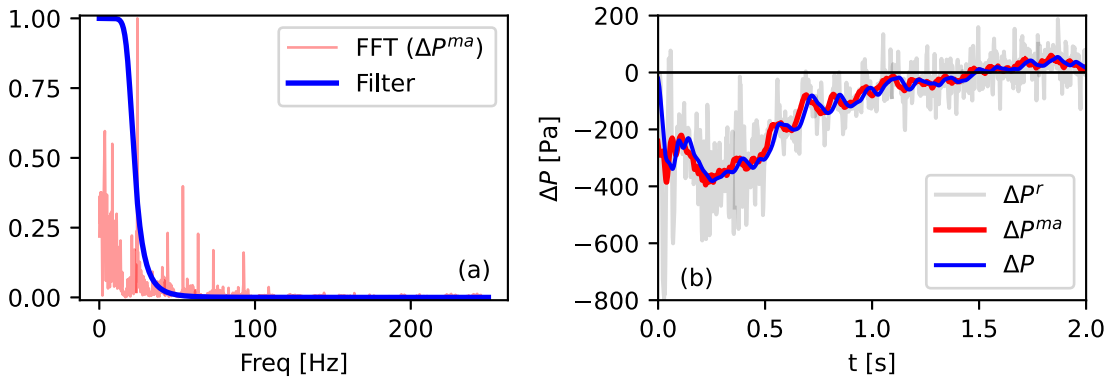

Figure 6.8. (a) Normalized Fourier transfor FFT of the pore pressure changes after doing the moving average ΔP^{ma}. The blue curve shows the Butterworth lowpass filter used to get rid of the instrument's dominant frequency. (b) Evolution of the pore pressure changes for the raw data ΔP^r; for the data after the moving average ΔP^{ma}; and for the data after filtering. This latter is considered as the pore pressure evolution ΔP used in this work.

Similar collapse mechanisms have been observed for sand columns [178] and polydisperse columns in two-dimensional simulations [172]. The motion of monodisperse collapses finishes earlier than that of polydisperse collapses, resulting in longer runout distances for systems with $\lambda = 20$ than for $\lambda = 1$. The final deposits of immersed collapses have a wavy shape that is produced by strong grain-fluid interactions on the surface of the moving mass. On the contrary, due to the negligible air viscosity, the deposits of dry collapses have a smooth surface. The collapse sequence in Fig. 6.9 presents the collapse evolution at equivalent moments for a time scale normalised by a characteristic time $t^* = \sqrt{H_0/g^*}$, where $g^* = g\Delta\rho/\rho_s$ is a scaled gravity due to the ambient fluid with $\Delta\rho = \rho_s - \rho_f$ being the difference between the solids and fluid densities and $g = 9.81\ \mathrm{m/s^2}$ the gravity acceleration.
From the recorder digital images, we obtained the profile of the moving mass and the evolution of the front position $L(t)$ (see section 6.1.2). This last provided information on the front propagation and its characteristic velocity U in the horizontal spreading stage. We found that U was nearly constant between the instants when the front had reached $L_{25} = L_0 + 0.25(L_f - L_0)$ and $L_{75} = L_0 + 0.75(L_f - L_0)$, and we computed the front velocity as $U = (L_{75} - L_{25})/(t_{75} - t_{25})$ with t_{25} and t_{75} being the time at which the front arrives to L_{25} and L_{75}, respectively. The information of $L(t)$ and $\Delta P(t)$ allow us to link the effect that one has on the other during the collapse sequence (see Fig. 6.10). This link is presented in section 6.3.

6.2.1 Polydispersity role

The evolution of the front position for dry collapses evidences that increasing the level of polydispersity has a minor effect on the collapse sequence. Regardless of their polydispersity level, collapses do not exhibit notable differences neither at the collapse initiation nor during the spreading stage. The front position of dry collapses reach similar distances at similar times, revealing the flow independence to the GSD during the constant shearing of the moving mass. At the end of the collapse, the final runout vaguely varies with polydispersity, and for

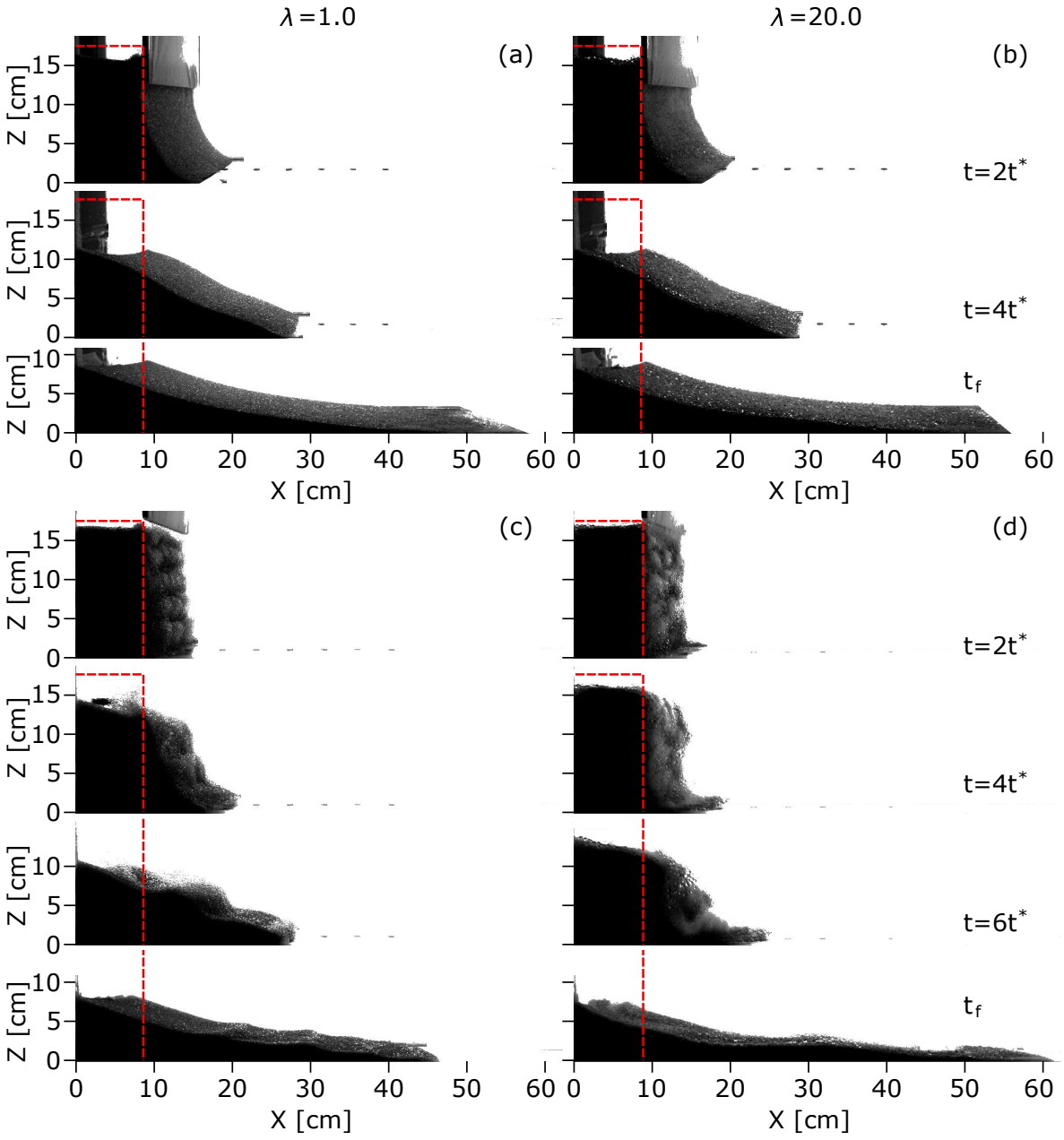

Figure 6.9. Collapse sequence of (a, b) dry and (c, d) immersed columns with aspect ratio $A = H_0/L_0 \simeq 2$, and (left) $\lambda = 1$ and (right) 20. The red dashed lines indicate the column initial geometry. $t^* = \sqrt{H_0/g^*}$ is a characteristic column time, where $g^* = g\Delta\rho/\rho_s$ is a scaled gravity due to the ambient fluid and $\Delta\rho = \rho_s - \rho_f$ is the difference between the solids ρ_s and fluid ρ_f densities.

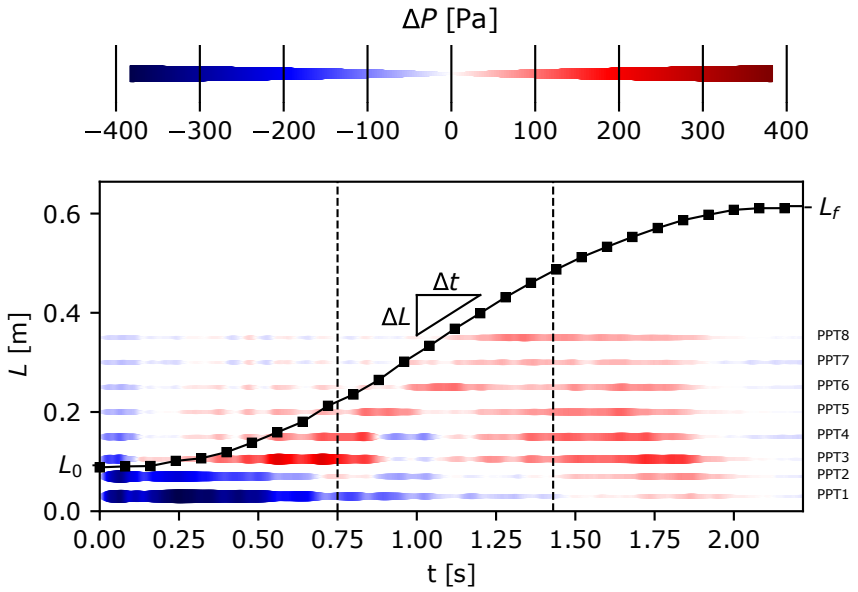

Figure 6.10. Evolution of the front position L_i and fluid pressure change ΔP for a column with $A \simeq 2.0$ and $\lambda = 20.0$. The fluid pressure change is computed as $\Delta P(t) = P(t) - P_0$ where $P(t)$ is the pressure registered by the pore pressure transducers PPTs and P_0 is the initial fluid hydrostatic pressure. Note that only PPT 1 and 2 are beneath the column initial geometry. The dashed lines indicate the instants when the collapse reaches $L_{25} = 0.25(L_f - L_0) + L_0$ and $L_{75} = 0.75(L_f - L_0) + L_0$, and delimit the collapse steady propagation stage interval where the front velocity U is computed.

tall columns the mobility tends to increase with λ (see $L(t)$ for dry collapses in Fig. 6.11). On the contrary, the collapse sequence of immersed columns depends on the polydispersity level. Notably, polydispersity affects the collapse initiation and the final runout. The horizontal spreading of highly polydisperse collapses is delayed, having a front position evolution with a time gap of about $0.9\ t^*$ compared with that of less polydisperse systems. Having a delay in the collapse sequence can also be linked with increasing ϕ as suggested by Pailha *et al.* [142] and Pailha & Pouliquen [143]. Interestingly, in our experiments we only observe that the collapse is delayed up to the greatest polydispersity level ($\lambda = 20$), indicating that immersed flows in the inertial regime are not as sensitive to ϕ as flows in the viscous regime (see $L(t)$ for immersed collapses in Fig. 6.11).

Once the collapses transition to the horizontal spreading stage, all systems with a similar aspect ratio exhibit an alike collapse velocity, having $L(t)$ with nearly aligned trends (see Fig. 6.11). Immersed polydisperse columns exhibit a prolonged phase of continuous spreading, which leads to collapses with greater runout distances compared to monodisperse systems. This effect is amplified in tall columns. The characteristic velocity U augments with A and is closely related with the theoretical free-fall velocity $U_{\mathrm{ff}} = \sqrt{2g^* A L_0}$, showing a good agreement when U_{ff} is scaled by a factor 0.5 and 0.28 for dry and immersed collapses, respectively. The similar between U/U_{ff} correlation was observed in previous works [133, 160], and also evidenced and discussed in the previous chapter (see section 5.3). Moreover, U has more variability in dry

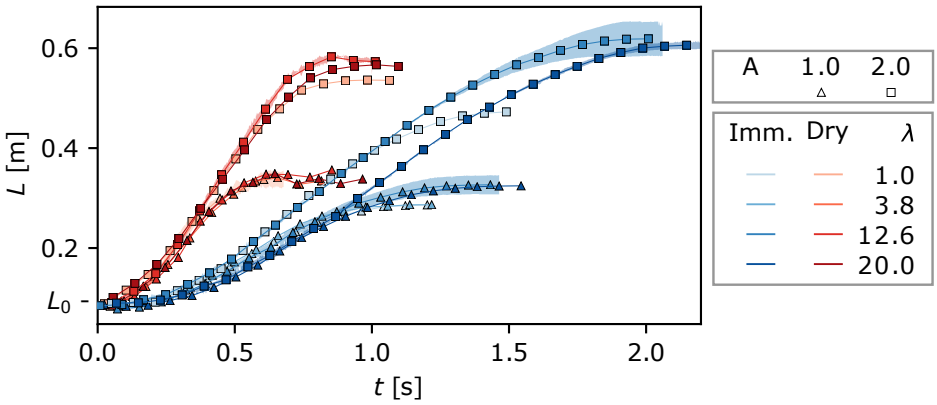

Figure 6.11. Front position evolution $L(t)$ for (reds) dry and (blues) immersed columns, and for ($\triangle$) $A \simeq 1$ and ($\square$) $A \simeq 2$. Shaded areas represent the variability between repetitions with envelopes indicating the minimum and maximum values, and markers and continuous line are the average of them.

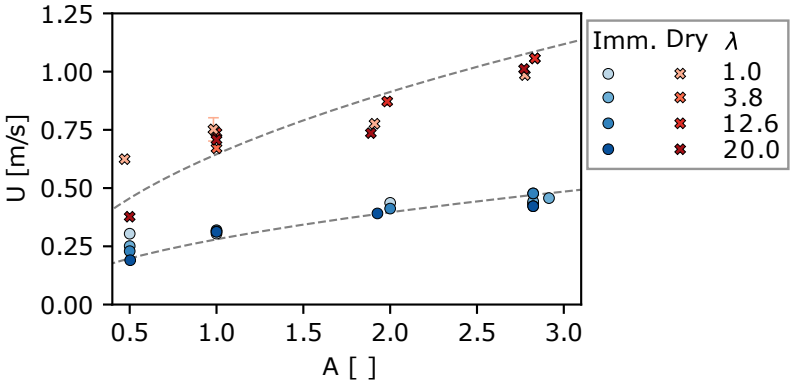

Figure 6.12. Front velocity U during the steady propagation stage as a function of A for all λ, and for (reds) dry and (blues) immersed columns. The interval where U is computed is shown in Fig. 6.10. The dashed lines indicate the theoretical free-fall velocity $U_{\text{ff}} = \sqrt{2g^* A L_0}$ scaled by a factor 0.50 and 0.28 for dry and immersed columns, respectively. Error bars indicate variability between repetitions.

collapses than in immersed collapses and, for the latter, U is marginally affected by λ with a slight reduction for $\lambda = 20$ (see Fig. 6.12).

6.2.2 Runout

The mobility of a granular column increases with the aspect ratio A and has been normally seen to follows a power law function (see Eq. (2.22)). Our results can be fitted by the coefficients $(a, b) = (2.7, 1)$ for short columns and $(a, b) = (3.7, 0.64)$ for tall columns, similar to those found by Bougouin & Lacaze [133]. For immersed columns, polydispersity enhances the column mobility and L^* deviates from the trend (see Fig. 6.13 (a)). Interestingly, for short columns ($A < 2$), L^* is slightly higher for dry collapses than for immersed ones, and it seems intuitive because the viscous force contrary to the motion of grains exerts an additional resistance. For immersed tall columns ($A \geq 2$), polydispersity boosts the column mobility, resulting in final deposits with a longer runout distance when compared with dry columns.

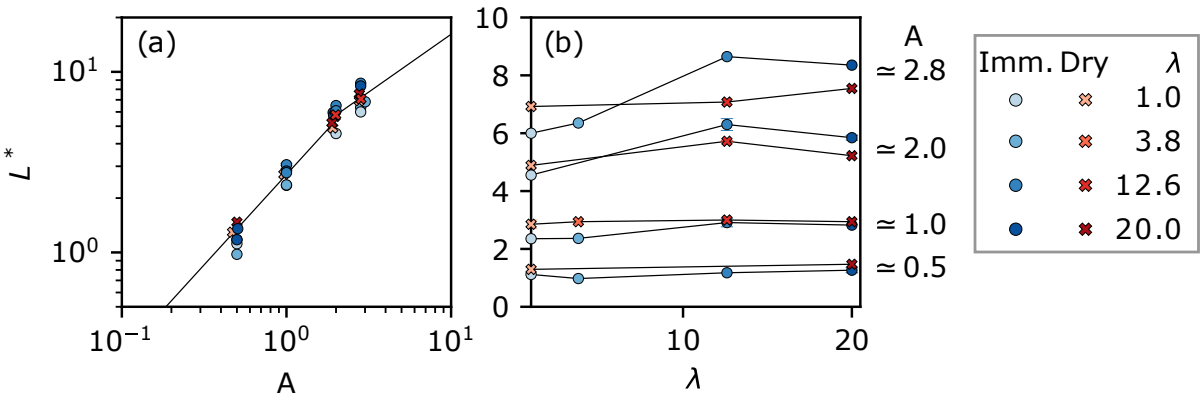

Figure 6.13. Normalized final runout $L^* = (L_f - L_0)/L_0$ as a function (a) A and (b) λ. The lines in (a) indicate $L^* = aA^b$ with the values $(a, b) = (2.7, 1.0)$ for short columns $(A < 2)$ and $(a, b) = (3.7, 0.64)$ for tall columns $(A \geq 2)$. Error bars indicate variability between repetitions.

For the sake of simplicity, we compare the runout for the extreme polydispersity levels $\lambda = 1$ and 20. Our findings indicate that polydispersity leads to a roughly 7% increase in mobility for dry columns. In the case of immersed short columns, despite having lower runout than dry columns, polydispersity enhances their mobility by up to 20%. Moreover, tall columns experience a significant boost in mobility, showing an increase of 38% (see Fig. 6.13 (b)).
In our experiments, we do not evidence segregation at the deposit, neither in dry columns nor in immersed columns. Therefore, we cannot attribute to segregation the reason for the increasing runout in highly polydisperse columns, especially for immersed cases. However, we can link the collapse sequence to changes on the basal pore pressure, thanks to our experimental setup and instrumentation (see Fig. 6.10). In the following subsection, we discuss the relationship between varying levels of polydispersity in immersed collapses and changes in the basal fluid pressure.

6.3 | Basal pore fluid

We found that there is a link between the evolution of the pore fluid pressure and the collapse sequence, and vice-versa. By observing the evolution of the front position, it is possible to demarcate three moments of basal pore pressure changes ΔP (see Fig. 6.10). Firstly, beneath the column initial geometry (i.e., for PPT 1 and PPT 2) the pore pressure decreases. It can be assumed that a decrease in pore pressure induces a fluid flow into the granular structure as the dense granular column dilates, resulting in a temporary increase of the effective stress σ' [9, 86]. During this first moment, the PPTs outside the column initial geometry $(X > L_0)$ do not record significant pressure changes. Secondly, during the horizontal spreading stage, the depositing of the moving mass and the reduction of the voids volume produce a exceeding pore pressure that stands for a fluidized flow without shear strength where grains may collide with the base but remain suspended [182]. Note in Fig. 6.10 that the amplitude of the ΔP augments after the granular front arrives at any of the PPT positions. The last moment is

characterized by a full dissipation of the excess pore pressure, i.e., $\Delta P \simeq 0$, that coincides with the front reaching L_{f}.

Let's now compare the effect that λ and A have on the first two moments of ΔP. At the collapse initiation, when the pore pressure changes beneath the column are negative, the amplitude of ΔP increases with λ and A, meaning that more fluid needs to enter into the dilating granular structure because λ makes denser systems and A augments the column H_0. This result is in agreement with Ahmed *et al.* [22] who show that highly polydisperse systems develop a greater magnitude of negative pore pressure changes, indicating their tendency to dilate when deforming. Notably, ΔP remains negative with a greater amplitude and for a longer period for $\lambda = 20$ than for other polydispersity levels, indicating that the fluid flow through the moving mass takes more time (see columns PPT1 and PPT2 in Fig. 6.14). The flow of a fluid through a porous media, as the columns collapse, can be interpreted as the flow through a network of interconnected pipes controlled by the material hydraulic permeability k. The lower k the slower the flow through the column. The permeability depends on ϕ and the solids specific surface M_{s}, and it decreases with an increase of any of the above [183]. Among our experiments, columns with $\lambda = 20$ have the highest ϕ_0 and the highest M_s (see Fig. 6.4) and, consequently, the lowest k, hindering the fluid percolation through the granular structure. This fact explains that in highly polydisperse columns the negative change of pore pressure ΔP lasts for a longer period, leading to a slower collapse initiation when compared with columns with lower polydispersity levels (see Fig. 6.11).

During the second moment of the pore pressure changes ΔP, the grains collective movement and the associated voids reduction induce positive pore pressure changes. The peak positive ΔP is recordered close to the column initial length and augments for tall columns (see column PPT 3 in Fig. 6.14). The strong positive change of P in the early stages of the collapse recalls the pore pressure in debris flows that approach, or in some cases exceed, the necessary pressure to liquefy the moving mass [10]. A closer look to ΔP reveals that polydispersity has a strong influence on the pore pressure change when the collapse front arrives at the PPTs position. For systems with low ϕ_0, like in $\lambda = 1$, the pore pressure change has a positive peak that rapidly vanishes to $\Delta P \approx 0$. In contrast, when the system has high ϕ_0 and low permeability, like in $\lambda = 20$, the excess pore pressure dissipation takes longer, because the large grains' concentration induces greater drag and reduces the depositing velocity [101], producing a localised fluidisation at the base. Fig. 6.15 presents the ratio between ΔP obtained for a 0.25 s interval after the front arrives to each PPT position and the equivalent effective stress σ'. We estimated $\sigma' = \phi_0 \rho_{\mathrm{p}} g h_{\mathrm{i}}$, where h_{i} is the average collapse height at PPTi for the same 0.25 s interval obtained from the image analysis.

Comparing two systems with extreme polydispersity level $\lambda = [1, 20]$, the differences on the collapse sequence can be attributed to differences on the evolution of the basal pore pressures. For highly polydisperse systems, positive pore pressure changes reduce σ' for a longer period, allowing the moving mass to flow with constant velocity during more time and, hence, resulting in longer runout distances than in monodisperse systems (see Fig. 6.11 and Fig. 6.13). This observation is similar to processes observed in geophysical flows, where the excess pore pressure

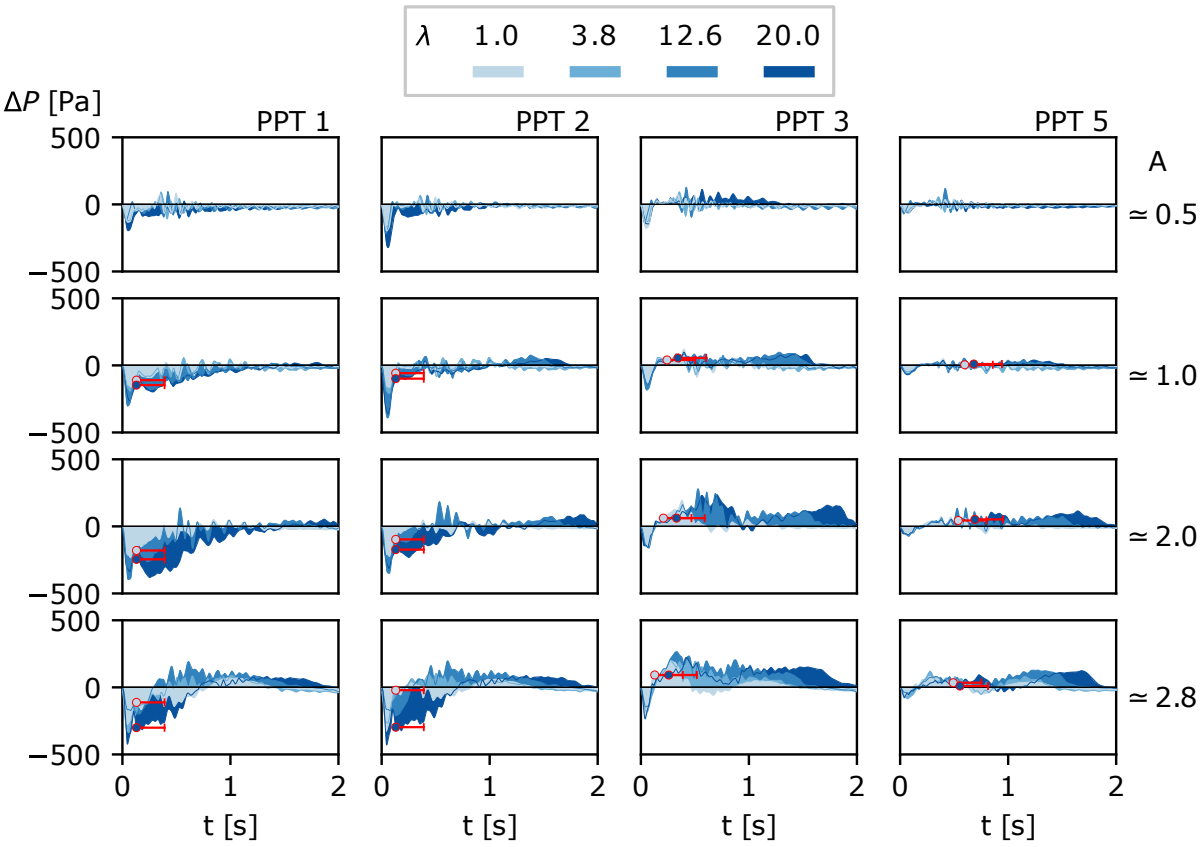

Figure 6.14. Evolution of ΔP for the PPTs 1, 2, 3 and 5 (columns), for columns with $A \simeq [0.5, 1, 2, 2.8]$ (rows) and for all λ. Markers indicate ΔP at the time when the front reaches the PPT_i position for $\lambda = [1, 20]$ and the horizontal red bar indicates a range of 0.25 s. For PPT 1 and 2, both beneath the column initial geometry, the horizontal bars indicate the time interval $t = [0.125 - 0.375]$.

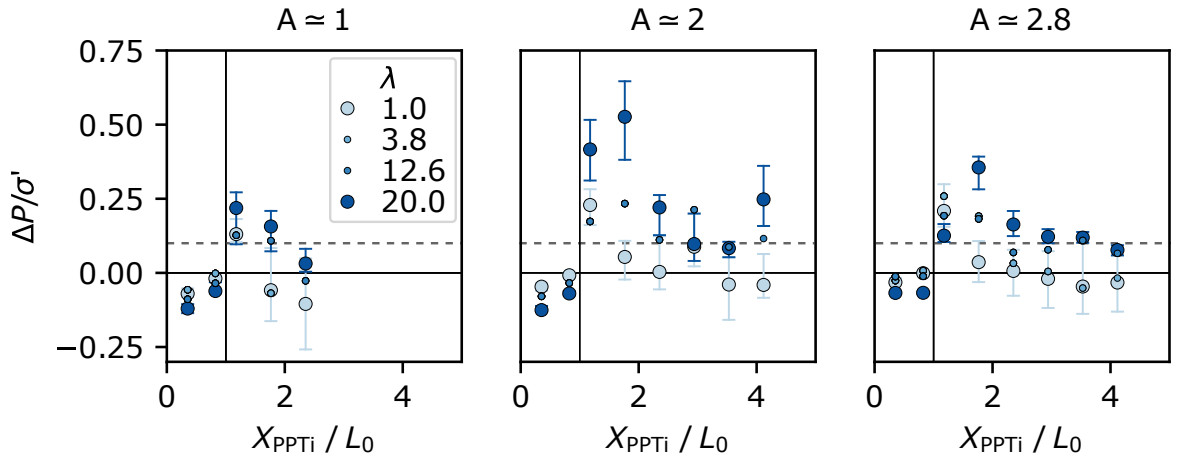

Figure 6.15. Ratio between the basal pore pressure changes ΔP and the effective stress σ' when the flow front arrives to the position X_{PPTi} for all λ and for columns with $A \simeq [1, 2, 2.8]$. ΔP was considered as the median value of a 0.25 s interval after the front arrives to X_{PPTi}, and the error bars indicate the first and third quartile of the same interval. $\sigma' = \phi_0 \rho_{\mathrm{p}} g h_{\mathrm{i}}$ is computed with the average flow height h_i for the same time interval. For for PPTs 1 and 2, both beneath the column initial geometry, ΔP was considered for the time interval $t = [0.125 - 0.375]$ s (see markers in Fig. 6.14). The dashed lines indicate $\Delta P/\sigma' = 0.1$.

is responsible for producing partial fluidization, reducing the effective friction and resulting in long runout distances [146, 147]. Our results indicate that, when ΔP increases to around 10% of σ', collapses can have a prolonged period of constant spreading (see Fig. 6.15). An interesting observation arises when comparing ΔP for systems with $\lambda = 12.6$ and 20, that have $\phi_0 \simeq 0.76$ and $\phi_0 \simeq 0.77$, respectively. For these two polydispersity levels, the changes of the basal pore pressure show a similar tendency with $\Delta P/\sigma' \gtrsim 0.1$ beyond the column initial length. These systems also have the greatest mobility. This result suggests that immersed polydisperse granular flows might be better described by an initial packing fraction ϕ_0 rather than by a characteristic grain diameter d.

6.4 | Conclusions

We conducted an experimental study of dry and immersed dense granular column collapses. We varied the column height, ranging from short to tall columns, as well as the columns' grain size distribution from monodisperse to highly polydisperse systems, in order to assess the effect of the grain size distribution on the column collapse. The collapse sequence was analysed by means of digital image analysis and direct measurements on the basal pore fluid pressures, providing unique insight into the coupled kinematics of grains and fluid until coming to rest.
We showed that the level of polydispersity has a stronger effect on immersed columns than on dry columns. For dry columns, the collapse sequence remains independent of the polydispsersity level, reaching similar distances at similar times. This observation is common for short and tall columns. The final runout of dry columns vaguely increases with the polydispersity level, enlarging the mobility in approximately 7%. In immersed columns, an increase on the polydispersity level plays an important role, most notably on the collapse initiation and on the runout distance. We evidenced that variations of these two features are caused by differences in the evolution of the pore pressures inside the moving mass. When the column starts to collapse there is a negative change of the pore pressure that provokes a temporally increase of the column's strength. We showed that the collapse of polydisperse columns is delayed because the negative change of pore pressure has a greater amplitude and remains for a longer period than in monodisperse columns. During the horizontal spreading stage of immersed collapses, the grain's deposition expels fluid from the moving mass and produces an excess, same as a positive change, of the pore pressure. We revealed that in monodisperse flows the excess of pore pressure is rapidly dissipated, while for polydisperse flows the excess of pore pressure remains for a longer period, decreasing the strength and producing a localised fluidisation that results in longer runout distances. Our findings indicate that, when the basal pore pressure increases to around 10% of the effective stress, granular flows can hold for a prolonged period a constant spreading rate. Due to the exceeding pore pressure, the mobility of short and tall columns increases up to 20% and 38%, respectively.
Previous studies focusing on monodisperse systems have already highlighted the importance of packing fraction in the behaviour of granular flows in fluids with high viscosity (e.g., oil or water-oil mixtures), but none have demonstrated its influence in immersed flows within

a fluid of low viscosity (e.g., water or, in the extreme case, air). In polydisperse systems, the influence of packing fraction and hydraulic conductivity becomes so pronounced that we have demonstrated their impact on the basal pore pressure changes in granular flows immersed in water. Our results indicate that characterising polydisperse granular flows in immersed conditions depends on a characteristic diameter, but more importantly, it relies on the material's packing fraction and permeability.

The findings of this work shed light on the effect that increasing polydispersity has on granular flows and evidence that immersed flows strongly depend on the polydispersity level. Our results suggest that the packing fraction might be a better descriptor than a characteristic diameter in polydisperse granular flows. Our experimental work provides a novel insight of the basal pore pressure variations and the influence that it has on the collapse sequence of immersed granular flows. Further studies might enrich the understanding of these complex systems exploring into other details such as the effect that cohesive granular contacts, grains with varying density, or grain shape have on immersed flows.

CHAPTER 7

The Unified Runout Description

This chapter is partially based on the paper *Collapse of dry and immersed polydisperse granular columns: A unified runout description* by Oscar Polanía, Miguel Cabrera, Mathieu Renouf, and Emilien Azéma published on August 22nd 2022 in Physical Review Fluids **7**, 084304 [172] and the paper *Polydispersity effect on dry and immersed granular collapses: An experimental study* by Oscar Polanía, Nicolas Estrada, Emilien Azéma, Mathieu Renouf, and Miguel Cabrera.

The results presented in this chapter come from the simulation and experimental campaign of Chapter 5 and Chapter 6, respectively. Moreover, we have strengthen the discussion with the results of *Granular collapse in a fluid: Different flow regimes for an initially dense-packing* of 2018 published in Physical Review Fluids by Bougouin & Lacaze [133] and *Underwater collapse of a loosely packed granular column on an inclined plane: Effects of the Darcy number* of 2019 published in AIP Advances by Lee [127] that the authors have kindly shared with us, and the results interpreted from the published papers of Lajeunesse *et al.* [123], Yang *et al.* [159], and Sun *et al.* [160]

Resume

Mobility models are a simple, but functional, way to estimate the mobility of granular flows. They provide a simplified interpretation of a complex process and link certain initial and flow conditions with the final runout. In this study, we test a mobility model that links the column final runout and the collapse kinetic energy, initially proposed for polydisperse granular column collapses in two-dimensions (see Chapter 5), with the experimental results of polydisperse granular columns (see Chapter 6), and the results of other authors. Moreover, relying on previous results, we extend the relationship between energy and runout, and propose a model that predicts the runout of granular columns, suggesting that it might be an universal scaling.

7.1 | Model Considerations

In Chapter 5, we proposed a mobility model that links the runout of a granular column L^* with the collapse kinetic energy E_K^U developed during the steady propagation stage (see section 5.5). This model was conceived with the analogy of a block of mass M that slides over a horizontal plane with steady velocity U. By assessing the controlling factors within the model, we found the collapse energy E_K^U as the foremost parameter for establishing a proportionality

between the flow condition and the column final runout. This model satisfactorily works for several polydispersity levels, and for both dry and immersed granular column collapses (see Eq. (5.6) and Fig. 5.9).

In the proportionality proposed in Chapter 5, we neglected the initial column length L_0 because all column simulations had the same L_0. Now, for applying this model to all columns column collapses with different initial geometries, we refer to the model as the proportionality given by

$$L^* \propto \frac{1}{L_0}\frac{\rho_s}{\Delta\rho}\sqrt{E_K^U} \tag{7.1}$$

where $E_K^U = MU^2/2$ is the collapse kinetic energy during the horizontal propagation stage and $M = L_0 H_0 \phi_0 \rho_s = L_0^2 A \phi_0 \rho_s$ is the column mass. M is considered as a mass of unitary width because the column collapse experiment is a width independent problem.

7.2 | The Mobility Model as a Common Trend

The scaling proposed in Eq. (7.1) collapses on a common trend of results coming from the numerical simulations and experiments for different polydispersity levels, and for dry and immersed columns. The scaling shows an slight distinction between dry and immersed experiments because these lasts, and specifically those with high polydispersity level, are influenced by the effect of positive pore pressure, resulting in longer L^* (see section 6.3). Despite the distinction of immersed and dry polydisperse experiments, it is outstanding that this formulation relates the energy and mobility of granular columns of results coming from simulations and experiments. Although polydispersity is not explicit in the model formulation, the initial packing fraction ϕ_0, that depends on it, is indispensable for obtaining the front kinetic energy because it affects the column mass M. Fig. 7.1 (a) presents the scaling of the normalised final runout L^* with the column kinetics according to Eq. (7.1) for the results of the column collapses of Chapter 5 and 6.

We consider that this scaling provides a good correlation between the column mobility L^* and the energy E_K^U. Fig. 7.1 (b) presents the scaling of Eq. (7.1) with our results, and the experimental results of Lajeunesse *et al.* [123] and Bougouin & Lacaze [133] who worked with glass beads; the experimental results of Lee [127] who worked with sand and inclined planes; the numerical results of Yang *et al.* [159] who worked in a couple DEM-Lattice Boltzmann Method (fine fluid solution); and the numerical results of Sun *et al.* [160] who worked with a couple DEM-CFM in a coarse graining approach. The majority of the data from these authors collapse on the same trend, indicating, once again, that there is a good proportionality between the L^* and E_K^U. Nevertheless, there are some results that detach from the trend. For those results from the work of Yang *et al.* [159] that deviate from the trend, one could interpret that the points deviating are collapses that reach a longer runout distance because those are collapses in inclined planes. For the others, the strong grain-fluid interactions might influence. Therefore, we will use the flow regime, which is a way to classify flows considering

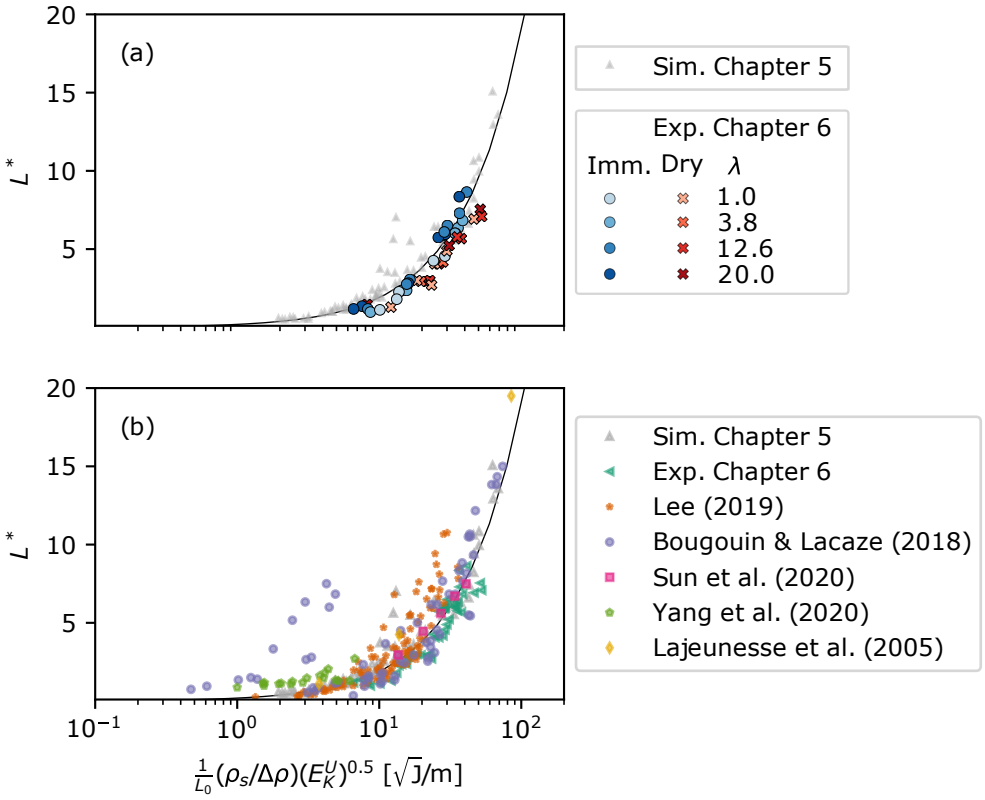

Figure 7.1. Scaling between the collapse energy E_K^U and the normalised runout L^* given by the mobility model proposed in Eq. (7.1) for: (a) the simulations presented in Chapter 5 and the experiments presented in Chapter 6, indicating the polydispersity level λ of immersed and dry column collapses; and (b) the results of this thesis, the numerical results of Yang *et al.* [159] and Sun *et al.* [160], and the experimental results of Lajeunesse *et al.* [123], Lee [127], and Bougouin & Lacaze [133]. The black line is the best fit linear fit with slope 0.19.

the grain-fluid interactions (see section 2.3), for distinguish each collapse and determining if it limits the scaling between energy and mobility.

The flow regime classification relies on fluid and grain properties, and notably depends on a characteristic diameter d. For polydisperse flows, the characteristic diameter d is a dimension difficult to interpret, and the Stokes number could vary in a range delimited by the smallest and biggest grain (see Eq. 2.12 and Fig. 2.15). In Chapter 4, we evidenced, at least for dry flows, that the diameter d_{50}, that holds the 50% of the sample's mass, can well characterises the flow for a wide range of inertial levels. Therefore, for now on, we will use d_{50} for classifying flows. Moreover, in Chapter 5, we observed that an increase in polydispersity, representing also an increase of the packing fraction ϕ_0, strongly varies the collapse behaviour of tall columns, reducing the flow velocity U and implying a regime transition from inertial to viscous (see Fig. 5.4). A similar observation for monodisperse columns was done by Rondon *et al.* [9] who evidenced changes in the collapse dynamic when the column packing was increase from loose to dense (see Fig. 2.11). These remarks suggest that the packing fraction ϕ_0 could be considered as one of the state variables for classifying the flow regime. Consequently, in order to account for the polydispersity effect, we will use the grain diameter d_{50} weighed by

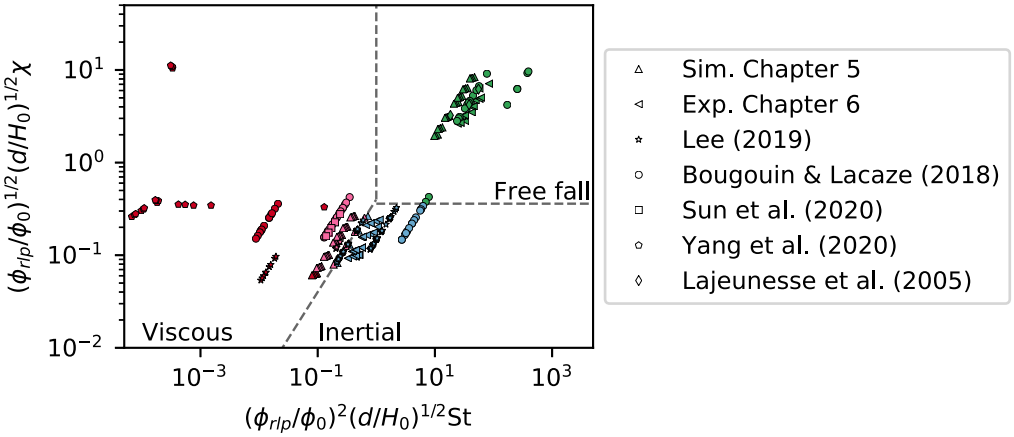

Figure 7.2. Parametric space (St, χ) proposed by Courrech du Pont *et al.* [79] with both axis scaled by $(d/H_0)^2$ and with dashed lines delimiting the transition between regimes as proposed by Bougouin & Lacaze [133]. The characteristic diameter d was considered as d_{50} weighted by the ratio between the random loose packing ϕ_{rlp} and the initial column packing fraction ϕ_0, resulting in a axes multiplied by $\phi_{\mathrm{rlp}}/\phi_0$ with different power indexes. The markers' colour indicates free-fall (greens), inertial (blues), viscous-inertial (pinks) and viscous flow regime (reds).

the ratio between the random loose packing $\phi_{\mathrm{rlp}} = 0.55$ and the column initial packing ϕ_0 to determine the flow's regime.

We classify the collapse regime according to the definition of Courrech du Pont *et al.* [79] that depends on $\mathrm{St}(d)$ and χ (see Eq. (2.12) and (2.13)) in the modified plane $((d/H_0)^{1/2}St, (d/H_0)^{1/2}\chi)$ proposed by Bougouin & Lacaze [133]. As we assume $d = d_{50}\phi_{\mathrm{rlp}}/\phi_0$, the plane for classifying the flow regime is $((\phi_{\mathrm{rlp}}/\phi_0)^2(d/H_0)^{1/2}St, (\phi_{\mathrm{rlp}}/\phi_0)^{1/2}(d/H_0)^{1/2}\chi)$. This plane provides a good interpretation of the transition between one regime to another, and allowed us to clearly identify column collapses that transit from the inertial to the viscous regime enhanced by H_0 and ϕ_0. Fig. 7.2 presents all results, both from experiments and simulations, mapping the regime to which they belong.

After classifying the column collapses by flow regime, we can now present the scaling between L^* and E_K^U, identifying the regime of each experiment or simulation (see Fig. 7.3). This time, it is easy to understand that granular column collapses belonging to the viscous regime do not follow the main trend between the final runout and the collapse energy. This suggest that the proportionality between L^* and E_K^U remains true for granular columns which collapse kinematic is mainly controlled by gravity (e.i. collapses belonging to the *free-fall*, *inertial*, and the transitional *viscous-inertial* regime) and not by the Stokes velocity. Excluding column collapses in the viscous regime, we obtained that all collapses are well correlated with a proportionality coefficient of 0.19 that can be interpreted as a rate of energy loss in gravity-driven flows (see inset of Fig. 7.3).

*For Fig. 7.3, and for the next figures included in this chapter, the results of Lee [127] of granular columns in inclined planes are not included.

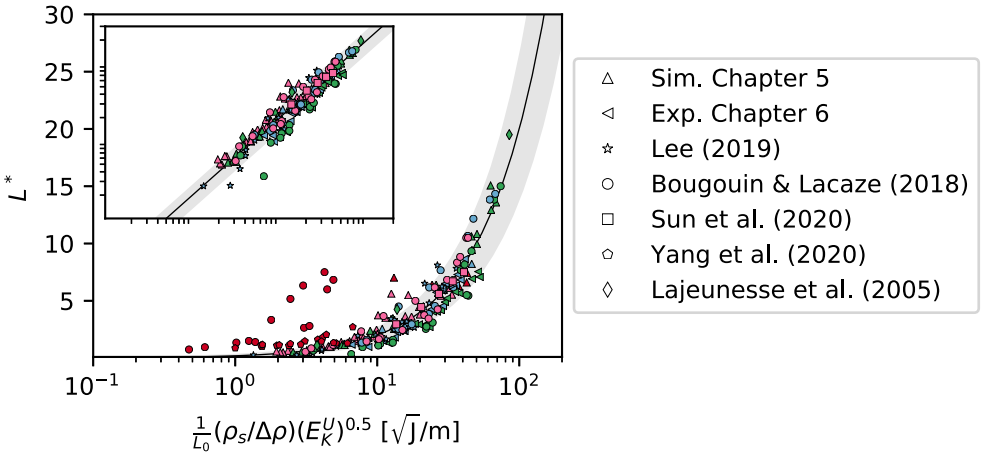

Figure 7.3. Scaling between the collapse energy E_K^U and the normalised runout L^*, distinguishing the collapse regimes presented in Fig. 7.2. The line is the best fit for all column collapses belonging to the free-fall (green), inertial (blue) and viscous inertial regime (pink) (see inset), having a proportionality coefficient of 0.19*. The grey shaded region represents a deviation of $\pm 30\%$.

We validate that the simplified model, proposed in Chapter 5 for numerical results in two-dimensions, remains true for experimental column collapses. Moreover, we prove the model with the results of different authors who covered a wider range of aspect ratios $A \in [0.21 - 16.7]$, confirming the model validity for shorter and taller columns. We understand that this model is an oversimplification of a complex physical process, but it is remarkable that the model can effectively link the final runout with the collapse kinematics across various levels of polydispersity and for both dry and immersed collapses. It is outstanding too that this model does not depend on fitting values, and it only needs materials parameters (i.e., ρ_s and ρ_f) and physically based variables (i.e., L_0, H_0, ϕ and U). This model is validated and supported with results from distinct methodologies and from experimental studies conducted by different authors. The fact that all results align on the same suggest the possibility of a universal model. If this simplified model can be used to establish a universal link between the collapse mobility and kinematics, it may prove useful in analysing and comprehending mass movements like landslides or debris flows, in areas where the only available data is the mobility and an interpretation of the initial geometry [6].

7.3 | Predictions Based on the Model

So far, we have presented a correlation between the normalised final column runout L^* and the collapse kinetic energy E_K^U conceived from an sliding block model. We claimed that this simplified scaling could be used as a back analysis tool for analysing and comprehending ancient landslides or debris flows, but based on previous observations, we consider that it has the potential of being a model for predicting the runout of granular collapses[†].

[†]**Short story about the model.** During a presentation of my research in the periodic meeting of the research group MéTICE at LMGC, I said '... Mobility models are a tool for predicting the mobility of granular

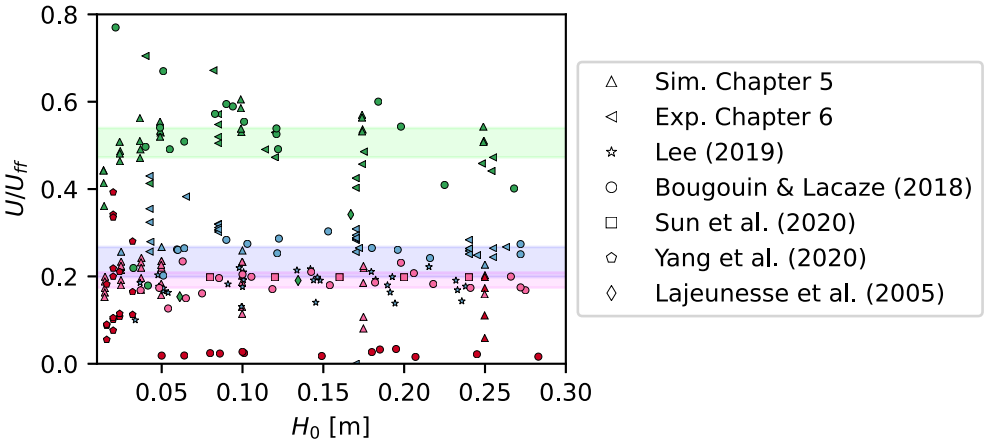

Figure 7.4. Front collapse velocity U normalised by the theoretical free-fall velocity U_{ff} (see Eq. (2.19)) as a function of the initial column height H_0. The shaded regions are delimited by the first and third quartile of U/U_{ff} for the free-fall (green), inertial (blue) and viscous inertial regime (pink) found for all the data available. The column collapse regime classification is presented in Fig. 7.2.

The simplified model that we propose establishes a good correlation between the column runout and the kinematic energy during collapse. The latter, the energy E_K^U, depends on the column mass M and the front velocity U. Previous studies have shown that U is proportional to the theoretical free-fall velocity U_{ff} (see Eq. (2.19) and Fig. 2.10 (b)) [123, 126, 130, 133, 160] and we have evidenced the same proportionality (see Fig. 5.4 and Fig. 6.12). Fig. 7.4 presents the ratio between the column velocity U and the theoretical free-fall velocity U_{ff} for all the results that we had available. We found representative values U/U_{ff} for each flow regime and propose that the front velocity U can be estimated as:

$$U = \begin{cases} 0.51U_{\mathrm{ff}} & \text{for Free} - \text{Fall}, \\ 0.24U_{\mathrm{ff}} & \text{for Inertial}, \\ 0.19U_{\mathrm{ff}} & \text{for Viscous} - \text{Inertial}, \end{cases} \tag{7.2}$$

with the constants 0.51, 0.24 and 0.19 being the median proportionality found for all the results belonging to the free-fall, inertial and viscous-inertial regime, respectively (see Fig. 7.4). Although there is a proportionality between U_{ff} and U for the granular column collapses belonging to the viscous regime (see Fig. 2.10 (b)), we decided not to include them in Eq. (7.2) because the whole collapse process, including the front velocity, is mainly controlled by the Stokes Velocity and do not follow the trend that we propose.
In Eq. (7.1) we replaced E_K^U by $L_0^2 A \phi_0 \rho_{\mathrm{s}} U/2$ and obtained an expression that only depends on material properties (i.e. ρ_{s}, ρ_{f}), initial column configuration (i.e., L_0, H_0, ϕ), and the

flow ...' and I presented the scaling between L^* and E_K^U. After my presentation, Loïc DARIDON, a researcher from the lab, said '... in the form that you have your model, it could be used for back analysis, but not for prediction... ', and he was right. In that moment, although it was missing something, I realised that we could also use the model for doing predictions.

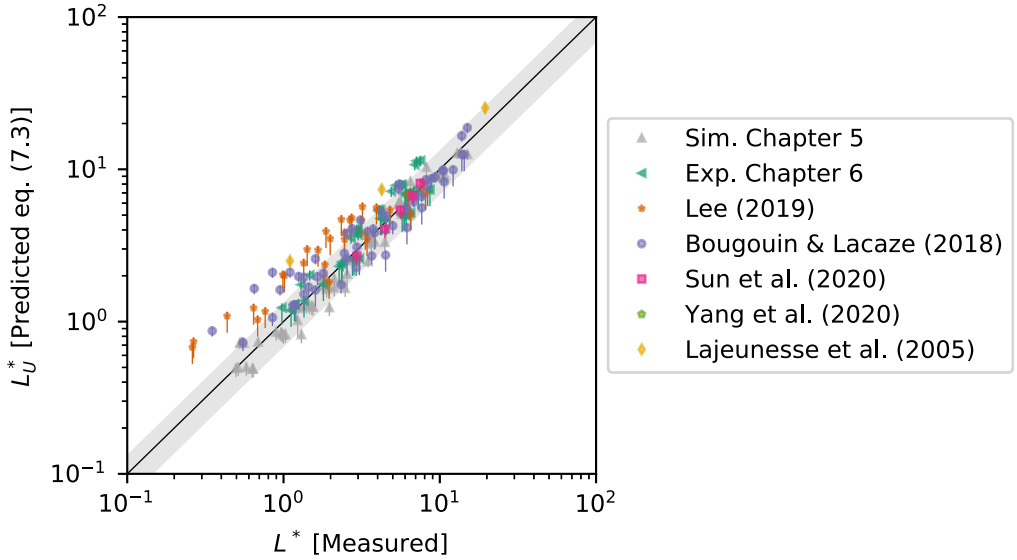

Figure 7.5. Comparison of reported column runout L^* and predicted runout L_U^* according to Eq. (7.3). The error bars are the variability associated to the front velocity U (see Fig. 7.4). The black line stands for the 1:1 proportionality and the grey shaded region indicates an error of $\pm 30\%$.

front velocity U as

$$L_U^* = 0.19 \frac{1}{\sqrt{2}} \frac{\rho_s^{3/2}}{\Delta\rho} U \sqrt{A\phi}. \tag{7.3}$$

With Eq. (7.3) and with 0.19 as the proportionality coefficient found for correlating the column runout and the column collapse energy (see Fig. 7.3), it is possible to predict the runout of granular columns. Fig. 7.5 presents a comparison of the runout predicted with the energy based model of Eq. (7.3) and the measured column runout. In general, the prediction shows accurate and works well for a wide range of L^*; however, the prediction lacks accuracy with the results of Lee [127]. Those experiments were done with sand of different sizes that, intrinsically, have different shapes and a higher friction coefficient, resulting in collapses with lower velocity and shorter runout compared with experiments or simulations made with spheres (or disks in two-dimensional simulations). Therefore, the prediction made with Eq. (7.3) overestimates the runout because the predicted velocity U in Eq. (7.2)) is mainly based on experiments and simulations that do not account for rough grains.

Although the runout predicted with Eq. (7.3) shows a good agreement with the runout measured in the experiments and simulations, the predictions do not precisely foretell the runout and have error. Fig. 7.6 presents the relative error between the predicted and the measured runout as

$$\text{error} = \frac{|L_U^* - L^*|}{L^*}. \tag{7.4}$$

Besides, Fig. 7.6 presents the relative error between the runout measured and the runout predicted with the well known scaling between A and L^* (see Eq. (2.21)), using the parameters found by different authors (see Table 2.1). In Fig. 7.6 (a) we can compare the error of the

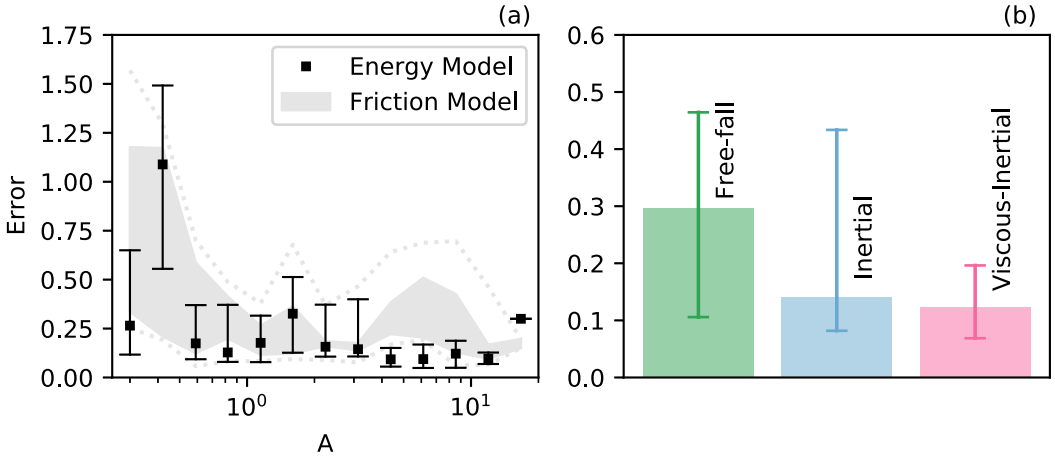

Figure 7.6. (a) Comparison of the absolute relative error between the measured and the predicted runout made with the energy model proposed in Eq. (7.3) and the prediction made with the friction model of Eq. (2.21) as a function of the column aspect ratio A for all the results reported in Fig. 7.5. For the energy model, the marker represents the median value and the error bars stand for the first and third quartile. For the predictions with the friction model, we used the values a and b proposed by Meruane *et al.* [122], Staron & Hinch [130], Topin *et al.* [132], and Bougouin & Lacaze [133]. The shaded area corresponds to the range spanning the minimum and maximum median errors, while the dashed lines represent the minimum first quartile and maximum third quartile. These values were obtained from the data reported by the previously mentioned authors. (b) Absolute relative error between the measured and the predicted runout made with the energy model proposed in Eq. (7.3), distinguishing the collapse flow regime. The error bars stand for the first and third quartile. Note that the limits of the vertical axis in figures (a) and (b) are different.

predictions made with the energy based model that we propose (Eq. (7.3)) and the friction based model (Eq. (2.21)) for all the results available. Both predictions show high variability for very short columns ($A < 0.5$), although they are biased by the experiments with rough grains that were previously discussed. The greatest variability obtained with the energy model occurs for the interval $A = [0.3 - 0.42]$, with an error greater than the error computed with the friction model, but this value may lack of statistical significance because it was obtained from only six results. For larger A, the error of both, the energy and friction based model, decreases and for many aspect ratio intervals the prediction made with Eq. (7.3) shows a better agreement with lower error. For the largest $A = 16.7$, the error with the energy based model is above the other, but it just accounts for a single point.

Lastly, when focusing only on the relative error of each flow regime, we observed that, on average, the highest error occurs during collapses in the free-fall regime, while the lowest error occurs in the viscous-inertial regime. Interestingly, for the free-fall regime we obtained the highest variability U/U_{ff} and, on the contrary, the lowest variability U/U_{ff} was obtained for the viscous-inertial regime.

7.4 | Conclusions

We tested the scaling between the column final runout and the collapse kinetic energy, initially proposed for polydisperse granular column collapses in two-dimensions (see Chapter 5), with the experimental results of polydisperse granular columns (see Chapter 6), and the results of Lajeunesse *et al.* [123], Lee [127], Bougouin & Lacaze [133], Yang *et al.* [159], and Sun *et al.* [160].

We confirmed that the link between the collapse energy during the propagation stage and the column mobility remains valid for three dimensional processes, and satisfactorily works for dry and immersed collapses. We have evidenced that the scaling works for granular column collapses in the free-fall, inertial, and viscous-inertial regimes where the collapse velocity is mainly controlled by gravity and it is not limited by the Stokes velocity. The model is an oversimplification of a complex physical process, but it is remarkable that it scales the final runout with the collapse kinematics for a wide range of polydispersity levels. Moreover, this model collapses numerical and experimental results on the same curve, pointing that it might capture a universal scaling.

Furthermore, alongside the link we found between the column mobility and the collapse kinematics, we propose an energy based model for estimating the runout of dry and immersed granular columns. This model only needs material parameters, initial geometric variables, the front velocity and the sole proportionality coefficient of (0.19) found between energy and runout. For an estimation of the front velocity, we relied on the observed proportionality between the collapse front velocity and the theoretical free-fall velocity, which has been previously studied and confirmed in this thesis (see Chapters 5 and 6). Based on the results of different authors and ours, we propose that the velocity of a column collapse could be estimated as 0.51, 0.24 and 0.19 times the theoretical free-fall velocity for columns belonging to the free-fall, inertial, and viscous-inertial flow regime, respectively. In this form, we suggest a predictive model that shows a good agreement with the results of experimental and numerical granular column collapses of different authors.

The prediction of the mobility of granular flows, and in our case granular columns, remains a challenging task that depends on several variables. Nevertheless, the model that we have suggested is supported by the findings of various authors and offers a reliable estimation of the mobility of granular columns. Additionally, the error associated with this model is comparable, if not lower, than the error incurred when employing the scaling for estimating the column runout based on the column aspect ratio.

Further works studying the relevance of the scaling between the column runout and the collapse kinetic energy could focus on the variables controlling the motion of collapses in the viscous regime, aiming to propose an scaling that rules all flow regimes. Moreover, further studies could focus on exploring the effect of inclined planes on the correlation between mobility and energy, with the intent of incorporating these findings into the trend that we propose. Furthermore, our findings showed that granular columns consisting of rough grains scale on the curve of energy and mobility that we propose. However, predicting the runout of columns

of such grains shows considerable variability. Therefore, future works could propose a front velocity estimation that takes into consideration the grains' angularity. Lastly, we claimed that the mobility model has the potential to be employed as a back-analysis tool for analysing and comprehending mass movements such as landslides or debris flows. Further studies could compare this mobility model with data from natural geophysical masses to evaluate its efficacy and limitations.

CHAPTER 8

Conclusions and Perspectives

> *Siempre he creído que toda versión de un cuento es mejor que la anterior. ¿Como saber entonces cuál debe ser la última?*
>
> **— Gabriel García Márquez (1927 - 2014)**
> Colombian writer. Nobel Prize in Literature, 1982

Conclusions

In this thesis, we studied experimentally and numerically the flow of granular materials, focusing on the effect that the grain size polydispersity has on them. We study granular materials in different configurations and varied their shear and stress conditions, studying granular flows in both the quasi-static, solid-like behavior, and dense regime, fluid-like behavior. Moreover, we studied dry and immersed transitional granular flows in the granular column collapse configuration, aiming to reveal the impact that polydispersity has on such flows. The following are the thesis' general conclusions that answer the open questions mentioned in Chapter 1 and discussed through Chapter 2.

We did an extensive experimental study about the influence that grain size, grain size polydispersity and grain size distribution have on the residual shear strength of granular materials. For this experimental study, we conducted an extensive experimental campaign in a triaxial test apparatus and use ceramic beads, focusing exclusively on the grains' size effect. The results of this study close a gap of knowledge between experiments and numerical simulations of quasi-static polydisperse granular materials, concluding that the residual shear strength is independent of the grain size, of the level of polydispersity, and of the Grain Size Distribution GSD shape (see Chapter 3)

We did a numerical campaign and studied granular flows in the shear cell configuration, focusing on the effect that polydispersity has on granular flows with different inertial levels. The results obtained allowed us to study the macroscopic behaviour of polydisperse granular materials and the grains' interaction at the contact scale. We showed that the independence of the shear strength to the polydispersity remains true for granular flows in the dense regime with an inertial number ranging between $I \in [10^{-4} - 0.1]$. We evidenced that the link between

the system's anisotropies and shear strength holds true across different polydispersity levels and a wide range of inertial numbers. This observation leaded us to the conclusion that the shear strength of polydisperse materials is lower than that of monodisperse materials because, at high inertial numbers, the sum of the system's anisotropies of polydisperse materials are insufficient to compensate the rapid increase of the contact anisotropy, the primary contributor to shear strength, in monodisperse materials (see Chapter 4).

We studied transitional granular flows in the granular column collapse configuration under both dry and immersed conditions. The aim of this study was to determine the effect that polydispersity has on transitional flows, specifically in immersed conditions. The study of polydisperse granular columns was conducted using a numerical approach with a coupled Finite Element Method and Discrete Element Method (see Chapter 5), as well as experimentally using nearly spherical beads to exclusively focus on the effect of the grains' sizes (see Chapter 6).

For the granular columns, we systematically varied the column aspect ratio, covering a range of short and tall columns while exploring different levels of polydispersity. We showed that the level of polydispersity has a stronger effect on immersed columns than on dry columns. For dry columns, the collapse sequence remains independent of the polydispersity level, reaching similar distances at similar times. This observation is common for short and tall columns. The final runout of the column, or final length, which is an indirect measure of the shear strength, vaguely varies with polydispersity, suggesting that polydispersity does not affect the shear strength.

We evidenced that the motion of immersed collapses is highly dependent on the level of polydispersity. We showed that the increment of the column polydispersity enhances the fluid-grains interactions, affecting the collapse sequence evolution, and most notably the collapse initiation and the runout distance. The variations of these two features are caused by differences in the evolution of the pore pressure. When the column starts to collapse there is a negative change of the pore pressure that provokes a temporally increase of the column's strength. We showed that the collapse of polydisperse columns is delayed because the negative change of pore pressure has a greater amplitude and remains for a longer period than in monodisperse columns. Moreover, the low permeability of polydisperse columns, due to high packing fraction and the presence of small grains, hinders the inflow of fluid into the column and provokes a retrogressive collapse of sliding layers. Then, during the column horizontal spreading, the grains' deposition augments the fluid pressure at the base of the moving mass. We revealed that in monodisperse flows the excess of pore pressure is rapidly dissipated, while for polydisperse flows the excess of pore pressure remains for a longer period, decreasing the strength and producing a localised fluidisation that results in longer runout distances (see Chapter 6).

We have proposed a mobility model for granular column collapses that correlates the collapse kinetic energy during the propagation stage with the final runout of the column. This model satisfactorily works for both monodisperse and polydisperse granular systems and remains valid for both experimental and numerical results. We have shown that the scaling applies

to granular column collapses where the collapse velocity is mainly controlled by gravity and is not limited by the Stokes velocity (i.e., flows in the free-fall, inertial, and viscous-inertial regime). The model is an oversimplification of a complex physical process, but it is remarkable that it scales the final runout with the collapse kinematics. This simplified model that we have introduced could be used as a tool for back analysis to analyze and understand mass movements such as landslides or debris flows. Furthermore, we extend this scaling between energy and mobility, and propose an energy based model for estimating the runout of granular columns. This model only needs materials parameters, initial geometric variables, the collapse front velocity and the sole proportionality coefficient found between energy and runout. We suggest a predictive model that shows a good agreement with the results of experimental and numerical granular column collapses of different authors (see Chapter 7).

We showed, in dry flows, that volume and friction laws initially proposed for monodisperse flows could be extended to polydisperse flows. We found that polydisperse flows satisfactorily follow the laws when the inertial number is computed with the diameter that holds 50% of the cumulative mass (see Chapter 4). In immersed cases, while characterising polydisperse granular flows with a characteristic diameter is crucial, we found that factors such as packing fractions and hydraulic conductivity gain significance when describing polydisperse granular flows (see Chapter 6).

Perspectives

Polydispersity in granular materials is a property that exhibits significant variability and leads to changes in other properties such as the packing fraction and the permeability, affecting the material's behaviour especially in immersed conditions. However, polydispersity is just one of many properties that exhibit significant variability in granular materials. For instance, the shape of the grains gains a major importance depending on the scale of the process studied. As the scale increases, so does the diversity in grain shapes. The grains's shape, and their orientation, influence the shear strength of granular materials [184] and the flow in immersed conditions [185]. Further studies could contribute on a deeper understanding of how the grains' shape, and intrinsically also the rugosity and orientation, affect granular flows.

In many processes, granular materials of different origins are involve in the same process. For example, the production of steel involves the transporting, depositing and, eventually, the melting of iron and coke grains. Debris flows are another example of granular flows that involve grains of different materials because they carry sand, gravel, rock boulders and even trees. Therefore, further works can do a valuable contributions if they explore the influence that grains of different materials, having different densities and/or friction coefficient, have on granular flows. Fig. 8.1 presents the results of a small experimental campaign which objective was to explore the influence of bidisperse materials in the mobility of granular columns. This results show that the mobility of immersed granular columns varies when the grains involved have different materials and, most importantly, indicate that the configuration has significant

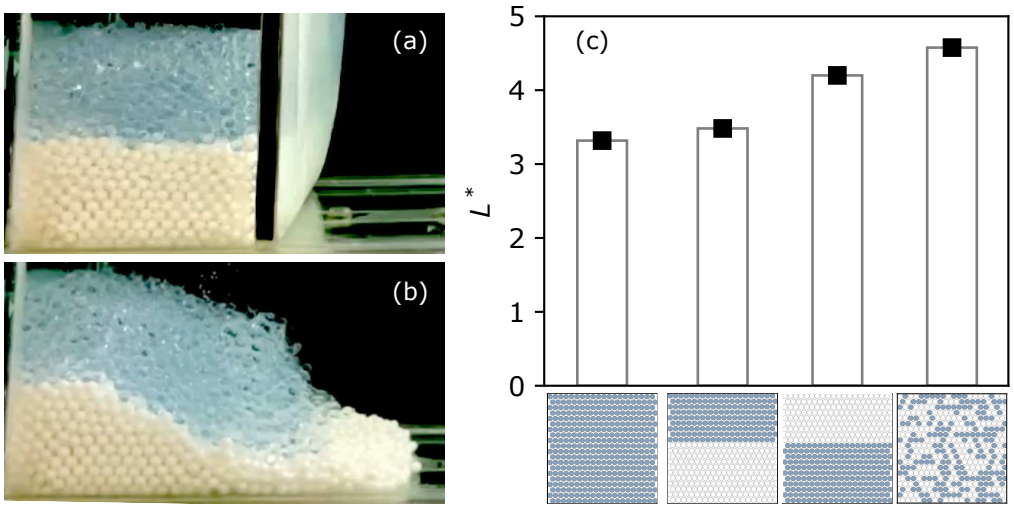

Figure 8.1. Collapse of a granular column of aspect ratio $A \sim 1$ composed of grains of different materials (glass beads, blues; and zirconium beads, whites) with diameter $d = 5$ mm. Figures (a) and (b) show images before and during the collapse, respectively. Figure (c) shows the normalised runout $L^* = (L_f - L_0)/L_0$ for different initial configurations*.

role. Further studies could study whether such kinds of systems are more affected by density segregation or by local differential velocities due to the material density.

Although the simulations of immersed polydisperse granular flows are limited by the physical considerations that we have made, they agree with the experiments, evidencing the strong influence of the packing fraction on the initiation of immersed granular flows. Further studies could employ more precise physical assumptions, implementing drag forces formulations for polydisperse systems or exploring a fine-scale solution for the fluid phase that allow a more detailed evolution of the pore pressure at the grain scale. Moreover, the experimental results of this thesis could be use for calibrate numerical simulations.

We have evidenced that increasing packing fraction, due to increasing polydispersity, strongly affects immersed granular flows. Polydispersity affects the packing fraction of granular materials when they transit from a solid-like to a fluid-like behaviour, but it also could affect long steady flows due to segregation [81]. Further studies would do a rich contribution if they focus on exploring the constitutive laws or if they propose segregation functions in immersed granular materials.

In this thesis, we explore the effect of polydispersity on transitional granular flows in the column collapse configuration, both in dry and immersed conditions. Further studies could focus on *something in the middle* and explore how wet polydisperse granular materials influence granular flows. A recent study by Gans *et al.* [137]† demonstrated that cohesive monodisperse grains lead to increased dissipation during flow, resulting in slower spreading of the material and a shorter runout length. It could be theorised that increasing polydispersity, especially the presence of smaller particles, might lead to a more dissipative flow due to an elevated

*I would like to thank José Moscote who did the experiments of granular column collapses with grains of different materials during his bachelor internship at Universidad de los Andes.

†I say 'recent' because the paper mentioned, the one by Gans *et al.* [137], was published the year that I submitted the thesis.

number of cohesive bonds. However, this is merely an initial hypothesis, and further research is necessary to fully understand the role of polydispersity in such systems.

The fracture of grains is a widely studied phenomenon in the granular materials community, as it holds significance in various fields such as mining, food processing, and construction. Among other reasons, grains fracture due to large punctual normal forces acting on them. One of our results indicates that strong and weak normal forces coincide with *short* and *long* branch lengths, and that the normal force between two grains is well described by a power-law function that depends on the branch length. We also showed that branch length occur with a distribution that depends on the polydispersity level and the inertial number (see Chapter 4). Further works could rely on previous studies about grain's fracture to obtain failure criteria and average grain sizes after failure [186], and propose a probability based law for the variation of the grain size distribution in granular flows based on our observations.

Bibliography

1. Andreotti, B., Y. Forterre & O. Pouliquen, *Granular Media: Between Fluid and Solid*. Cambridge University Press, 2013.
2. MiDi, G., "On dense granular flows". *The European Physical Journal E* 14, 341–365 2004.
3. Cabrera, M., & O. Polanía, "Heaps of sand in flows within a split-bottom Couette cell". *Phys. Rev. E* 102, 062901 6 Dec. 2020.
4. Asgarpour, M.. Offshore Wind Farms. eds Ng, C. & Ran, L. , 527–541. Woodhead Publishing, 2016.
5. Luckett, R., B. Baptie, L. Ottemoller & G. Thompson, "Seismic monitoring of the Soufrière Hills volcano, Montserrat". *Seismological Research Letters* 78, 192–200 2007.
6. Prada-Sarmiento, L. F., M. A. Cabrera, R. Camacho, N. Estrada & A. M. Ramos-Cañón, "The Mocoa Event on March 31 (2017): analysis of a series of mass movements in a tropical environment of the Andean-Amazonian Piedmont". *Landslides* 16, 2459–2468 2019.
7. Brilliantov, N., P. L. Krapivsky, A. Bodrova, F. Spahn, H. Hayakawa, V. Stadnichuk & J. Schmidt, "Size distribution of particles in Saturn's rings from aggregation and fragmentation". *Proceedings of the National Academy of Sciences* 112, 9536–9541 2015.
8. Chilingar, G. V.. Deltaic and Shallow Marine Deposits. ed van Straaten, L. , 71–75. Elsevier, 1964.
9. Rondon, L., O. Pouliquen & P. Aussillous, "Granular collapse in a fluid: Role of the initial volume fraction". *Physics of Fluids* 23, 073301 2011.
10. Iverson, R. M., "The physics of debris flows". *Reviews of Geophysics* 35, 245–296 1997.
11. Banerjee, S. K., M. Yang & M. Taiebat, "Effect of coefficient of uniformity on cyclic liquefaction resistance of granular materials". *Computers and Geotechnics* 155, 105232 2023.
12. Wichtmann, T., & T. Triantafyllidis, "Effect of uniformity coefficient on G/G max and damping ratio of uniform to well-graded quartz sands". *Journal of geotechnical and geoenvironmental engineering* 139, 59–72 2013.
13. Oquendo-Patiño, W. F., & N. Estrada, "Densest arrangement of frictionless polydisperse sphere packings with a power-law grain size distribution". *Granular Matter* 22, 1–8 2020.

14. Damasceno, P. F., M. Engel & S. C. Glotzer, "Predictive Self-Assembly of Polyhedra into Complex Structures". *Science* 337, 453–457 2012.

15. Scott, G. D., "Packing of Spheres: Packing of Equal Spheres". *Nature* 188, 908–909 1960.

16. Fuller, W. B., & S. E. Thompson, "The Laws of Proportioning Concrete". *Transactions of the American Society of Civil Engineers* 59, 67–143 1907.

17. Estrada, N., "Effects of grain size distribution on the packing fraction and shear strength of frictionless disk packings". *Phys. Rev. E* 94, 062903 6 Dec. 2016.

18. Oquendo-Patiño, W. F., & N. Estrada, "Finding the grain size distribution that produces the densest arrangement in frictional sphere packings: Revisiting and rediscovering the century-old Fuller and Thompson distribution". *Phys. Rev. E* 105, 064901 6 2022.

19. Nicot, F., N. Hadda, M. Guessasma, J. Fortin & O. Millet, "On the definition of the stress tensor in granular media". *International Journal of Solids and Structures* 50, 2508–2517 2013.

20. Yan, B., & R. A. Regueiro, "Definition and symmetry of averaged stress tensor in granular media and its 3D DEM inspection under static and dynamic conditions". *International Journal of Solids and Structures* 161, 243–266 2019.

21. Skempton, A. W., "Effective Stress in Soils, Concrete and Rocks", 106–118.

22. Ahmed, S. S., A. Martinez & J. T. DeJong, "Effect of Gradation on the Strength and Stress-Dilation Behavior of Coarse-Grained Soils in Drained and Undrained Triaxial Compression". *Journal of Geotechnical and Geoenvironmental Engineering* 149, 04023019 2023.

23. Iverson, R. M., "Landslide triggering by rain infiltration". *Water Resources Research* 36, 1897–1910 2000.

24. Hibert, C., G. Ekström & C. P. Stark, "Dynamics of the Bingham Canyon Mine landslides from seismic signal analysis". *Geophysical Research Letters* 41, 4535–4541 2014.

25. Farin, M., A. Mangeney, R. Toussaint, J. d. Rosny, N. Shapiro, T. Dewez, C. Hibert, C. Mathon, O. Sedan & F. Berger, "Characterization of rockfalls from seismic signal: Insights from laboratory experiments". *Journal of Geophysical Research: Solid Earth* 120, 7102–7137 2015.

26. Persichillo, M. G., M. Bordoni, M. Cavalli, S. Crema & C. Meisina, "The role of human activities on sediment connectivity of shallow landslides". *CATENA* 160, 261–274 2018.

27. Iverson, R. M., M. E. Reid, N. R. Iverson, R. G. LaHusen, M. Logan, J. E. Mann & D. L. Brien, "Acute Sensitivity of Landslide Rates to Initial Soil Porosity". *Science* 290, 513–516 2000.

28. Iverson, R. M., "Regulation of landslide motion by dilatancy and pore pressure feedback". *Journal of Geophysical Research: Earth Surface* 110 2005.

29. Radjai, F., "Modeling force transmission in granular materials". *Comptes Rendus Physique* 16, 3–9 2015.

30. Radjai, F., M. Jean, J.-J. Moreau & S. Roux, "Force Distributions in Dense Two-Dimensional Granular Systems". *Phys. Rev. Lett.* 77, 274–277 2 July 1996.

31. Voivret, C., F. Radjaı, J.-Y. Delenne & M. S. El Youssoufi, "Multiscale Force Networks in Highly Polydisperse Granular Media". *Phys. Rev. Lett.* 102, 178001 17 Apr. 2009.

32. Cantor, D., E. Azéma, P. Sornay & F. Radjai, "Rheology and structure of polydisperse three-dimensional packings of spheres". *Phys. Rev. E* 98, 052910 5 Nov. 2018.

33. Rothenburg, L. & Selvadurai, A. A micromechanical definition of the Cauchy stress tensor for particulate media. *Mechanics of structured media,* 469–486 1981.

34. Rothenburg, L., & R. J. Bathurst, "Analytical study of induced anisotropy in idealized granular materials". *Géotechnique* 39, 601–614 1989.

35. Azéma, E., Y. Descantes, N. Roquet, J.-N. Roux & F. ç. Chevoir, "Discrete simulation of dense flows of polyhedral grains down a rough inclined plane". *Phys. Rev. E* 86, 031303 3 2012.

36. Azéma, E., F. Radjai & F. Dubois, "Packings of irregular polyhedral particles: Strength, structure, and effects of angularity". *Phys. Rev. E* 87, 062203 6 June 2013.

37. Azéma, E., F. Radjai & G. Saussine, "Quasistatic rheology, force transmission and fabric properties of a packing of irregular polyhedral particles". *Mechanics of Materials* 41. Advances in the Dynamics of Granular Materials, 729–741 2009.

38. Cantor, D., E. Azéma & I. Preechawuttipong, "Microstructural analysis of sheared polydisperse polyhedral grains". *Phys. Rev. E* 101, 062901 6 June 2020.

39. Hungr, O.. Progress in Landslide Science. eds Sassa, K., Fukuoka, H., Wang, F. & Wang, G. , 47–57. Berlin, Heidelberg, Springer Berlin Heidelberg, 2007.

40. Mesri, G., & N. Huvaj-Sarihan, "Residual Shear Strength Measured by Laboratory Tests and Mobilized in Landslides". *Journal of Geotechnical and Geoenvironmental Engineering* 138, 585–593 2012.

41. Simoni, A., & G. T. Houlsby, "The direct shear strength and dilatancy of sand–gravel mixtures". *Geotechnical & Geological Engineering* 24, 523–549 2006.

42. Liu, Y., F. Guillard, B. Marks, P. Rognon & I. Einav, "The perpetual shearing of granular soils under low stresses using the stadium shear device". *Open Geomechanics* 3, 1–19 2022.

43. Santamarina, J., & H. Shin. Meso-scale Shear Physics in Earthquake and Landslide Mechanics. eds Yossef H., H., Jean, S. & Ioannis, V. , 157–188. London, SCRC Press, 2009.

44. Linero Molina, S., E. Azema, N. Estrada, S. Fityus, J. Simmons & A. Lizcano, "Impact of grading on steady-state strength". *Géotechnique Letters* 9, 328–333 2019.

45. Nguyen, D.-H., E. Azéma, P. Sornay & F. Radjai, "Effects of shape and size polydispersity on strength properties of granular materials". *Phys. Rev. E* 91, 032203 3 Mar. 2015.

46. Saint-Cyr, B., J.-Y. Delenne, C. Voivret, F. Radjai & P. Sornay, "Rheology of granular materials composed of nonconvex particles". *Phys. Rev. E* 84, 041302 4 Oct. 2011.

47. Estrada, N., A. Taboada & F. Radjaı, "Shear strength and force transmission in granular media with rolling resistance". *Phys. Rev. E* 78, 021301 2 Aug. 2008.

48. Liang, Y., T.-C. J. Yeh, J. Wang, M. Liu & Y. Hao, "Effect of particle size distribution on soil-steel interface shear behavior". *Soil Mechanics and Foundation Engineering* 54, 310–317 2017.

49. Wang, H.-L., W.-H. Zhou, Z.-Y. Yin & X.-X. Jie, "Effect of grain size distribution of sandy soil on shearing behaviors at soil-structure interface". *Journal of Materials in Civil Engineering* 31, 04019238 2019.

50. Carbillet, L., M. J. Heap, P. Baud, F. B. Wadsworth & T. Reuschlé, "The Influence of Grain Size Distribution on Mechanical Compaction and Compaction Localization in Porous Rocks". *Journal of Geophysical Research: Solid Earth* 127, e2022JB025216 2022.

51. Kokusho, T., T. Hara & R. Hiraoka, "Undrained Shear Strength of Granular Soils with Different Particle Gradations". *Journal of Geotechnical and Geoenvironmental Engineering* 130, 621–629 2004.

52. Igwe, O., H. Fukuoka & K. Sassa, "The effect of relative density and confining stress on shear properties of sands with varying grading". *Geotechnical and Geological Engineering* 30, 1207–1229 2012.

53. Cao, P., M.-j. Jiang & Z.-j. Ding, "Effects of particle size on mechanical behaviors of calcareous sand under triaxial conditions". *Japanese Geotechnical Society Special Publication* 8, 182–187 2020.

54. Amirpour Harehdasht, S., M. Karray, M. N. Hussien & M. Chekired, "Influence of particle size and gradation on the stress-dilatancy behavior of granular materials during drained triaxial compression". *International Journal of Geomechanics* 17, 04017077 2017.

55. Li, G., Y.-J. Liu, C. Dano & P.-Y. Hicher, "Grading-Dependent Behavior of Granular Materials: From Discrete to Continuous Modeling". *Journal of Engineering Mechanics* 141, 04014172 2015.

56. Yang, J., & X. Luo, "The critical state friction angle of granular materials: does it depend on grading?". *Acta Geotechnica* 13, 535–547 2018.

57. Zhao, S., J. Zhao & N. Guo, "Universality of internal structure characteristics in granular media under shear". *Phys. Rev. E* 101, 012906 1 Jan. 2020.

58. Zhu, Y., Z. Nie, J. Gong, J. Zou, L. Zhao & L. Li, "An analysis of the effects of the size ratio and fines content on the shear behaviors of binary mixtures using DEM". *Computers and Geotechnics* 118, 103353 2020.

59. Cabrera, M., & N. Estrada, "Is the Grain Size Distribution a Key Parameter for Explaining the Long Runout of Granular Avalanches?". *Journal of Geophysical Research: Solid Earth* 126, e2021JB022589 2021.

60. Iordanoff, I., & M. M. Khonsari, "Granular Lubrication: Toward an Understanding of the Transition Between Kinetic and Quasi-Fluid Regime ". *Journal of Tribology* 126, 137–145 Jan. 2004.

61. Da Cruz, F., S. Emam, M. Prochnow, J.-N. Roux & F. ç. Chevoir, "Rheophysics of dense granular materials: Discrete simulation of plane shear flows". *Phys. Rev. E* 72, 021309 2 Aug. 2005.

62. Jop, P., Y. Forterre & O. Pouliquen, "A constitutive law for dense granular flows". *Nature* 441, 727–730 2006.

63. Forterre, Y., & O. Pouliquen, "Flows of Dense Granular Media". *Annual Review of Fluid Mechanics* 40, 1–24 2008.

64. JOP, P., Y. FORTERRE & O. POULIQUEN, "Crucial role of sidewalls in granular surface flows: consequences for the rheology". *Journal of Fluid Mechanics* 541, 167–192 2005.

65. Chialvo, S., J. Sun & S. Sundaresan, "Bridging the rheology of granular flows in three regimes". *Phys. Rev. E* 85, 021305 2 Feb. 2012.

66. Bonamy, D., F. Daviaud, L. Laurent, M. Bonetti & J. P. Bouchaud, "Multiscale Clustering in Granular Surface Flows". *Phys. Rev. Lett.* 89, 034301 3 June 2002.

67. Pouliquen, O., "Velocity Correlations in Dense Granular Flows". *Phys. Rev. Lett.* 93, 248001 24 Dec. 2004.

68. Lois, G., A. Lemaıtre & J. M. Carlson, "Spatial force correlations in granular shear flow. I. Numerical evidence". *Phys. Rev. E* 76, 021302 2 Aug. 2007.

69. Azéma, E., & F. Radjaı, "Internal Structure of Inertial Granular Flows". *Phys. Rev. Lett.* 112, 078001 7 Feb. 2014.

70. Silbert, L. E., D. Erta ş, G. S. Grest, T. C. Halsey, D. Levine & S. J. Plimpton, "Granular flow down an inclined plane: Bagnold scaling and rheology". *Phys. Rev. E* 64, 051302 5 Oct. 2001.

71. Baran, O., D. Erta ş, T. C. Halsey, G. S. Grest & J. B. Lechman, "Velocity correlations in dense gravity-driven granular chute flow". *Phys. Rev. E* 74, 051302 5 Nov. 2006.

72. Pouliquen, O., "Scaling laws in granular flows down rough inclined planes". *Physics of fluids* 11, 542–548 1999.

73. Savage, S. B., "The Mechanics of Rapid Granular Flows". *Advances in Applied Mechanics* 24. eds Hutchinson, J. W. & Wu, T. Y. , 289–366 1984.

74. Otsuki, M., & H. Hayakawa, "Critical behaviors of sheared frictionless granular materials near the jamming transition". *Phys. Rev. E* 80, 011308 1 July 2009.

75. Gu, Y., A. Ozel & S. Sundaresan, "Rheology of granular materials with size distributions across dense-flow regimes". *Powder Technology* 295, 322–329 2016.

76. Rognon, P. G., J.-N. Roux, M. Naaïm & F. Chevoir, "Dense flows of bidisperse assemblies of disks down an inclined plane". *Physics of Fluids* 19, 058101 May 2007.

77. Dahl, S., R. Clelland & C. Hrenya, "Three-dimensional, rapid shear flow of particles with continuous size distributions". 138, 7–12 2003.

78. Breard, E. C. P., J. Dufek, L. Fullard & A. Carrara, "The Basal Friction Coefficient of Granular Flows With and Without Excess Pore Pressure: Implications for Pyroclastic Density Currents, Water-Rich Debris Flows, and Rock and Submarine Avalanches". *Journal of Geophysical Research: Solid Earth* 125, e2020JB020203 2020.

79. Courrech du Pont, S., P. Gondret, B. Perrin & M. Rabaud, "Granular Avalanches in Fluids". *Phys. Rev. Lett.* 90, 044301 4 Jan. 2003.

80. Boyer, F. ç., É. Guazzelli & O. Pouliquen, "Unifying Suspension and Granular Rheology". *Phys. Rev. Lett.* 107, 188301 18 Oct. 2011.

81. Guazzelli, É., & O. Pouliquen, "Rheology of dense granular suspensions". *Journal of Fluid Mechanics* 852, P1 2018.

82. Trulsson, M., B. Andreotti & P. Claudin, "Transition from the Viscous to Inertial Regime in Dense Suspensions". *Phys. Rev. Lett.* 109, 118305 11 Sept. 2012.

83. Amarsid, L., J.-Y. Delenne, P. Mutabaruka, Y. Monerie, F. Perales & F. Radjai, "Viscoinertial regime of immersed granular flows". *Phys. Rev. E* 96, 012901 1 July 2017.

84. Tapia, F., M. Ichihara, O. Pouliquen & É. Guazzelli, "Viscous to Inertial Transition in Dense Granular Suspension". *Phys. Rev. Lett.* 129, 078001 7 Aug. 2022.

85. Lacaze, L., J. Bouteloup, B. Fry & E. Izard, "Immersed granular collapse: from viscous to free-fall unsteady granular flows". *Journal of Fluid Mechanics* 912, A15 2021.

86. Rauter, M., "The compressible granular collapse in a fluid as a continuum: validity of a Navier–Stokes model with $\mu(J)$, $\phi(J)$-rheology". *Journal of Fluid Mechanics* 915, A87 2021.

87. Pudasaini, S. P., "A fully analytical model for virtual mass force in mixture flows". *International Journal of Multiphase Flow* 113, 142–152 2019.

88. Rognon, P. G., I. Einav & C. Gay, "Flowing resistance and dilatancy of dense suspensions: lubrication and repulsion". *Journal of Fluid Mechanics* 689, 75–96 2011.

89. Mema, I., V. V. Mahajan, B. W. Fitzgerald & J. T. Padding, "Effect of lift force and hydrodynamic torque on fluidisation of non-spherical particles". *Chemical Engineering Science* 195, 642–656 2019.

90. DallaValle, J. M. *Micromeritics: the technology of the particles* Pitman Publishing Corporation, 1943.

91. Goldstein, S., & H. Jeffreys, "The steady flow of viscous fluid past a fixed spherical obstacle at small reynolds numbers". *Proceedings of the Royal Society of London. Series A, Containing Papers of a Mathematical and Physical Character* 123, 225–235 1929.

92. Morrison, F. A., *An Introduction to Fluid Mechanics*. Cambridge University Press, 2013.

93. ROOS, F. W., & W. W. WILLMARTH, "Some experimental results on sphere and disk drag". *AIAA Journal* 9, 285–291 1971.

94. Di Felice, R., "The voidage function for fluid-particle interaction systems". *International Journal of Multiphase Flow* 20, 153–159 1994.

95. Nucci, E., A. Armanini & M. Larcher, "Drag forces in statistically stationary and homogeneous submerged granular flows". *Phys. Rev. E* 99, 042904 4 Apr. 2019.

96. Richardson, J., & W. Zaki, "The sedimentation of a suspension of uniform spheres under conditions of viscous flow". *Chemical Engineering Science* 3, 65–73 1954.

97. Beetstra, R., M. van der Hoef & J. Kuipers, "Numerical study of segregation using a new drag force correlation for polydisperse systems derived from lattice-Boltzmann simulations". *Chemical Engineering Science* 62, 246–255 2007.

98. Cello, F., A. Di Renzo & F. P. Di Maio, "A semi-empirical model for the drag force and fluid–particle interaction in polydisperse suspensions". *Chemical Engineering Science* 65, 3128–3139 2010.

99. Knight, C., C. O'Sullivan, B. van Wachem & D. Dini, "Computing drag and interactions between fluid and polydisperse particles in saturated granular materials". *Computers and Geotechnics* 117, 103210 2020.

100. Garcia, M., *Sedimentation Engineering* MOP 110. American Society of Civil Engineers, 2008.

101. Kaitna, R., M. C. Palucis, B. Yohannes, K. M. Hill & W. E. Dietrich, "Effects of coarse grain size distribution and fine particle content on pore fluid pressure and shear behavior in experimental debris flows". *Journal of Geophysical Research: Earth Surface* 121, 415–441 2016.

102. Jackson, R., "Locally averaged equations of motion for a mixture of identical spherical particles and a Newtonian fluid". *Chemical Engineering Science* 52. Mathematical modelling of chemical and biochemical processes, 2457–2469 1997.

103. Pirulli, M., & A. Mangeney, "Results of back-analysis of the propagation of rock avalanches as a function of the assumed rheology". *Rock Mechanics and Rock Engineering* 41, 59–84 2008.

104. GRAY, J. M. N. T., & C. ANCEY, "Segregation, recirculation and deposition of coarse particles near two-dimensional avalanche fronts". *Journal of Fluid Mechanics* 629, 387–423 2009.

105. Gray, J. M. N. T., & C. Ancey, "Multi-component particle-size segregation in shallow granular avalanches". *Journal of Fluid Mechanics* 678, 535–588 2011.

106. Edwards, A., F. Rocha, B. Kokelaar, C. Johnson & J. Gray, "Particle-size segregation in self-channelized granular flows". *Journal of Fluid Mechanics* 955, A38 2023.

107. Cundall, P. A., & O. D. L. Strack, "A discrete numerical model for granular assemblies". *Géotechnique* 29, 47–65 1979.

108. Moreau, J. J., "Sorne numerical methods in multibody dynamics: application to granular materials". *European Journal of Mechanics-A/Solids* 13, 93–114 1994.

109. Jean, M., "The non-smooth contact dynamics method". *Computer Methods in Applied Mechanics and Engineering* 177, 235–257 1999.

110. Dubois, F., V. Acary & M. Jean, "The Contact Dynamics method: A nonsmooth story". *Comptes Rendus Mécanique* 346, 247–262 2018.

111. Wachs, A., "PeliGRIFF, a parallel DEM-DLM/FD direct numerical simulation tool for 3D particulate flows". *Journal of Engineering Mathematics* 71, 131–155 2011.

112. Galindo-Torres, S., "A coupled Discrete Element Lattice Boltzmann Method for the simulation of fluid–solid interaction with particles of general shapes". *Computer Methods in Applied Mechanics and Engineering* 265, 107–119 2013.

113. Kumar, K., J.-Y. Delenne & K. Soga, "Mechanics of granular column collapse in fluid at varying slope angles". *Journal of Hydrodynamics* 29, 529–541 2017.

114. Tsuji, Y., T. Kawaguchi & T. Tanaka, "Discrete particle simulation of two-dimensional fluidized bed". *Powder Technology* 77, 79–87 1993.

115. Constant, M., F. Dubois, J. Lambrechts & V. Legat, "Implementation of an unresolved stabilised FEM–DEM model to solve immersed granular flows". *Computational Particle Mechanics* 6, 213–226 2019.

116. Koval, G., J.-N. Roux, A. Corfdir & F. ç. Chevoir, "Annular shear of cohesionless granular materials: From the inertial to quasistatic regime". *Phys. Rev. E* 79, 021306 2 Feb. 2009.

117. Pouliquen, O., & R. Gutfraind, "Stress fluctuations and shear zones in quasistatic granular chute flows". *Phys. Rev. E* 53, 552–561 1 Jan. 1996.

118. Grasselli, Y., & H. Herrmann, "On the angles of dry granular heaps". *Physica A: Statistical Mechanics and its Applications* 246, 301–312 1997.

119. Delannay, R., A. Valance, A. Mangeney, O. Roche & P. Richard, "Granular and particle-laden flows: from laboratory experiments to field observations". *Journal of Physics D: Applied Physics* 50, 053001 2017.

120. Balmforth, N. J., & R. R. Kerswell, "Granular collapse in two dimensions". *Journal of Fluid Mechanics* 538, 399–428 2005.

121. Lube, G., H. E. Huppert, R. S. J. Sparks & M. A. Hallworth, "Axisymmetric collapses of granular columns". *Journal of Fluid Mechanics* 508, 175–199 2004.

122. Meruane, C., A. Tamburrino & O. Roche, "On the role of the ambient fluid on gravitational granular flow dynamics". *Journal of Fluid Mechanics* 648, 381–404 2010.

123. Lajeunesse, E., J. B. Monnier & G. M. Homsy, "Granular slumping on a horizontal surface". *Physics of Fluids* 17, 103302 2005.

124. Man, T., H. E. Huppert, Z. Zhang & S. A. Galindo-Torres, "Influence of cross-section shape on granular column collapses". *Powder Technology* 407, 117591 2022.

125. Lacaze, L., J. C. Phillips & R. R. Kerswell, "Planar collapse of a granular column: Experiments and discrete element simulations". *Physics of Fluids* 20. 063302 June 2008.

126. Pinzon, G., & M. Cabrera, "Planar collapse of a submerged granular column". *Physics of Fluids* 31, 086603 2019.

127. Lee, C.-H., "Underwater collapse of a loosely packed granular column on an inclined plane: Effects of the Darcy number". *AIP Advances* 9, 095046 2019.

128. Cabrera, M. A., G. Pinzon, W. A. Take & R. P. Mulligan, "Wave Generation Across a Continuum of Landslide Conditions From the Collapse of Partially Submerged to Fully Submerged Granular Columns". *Journal of Geophysical Research: Oceans* 125, e2020JC016465 2020.

129. Sarlin, W., C. Morize, A. Sauret & P. Gondret, "Nonlinear regimes of tsunami waves generated by a granular collapse". *Journal of Fluid Mechanics* 919, R6 2021.

130. Staron, L., & E. J. Hinch, "Study of the collapse of granular columns using two-dimensional discrete-grain simulation". *Journal of Fluid Mechanics* 545, 1–27 2005.

131. Zenit, R., "Computer simulations of the collapse of a granular column". *Physics of Fluids* 17, 031703 2005.

132. Topin, V., Y. Monerie, F. Perales & F. Radjaı, "Collapse Dynamics and Runout of Dense Granular Materials in a Fluid". *Phys. Rev. Lett.* 109, 188001 18 Nov. 2012.

133. Bougouin, A., & L. Lacaze, "Granular collapse in a fluid: Different flow regimes for an initially dense-packing". *Phys. Rev. Fluids* 3, 064305 6 June 2018.

134. Staron, L., & E. Hinch, "The spreading of a granular mass: role of grain properties and initial conditions". *Granular Matter* 9, 205–217 2007.

135. Zhang, P., L. Qiu, Y. Chen, Y. Zhao, L. Kong, A. Scheuermann, L. Li & S. Galindo-Torres, "Coupled metaball discrete element lattice Boltzmann method for fluid-particle systems with non-spherical particle shapes: A sharp interface coupling scheme". *Journal of Computational Physics* 479, 112005 2023.

136. Bougouin, A., L. Lacaze & T. Bonometti, "Collapse of a neutrally buoyant suspension column: from Newtonian to apparent non-Newtonian flow regimes". *Journal of Fluid Mechanics* 826, 918–941 2017.

137. Gans, A., A. Abramian, P.-Y. Lagrée, M. Gong, A. Sauret, O. Pouliquen & M. Nicolas, "Collapse of a cohesive granular column". *Journal of Fluid Mechanics* 959, A41 2023.

138. Wang, C., Y. Wang, C. Peng & X. Meng, "Dilatancy and compaction effects on the submerged granular column collapse". *Physics of Fluids* 29, 103307 2017.

139. Lee, C.-H., "Two-phase modelling of submarine granular flows with shear-induced volume change and pore-pressure feedback". *Journal of Fluid Mechanics* 907, A31 2021.

140. Lagrée, P.-Y., L. Staron & S. Popinet, "The granular column collapse as a continuum: validity of a two-dimensional Navier–Stokes model with a (I)-rheology". *Journal of Fluid Mechanics* 686, 378–408 2011.

141. Cabrera, M., & N. Estrada, "Granular column collapse: Analysis of grain-size effects". *Phys. Rev. E* 99, 012905 1 Jan. 2019.

142. Pailha, M., M. Nicolas & O. Pouliquen, "Initiation of underwater granular avalanches: Influence of the initial volume fraction". *Physics of Fluids* 20, 111701 2008.

143. Pailha, M., & O. Pouliquen, "A two-phase flow description of the initiation of underwater granular avalanches". *Journal of Fluid Mechanics* 633, 115–135 2009.

144. Iverson, R. M., M. E. Reid, N. R. Iverson, R. G. LaHusen, M. Logan, J. E. Mann & D. L. Brien, "Acute Sensitivity of Landslide Rates to Initial Soil Porosity". *Science* 290, 513–516 2000.

145. Mutabaruka, P., J.-Y. Delenne, K. Soga & F. Radjai, "Initiation of immersed granular avalanches". *Phys. Rev. E* 89, 052203 5 May 2014.

146. Gee, M., D. Masson, A. Watts & P. Allen, "The Saharan debris flow: an insight into the mechanics of long runout submarine debris flows". *Sedimentology* 46, 317–335 1999.

147. Legros, F., "The mobility of long-runout landslides". *Engineering Geology* 63, 301–331 2002.

148. Mangeney-Castelnau, A., F. Bouchut, J. P. Vilotte, E. Lajeunesse, A. Aubertin & M. Pirulli, "On the use of Saint Venant equations to simulate the spreading of a granular mass". *Journal of Geophysical Research: Solid Earth* 110 2005.

149. Degaetano, M., L. Lacaze & J. C. Phillips, "The influence of localised size reorganisation on short-duration bidispersed granular flows". *The European Physical Journal E* 36, 1–9 2013.

150. Roche, O., M. Attali, A. Mangeney & A. Lucas, "On the run-out distance of geophysical gravitational flows: Insight from fluidized granular collapse experiments". *Earth and Planetary Science Letters* 311, 375–385 2011.

151. Warnett, J., P. Denissenko, P. Thomas, E. Kiraci & M. Williams, "Scalings of axisymmetric granular column collapse". *Granular Matter* 16, 115–124 2014.

152. Roche, O., M. Gilbertson, J. Phillips & R. Sparks, "Inviscid behaviour of fines-rich pyroclastic flows inferred from experiments on gas–particle mixtures". *Earth and Planetary Science Letters* 240, 401–414 2005.

153. Meruane, C., A. Tamburrino & O. Roche, "Dynamics of dense granular flows of small-and-large-grain mixtures in an ambient fluid". *Phys. Rev. E* 86, 026311 2 Aug. 2012.

154. He, K., H. Shi & X. Yu, "An experimental study on aquatic collapses of bidisperse granular deposits". *Physics of Fluids* 33, 103311 2021.

155. Martinez, F., A. Tamburrino, V. Casis & P. Ferrer, "Segregation effects on flow's mobility and final morphology of axisymmetric granular collapses". *Granular Matter* 24, 101 2022.

156. Watanabe, D., S. Moriguchi & K. Terada, "A numerical study on the effects of particle size distribution on run-out distance of granular flow". *Soils and Foundations* 62, 101242 2022.

157. Lai, Z., L. E. Vallejo, W. Zhou, G. Ma, J. M. Espitia, B. Caicedo & X. Chang, "Collapse of Granular Columns With Fractal Particle Size Distribution: Implications for Understanding the Role of Small Particles in Granular Flows". *Geophysical Research Letters* 44, 12, 181–12, 189 2017.

158. Sarlin, W., C. Morize, A. Sauret & P. Gondret, "Collapse dynamics of dry granular columns: From free-fall to quasistatic flow". *Phys. Rev. E* 104, 064904 6 Dec. 2021.

159. Yang, G. C., L. Jing, C. Y. Kwok & Y. D. Sobral, "Pore-Scale Simulation of Immersed Granular Collapse: Implications to Submarine Landslides". *Journal of Geophysical Research: Earth Surface* 125, e2019JF005044 2020.

160. Sun, Y.-h., W.-t. Zhang, X.-l. Wang & Q.-q. Liu, "Numerical study on immersed granular collapse in viscous regime by particle-scale simulation". *Physics of Fluids* 32, 073313 2020.

161. Guo, X., T. Stoesser, D. Zheng, Q. Luo, X. Liu & T. Nian, "A methodology to predict the run-out distance of submarine landslides". *Computers and Geotechnics* 153, 105073 2023.

162. Polanıa, O., M. Cabrera, M. Renouf, E. Azéma & N. Estrada, "Grain size distribution does not affect the residual shear strength of granular materials: An experimental proof". *Phys. Rev. E* 107, L052901 5 May 2023.

163. Wood, D. M., *Soil Behaviour and Critical State Soil Mechanics*. Cambridge University Press, 1991.

164. Wang, B., Y. Li, D. Liu & J. Liu, "Debris flow density determined by grain composition". *Landslides* 15, 1205–1213 2018.

165. Deng, Y., Y. Yilmaz, A. Gokce & C. S. Chang, "Influence of particle size on the drained shear behavior of a dense fluvial sand". *Acta Geotechnica* 16, 2071–2088 2021.

166. Wackenhut, M., S. McNamara & H. Herrmann, "Shearing behavior of polydisperse media". *The European Physical Journal E* 17, 237–246 2005.

167. *LMGC90* Available at `https://git-xen.lmgc.univ-montp2.fr/lmgc90/lmgc90_user`

168. Voivret, C., F. Radjaı, J.-Y. Delenne & M. S. El Youssoufi, "Space-filling properties of polydisperse granular media". *Phys. Rev. E* 76, 021301 2 Aug. 2007.

169. Mutabaruka, P., M. Taiebat, R. J.-M. Pellenq & F. Radjai, "Effects of size polydispersity on random close-packed configurations of spherical particles". *Phys. Rev. E* 100, 042906 4 Oct. 2019.

170. Pouliquen, O., C. Cassar, P. Jop, Y. Forterre & M. Nicolas, "Flow of dense granular material: towards simple constitutive laws". *Journal of Statistical Mechanics: Theory and Experiment* 2006, P07020 2006.

171. Radjai, F., D. E. Wolf, M. Jean & J.-J. Moreau, "Bimodal Character of Stress Transmission in Granular Packings". *Phys. Rev. Lett.* 80, 61–64 1 Jan. 1998.

172. Polanıa, O., M. Cabrera, M. Renouf & E. Azéma, "Collapse of dry and immersed polydisperse granular columns: A unified runout description". *Phys. Rev. Fluids* 7, 084304 8 2022.

173. Dalcin, L. D., R. R. Paz, P. A. Kler & A. Cosimo, "Parallel distributed computing using Python". *Advances in Water Resources* 34, 1124–1139 2011.

174. Capecelatro, J., & O. Desjardins, "An Euler–Lagrange strategy for simulating particle-laden flows". *Journal of Computational Physics* 238, 1–31 2013.

175. Mitchell, J. K., Soga, K., *et al. Fundamentals of soil behavior* 2005.

176. Hinrichsen, E. L., J. Feder & T. Jøssang, "Random packing of disks in two dimensions". *Phys. Rev. A* 41, 4199–4209 8 Apr. 1990.

177. Kausch, H., D. Fesko & N. Tschoegl, "The random packing of circles in a plane". *Journal of Colloid and Interface Science* 37, 603–611 1971.

178. Thompson, E. L., & H. E. Huppert, "Granular column collapses: further experimental results". *Journal of Fluid Mechanics* 575, 177–186 2007.

179. Azéma, E., S. Linero, N. Estrada & A. Lizcano, "Shear strength and microstructure of polydisperse packings: The effect of size span and shape of particle size distribution". *Phys. Rev. E* 96, 022902 2 Aug. 2017.

180. Bradski, G., "The OpenCV Library". *Dr. Dobb's Journal of Software Tools* 2000.

181. Virtanen, P., R. Gommers, T. E. Oliphant, M. Haberland, T. Reddy, D. Cournapeau, E. Burovski, P. Peterson, W. Weckesser, J. Bright, S. J. van der Walt, M. Brett, J. Wilson, K. J. Millman, N. Mayorov, A. R. J. Nelson, E. Jones, R. Kern, E. Larson, C. J. Carey, İ. Polat, Y. Feng, E. W. Moore, J. VanderPlas, D. Laxalde, J. Perktold, R. Cimrman, I. Henriksen, E. A. Quintero, C. R. Harris, A. M. Archibald, A. H. Ribeiro, F. Pedregosa, P. van Mulbregt & SciPy 1.0 Contributors, "SciPy 1.0: Fundamental Algorithms for Scientific Computing in Python". *Nature Methods* 17, 261–272 2020.

182. Ilstad, T., J. G. Marr, A. Elverhøi & C. B. Harbitz, "Laboratory studies of subaqueous debris flows by measurements of pore-fluid pressure and total stress". *Marine Geology* 213, 403–414 2004.

183. Carman, P., "Fluid flow through granular beds". *Chemical Engineering Research and Design* 75, S32–S48 1937.

184. Pinzón, G., E. Andò, J. Desrues & G. Viggiani, "Fabric evolution and strain localisation in inherently anisotropic specimens of anisometric particles (lentils) under triaxial compression". *Granular Matter* 25, 15 2023.

185. Coppin, N., M. Henry, M. Cabrera, E. Azéma, F. Dubois, V. Legat & J. Lambrechts, "Collapse dynamics of two-dimensional dry and immersed granular columns of elongated grains". *Phys. Rev. Fluids* 8, 094303 9 Sept. 2023.

186. Orozco, L. F., J.-Y. Delenne, P. Sornay & F. Radjai, "Discrete-element model for dynamic fracture of a single particle". *International Journal of Solids and Structures* 166, 47–56 2019.